

11:26:47

OCA PAD INITIATION - PROJECT HEADER INFORMATION

09/02/88

Active

Project #: E-25-602  
Center #: R6581-OA0

Cost share #: E-25-346  
Center shr #: F6581-OA0

Rev #: 0  
OCA file #:  
Work type : RES  
Document : GRANT  
Contract entity: GTRC

Contract#: DMC-8810146  
Prime #:

Mod #:

Subprojects ? : N  
Main project #:

Project unit: ME  
Project director(s):  
LEE K-M ME

Unit code: 02.010.126

Sponsor/division names: NATL SCIENCE FOUNDATION / GENERAL  
Sponsor/division codes: 107 / 000

Award period: 880901 to 910228 (performance) 910531 (reports)

Sponsor amount	New this change	Total to date
Contract value	60,273.00	60,273.00
Funded	60,273.00	60,273.00
Cost sharing amount		10,500.00

Does subcontracting plan apply ? : N

Title: DEVELOPMENT OF A SPHERICAL STEPPER WRIST MOTOR

PROJECT ADMINISTRATION DATA

OCA contact: Steven K. Watt 894-4820

Sponsor technical contact

Sponsor issuing office

MARVIN F. DEVRIES  
(202)357-7676  
NATIONAL SCIENCE FOUNDATION  
ENG/DMC  
WASHINGTON, D.C. 20550

PATRICK A. WELSH  
(202)357-9602  
NATIONAL SCIENCE FOUNDATION  
DGC/ENG  
WASHINGTON, D.C. 20550

Security class (U,C,S,TS) : U  
Defense priority rating : N/A  
Equipment title vests with: Sponsor  
NONE PROPOSED

ONR resident rep. is ACO (Y/N): N  
NSF supplemental sheet  
GIT X

Administrative comments -  
PROJECT INITIATION. NSF 87-69, RESEARCH INITIATION AWARD - 1988

GEORGIA INSTITUTE OF TECHNOLOGY  
OFFICE OF CONTRACT ADMINISTRATION

NOTICE OF PROJECT CLOSEOUT

Closeout Notice Date 06/26/91

Project No. E-25-602 \_\_\_\_\_ Center No. R6581-0A0 \_\_\_\_\_

Project Director LEE K-M \_\_\_\_\_ School/Lab MECH ENGR \_\_\_\_\_

Sponsor NATL SCIENCE FOUNDATION/GENERAL \_\_\_\_\_

Contract/Grant No. DMC-8810146 \_\_\_\_\_ Contract Entity GTRC

Prime Contract No. \_\_\_\_\_

Title DEVELOPMENT OF A SPHERICAL STEPPER WRIST MOTOR \_\_\_\_\_

Effective Completion Date 910228 (Performance) 910531 (Reports)

Closeout Actions Required:	Y/N	Date Submitted
Final Invoice or Copy of Final Invoice	N	_____
Final Report of Inventions and/or Subcontracts	Y	910605
Government Property Inventory & Related Certificate	N	_____
Classified Material Certificate	N	_____
Release and Assignment	N	_____
Other _____	N	_____

Comments BILL VIA NSF LOC \_\_\_\_\_

Subproject Under Main Project No. \_\_\_\_\_

Continues Project No. \_\_\_\_\_

Distribution Required:

Project Director	Y
Administrative Network Representative	Y
GTRI Accounting/Grants and Contracts	Y
Procurement/Supply Services	Y
Research Property Management	Y
Research Security Services	N
Reports Coordinator (OCA)	Y
GTRC	Y
Project File	Y
Other _____	N
_____	N

NOTE: Final Patent Questionnaire sent to PDPi. GOR

# ON THE DEVELOPMENT OF A SPHERICAL WRIST ACTUATOR

Kok-Meng Lee Jian-Fa Pei

The George W. Woodruff School of Mechanical Engineering  
Georgia Institute of Technology

Uri Gilboa

Armament Development Authority  
Haifa, Israel

**ABSTRACT** The research is to establish the theoretical basis for the design, dynamic modeling and control of a spherical wrist motor which presents some attractive possibilities by combining pitch, roll, and yaw motion in a single joint. The spherical wrist motor has potential applications where the demand on workspace is low but for high-speed precision isotropic manipulation of end-effector orientation, is required continuously in all directions. In this paper, both the finite-element method and the permeance-based model are used for the design and control of the spherical stepper motor. The results of the finite-element method provide the necessary knowledge on the magnetic flux patterns, which are essential for design optimization and dynamic modeling for spherical motor control.

**INTRODUCTION** Recent developments in robotics, data driven manufacturing and high precision assembly have provided the motivation for resurfacing of unusual designs of electromechanical transducers. A flurry of research activity is currently underway in direct drives involving DC, stepping, and brushless electro-mechanical actuators to improve performance by eliminating the problems inherent in the gear systems such as backlash, friction due to meshing, and mechanical compliance. These devices are normally employed to accomplish a single degree-of-freedom (DOF) motion at each joint. In applications such as high speed plasma and laser cutting, it is required that the end effector is oriented quickly, continuously and isotropically in all directions. The popular three-consecutive-rotational-joints wrist possesses singularity inside its workspace [1] [2], which is a major problem in trajectory planning and control. In addition, a significant undesired centrifugal effect is expected in the wrist dynamics.

The research efforts described in this paper have been focused on the creation of a spherical motor which presents some attractive possibilities by combining pitch, roll, and yaw motion in a single joint. In addition to the compact design without the use of speed reducer, the spherical wrist motor results in relatively simple joint kinematics and has no singularities in the middle of the workspace except at the boundaries. A particular form of spherical induction motor was originally designed, built and successfully tested by Laithwaite et al. [3] [4] [5]. The concept of a spherical motor was later employed in the design of a rotodynamic pump [6] and gyroscope applications [7] [8]. An attempt was made to develop the theoretical basis of a field control spherical induction motor in [9], which was suggested as a robotic wrist actuator in [10]. However, realization of a field-control prototype spherical induction motor remains to be demonstrated. The mechanical design of a spherical induction motor is complex. Laminations are required to prevent movement of unwanted eddy currents. Complicated three phase windings must be mounted in recessed grooves in addition to the rolling supports for the rotor in a static configuration. Recently, some efforts have been directed towards the design of multi-DOF wrist based on DC field windings [11] [12]. These DC spherical motors have the advantage of simplicity in control. However, they are, in general, have very limited range of motion. These and other considerations lead to an investigation of an alternative spherical actuators based on the concept of variable reluctance (VR) stepper motor which is easier to manufacture [13]. The trade-off, however, is that sophisticated control scheme is required.

The motor designs to date have been based on arguments employing rather simple magnetic circuit concepts. These are useful only to yield order of magnitude estimates of the forces involved. A good understanding of the magnetic fields and forces at play are necessary to realize an effective and efficient spherical motor design and control. This paper presents the theoretical development of the spherical VR wrist actuator. The analysis is performed using both the finite-element method [14] and a permeance-based model [15]. The permeance-based model, which is commonly used in the stepper motor community to model the reluctance force of a step motor, was developed for design optimization, dynamic modeling, and motion control. Since the success of the permeance-based model depends significantly on the assumed shape of the magnetic flux tubes, the finite element method was used in this study to provide physical insights of the magnetic flux patterns and to examine the validity of the assumed flux shape.

**DESIGN CONCEPT** The spherical motor operates on the variable-reluctance (VR) principle. A conceptual schematic of the electro-mechanical spherical motor is shown in Fig. 1(a). The spherical motor consists of two sub-assemblies: the rotor and the stator. The rotor is supported freely by means of gimbals. The rotor is a smooth sphere in which  $m$  electromagnetic coils or permanent magnets are impeded as illustrated in the assembly view in Fig. 1(b). The rotor coils or permanent magnets are radially oriented and joined at the spherical core, which is magnetic. The remaining rotor structure is non-magnetic but of hard material, the surface of which is a part of the bearing structure. The hollow spherical stator houses  $n$  ( $\neq m$ ) electromagnetic coils with ferromagnetic core. Fig. 1(c) shows an example of orientation measurement using encoders.

**Coil arrangement constraints** The spherical actuator has an infinite number of rotational axes and has three degrees of freedom. At least two torques which are not co-linear with the center of the rotor are necessary to provide rotor stability at a static position and three DOF motion at any instant. Since only one energized rotor poles can be actuated by attraction in any direction along a tangent of the inner surface of the stator and thus provide two DOF motion control. The third DOF motion control, which is the spin motion about an axis through the center of the rotor and the point of attraction, must be provided through a second force of attraction. Thus, the minimum number of rotor coil excitation is two ( $m \geq 2$ ). The maximum number of coils which can be evenly spaced on a sphere can be shown to be 20 corresponding to the number of complex angles of a dodecahedron [16].

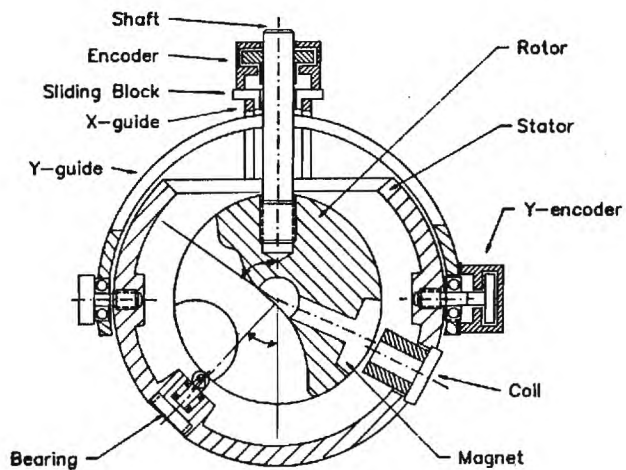


Fig. 1(a) Conceptual Schematics

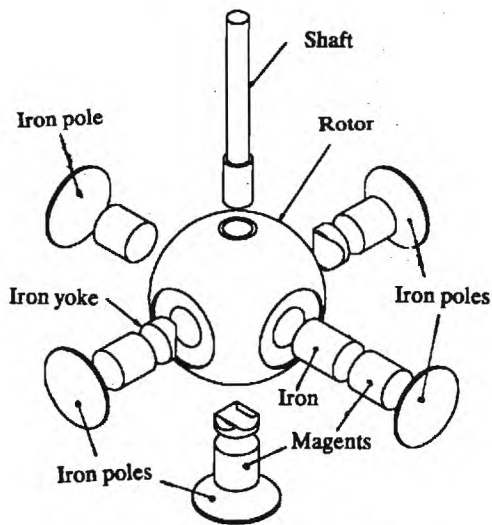


Fig. 1(b) Schematic of Rotor Assembly

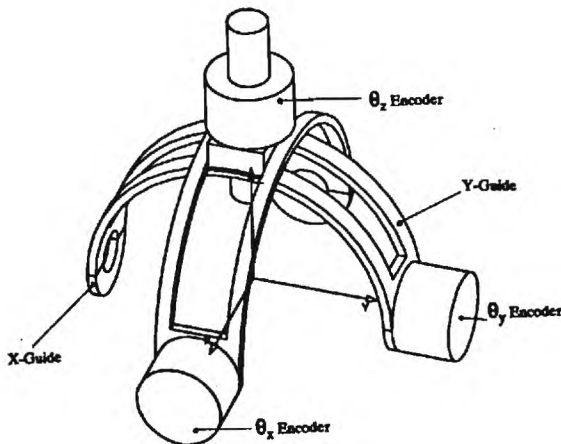


Fig. 1(c) Orientation Measurement

**Driving mechanism** The driver of the mechanism is the magnetic attraction force between the rotor and the stator coil excitations. The stator coils can be energized individually using a control circuitry. As the stator coils adjacent to the rotor poles or permanent magnets are energized, a magnetic field is generated. The corresponding magnetic flux flows through the air gap between the rotor and the stator. The magnetic attraction is created as the system tries to minimize the energy stored and reduces the reluctance of the magnetic path. The tangential components of the magnetic force attract the adjacent rotor poles and hence exert a resultant torque on the rotor. Appropriate control of the current which excites the stator coils and/or rotor coils results in the rotor moving in any direction desired. Unlike the conventional stepping motor where the resolution is discrete, the spherical wrist motor being developed has infinitesimal resolution.

**Preliminary analytical model** To obtain some knowledge on the initial design and control of the spherical motor, an analytical procedure to predict the force generation for motion control using the permeance-based model has been derived with the following assumptions: (1) The iron reluctance is assumed infinite as compared to the air reluctance. (2) No hysteresis or saturation of iron elements in the system. This assumption is reasonable as long as the coil excitations are limited so that the flux density in the iron is within the linear portion of the iron magnetization curve. (3) The assumed flux path is connected to the nearest coil by a straight line and/or a circular arc such that it enters or emerges iron surface perpendicularly and does not cross other flux paths. (4) No magnetic flux leakages between the adjacent stator coils, between the adjacent rotor coils, or in the system. (5) The coil excitations are made such that there are only attraction forces between rotor coils to stator coils. Repulsion between coils generates significant flux leakages. This assumption is also a necessity in order for assumption (4) to be reasonably stated. The flow chart which illustrates the procedure of the static force generation using permeance-based method is shown in Fig. 2.

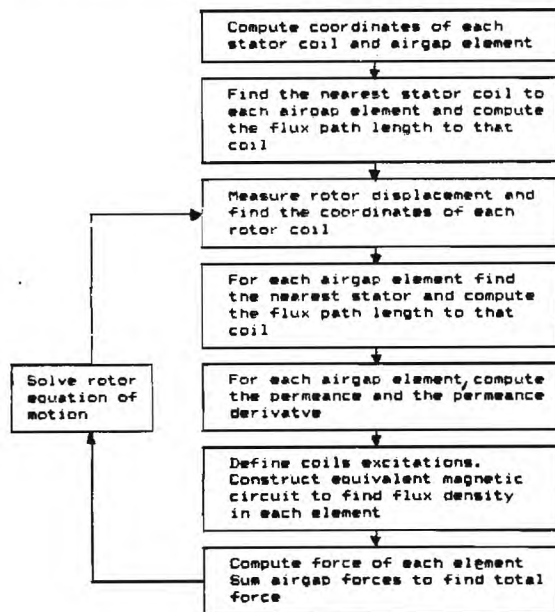


Fig. 2 Flow Chart illustrating Permeance-based Model

The preliminary investigation in developing permeance-based model for motion control [15] has proved the concept feasibility and has yielded qualitative agreement. The success of the permeance-based model, however, depends significantly on the assumed shape of the magnetic flux tubes.

**OBJECTIVE AND PLAN** The objective of the research is to perform the design and to model the spherical motor dynamics for three DOF high-speed precision motion control. The research consists of three specific tasks. The first is the prediction of the fields and commensurate forces for a given design. The second is an optimization using nonlinear programming techniques. The third is the development of the control scheme and its associated sensing. These tasks are described as follows:

(1) The finite element package called ANSYS written by Swanson is used to predict the magnetic fields [17]. This package is used to compute the fields at each of the brick nodes. With the knowledge of the fields at hand, we can approach the calculation of the forces through the Maxwell stress tensor. Once done, the torque can be computed, which will indeed be a rather non-linear functional of all the parameters; namely, air gap, magnet separation, pole pitch, current/slot, size. The result of this task provides the basis for a good field and force prediction and a good understanding of the influences of the design parameters on torque generation, resolution, and control performance.

(2) The requirements for the spherical wrist motor for the robotics application are rather stringent. To be specific, we desire to maximize torque while minimizing weight and volume. The design discussed above allows us to realize three degrees of motion while still employing a rather simple design. This design still allows us several degrees of freedom which must be pinned down, these being gap, magnet separation, pole pitch of the windings, the current per slot, and the size of the motor itself. The second task is an optimization using non-linear programming techniques to suggest an optimal spacing of magnetics, choice of pole pitch, gap, and current per slot appropriate for motor design. To optimize this functional according to an objective criteria, the criteria this research chooses is to maximize torque given certain external size and requirements, both in weight and outer diameter, as well as necessary requirements on air-gap between the rotor and the stator and the current density allowed per slot. The nonlinear optimization will be approached using the techniques suggested by Rosen [18] [19].

(3) Unlike a single-axis motor, the dynamic equations of the three DOF spherical motor are coupled, time-varying and non-linear. In addition, the possible directions of movement for the spherical motor is considerable much more than a single-axis VR step motor, it is not realistic to pre-program all the possible excitation sequence in hardware. It is expected that a microprocessor based switching circuitry is needed to perform a preliminary path planning in addition to position control algorithm. The third task is to develop the dynamic model and the control algorithms for motion control.

**EFFECT OF COIL EXCITATION ON RELUCTANCE FORCE** For motion control, both the direct dynamics which determine the torque generated as a result of activating the motor coils and the inverse dynamics which determine the coil excitations required to obtain the desired torques are needed in the motion control of the spherical motor. The solution to the

direct dynamics is unique but the inverse dynamic may have many solutions and therefore an optimization is required. To obtain some knowledge of coil excitation on flux distributions, magnetic leakages, and reluctance forces, a two-dimensional model of one degree-of-freedom (DOF) linear motion structure was computed, which permits a variety of magnetic field interactions between the stator and the coil excitation to be investigated.

The model where the depth dimension is infinite is shown in Fig. 3. The flux distribution and the static force generated between the stator and the rotor for a given coil excitation is determined using both the finite-element method and a permeance-based model. The finite element technique is based on ANSYS package written by Swanson [17]. To make the two methods comparable, the product of the current density and the coil cross-sectional area is chosen such that it yields the desired magneto-motive-force (mmf). That is,  $J = (\text{mmf})/A$ , where  $J$  is the current density in Amperes/m<sup>2</sup>; mmf is the magneto-motive-force in Ampere-turns; and  $A$  is the cross-sectional area of the coil in m<sup>2</sup>. In the simulation, the cross-section of the coil on each side is 20mm x 3mm. Thus, 100 Ampere-turns are equivalent to 1.66E+6 Amperes/m<sup>2</sup>. Seven cases of coil excitations are shown in Figs. 4 and 5. The left illustrations indicate the excited coils and the excitation direction where the magnitude of each excitation is 100 Ampere-turns. The right illustration shows the magnetic flux path pattern as generated by the computation of the finite element model. The effective permeance of the iron used in the left illustration was about 1E+3. The axial forces are computed by Ansys program and by permeance-based model. The percentage error listed is relative to the force computed by finite element method in TABLE I.

**Prediction using finite-element method** Since the magnetic system tends to minimize the energy stored in the air gap, the change in magnetic flux in the air gaps between coils #1 and #11, coils #2 and #10, or coils #6 and #7 would generate a positive force and that between coils #3 and #9 or coils #4 and #8 would result in negative force. Fig. 4 illustrate some examples of generating positive forces. For the same input excitation, Case (1) yields a much larger force than that generated in Cases (2) and (3). For Case (2), there is an increase in leakage flux in coil #6 due to the removal of coil #7 excitation. Similar leakage flux between coil #10 and the adjacent rotor poles can also be observed. Although the excitation in Case (3) is similar to that in Case (1), the former yields a smaller force due to the smaller misalignment between the excited coils. With the input excitation tripled in Case (4), the force generated can be increased by a factor of four despite the fact that there is more magnetic leakages between adjacent poles than the previous three cases. The significant increase of force is the result of well-shaped magnetic flux path which not only utilizes all the positive force generating air-gaps but also effectively eliminates the flowing of magnetic flux through the negative force generating air-gaps.

Three different alternatives to generate negative forces are shown in Fig. 5. In Case (5), the magnetic leakages cause the flux from the rotor coil #9 to return through one side of the rotor poles. The relocation of the excitation from rotor coil #9 to coil #8 has significantly changed the flux patterns and effectively eliminated the field generated in air-gap between stator coils #6 and rotor coil #7. The force generation can be increased by a factor of five by doubling the input excitation which results in a well-shaped flux path as compared to the case (6).

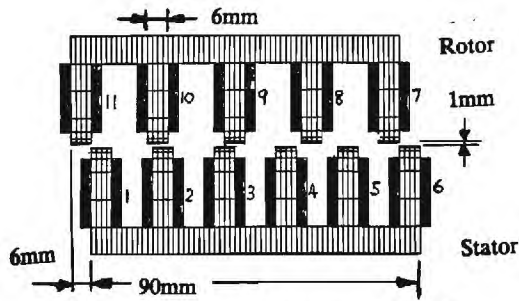
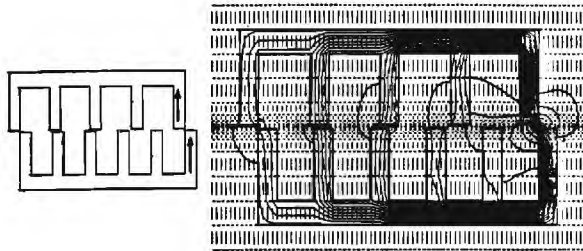
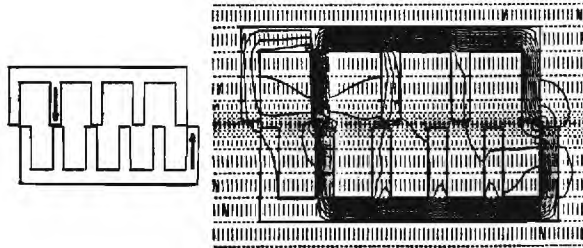


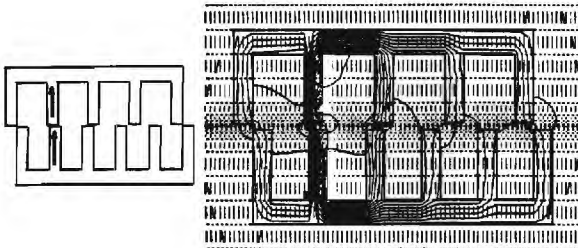
Fig. 3 Two-Dimensional Computation model



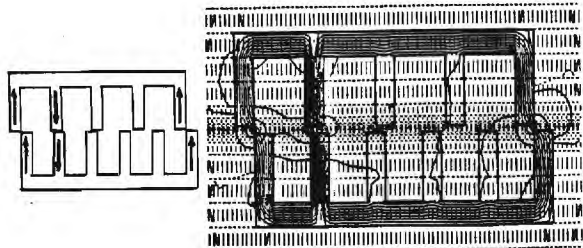
4(a) Case 1



4(b) Case 2

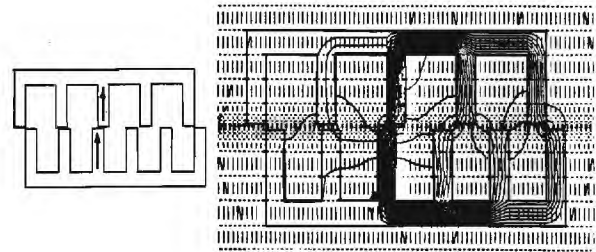


4(c) Case 3

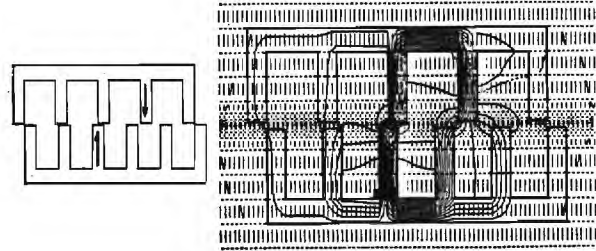


4(d) Case 4

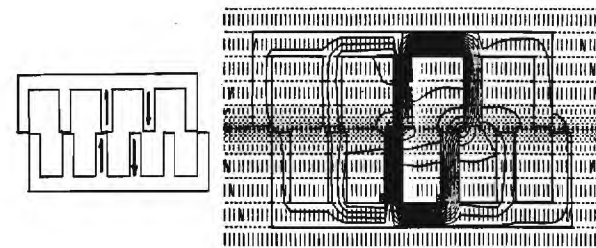
Fig. 4 Flux Distribution of Postive Force Generation



5(a) Case 5



5(b) Case 6



5(c) Case 7

Fig. 5 Flux Distribution of Negative Force Generation

TABLE I: COMPUTED RELUCTANCE FORCE

Case	P-B. Model	F-E. Model (ANSYS)		Relative Error*	
		$\mu_i/\mu_a = 1E+3$	$\mu_i/\mu_a = 1E7$	$E_{(1)}$	$E_{(2)}$
		(N/m)	(N/m)	(%)	(%)
1	16.47	12.17	13.52	35.3	15.5
2	10.81	7.81	8.79	38.4	23.0
3	10.31	7.90	8.82	30.5	16.9
4	63.95	47.68	52.33	34.1	22.2
5	- 8.02	- 4.12	- 4.33	94.7	85.2
6	- 5.89	- 5.39	- 5.89	10.9	1.5
7	-28.88	-26.75	-28.88	0.1	- 7.4

\*  $E_{(1)}$  and  $E_{(2)}$  are the relative error of calculated reluctance forces using permeance-based model with respect to that computed using finite-element model with  $\mu_i/\mu_a = 1E+3$  and  $1E+7$  respectively.

**Prediction using permeance-based model** Except for Case (5), the permeance-based model yields relatively good approximation when the magnetic materials has a very high permeability. There are three major assumptions which may accumulate significant errors in the permeance-based model:

- (1) The model assumes no reluctance in the iron core.
- (2) The model neglects leakage paths.
- (3) The model is inaccurate describing the flux paths.

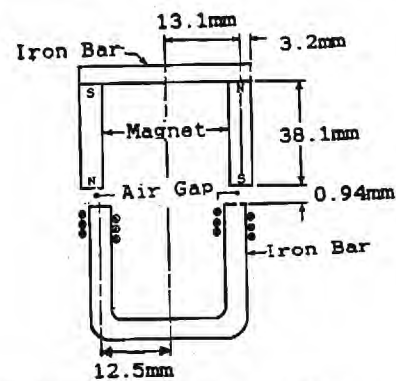
As expected, the model yields higher force than the real system, thus the error is unidirectional. The contribution of the first source may be inferred by running modified finite element model using an iron core of very high permeability. As shown in TABLE I, the relative errors in Case (1) are 35.3% and 15.5% with the iron permeance of  $1E+3$  and  $1E+7$  used in ANSYS program respectively. The decrease in relative error can also be observed in all cases, which is consistent with the assumption made in permeance-based model that the reluctance of the iron is negligible or the permeability of the iron is infinite.

The relative contribution of the second and the third sources to the error is not as obvious. However, it is noted that the relative errors in Cases (2) and (4) are higher than that in Cases (1) and (3) which apparently correspond to the degrees of magnetic leakages. Unlike the cases (1) and (3) where the flux flows from the excited rotor coil and return through both sides of the remaining rotor poles, leakages in Case (5) cause the flux to return through the rotor poles on one side of the excited rotor poles. Thus, the assumption of no magnetic leakages results in relative error of 94.7% and 85.2% in Case (5) computed using iron permeance of  $1E+3$  and  $1E+7$  respectively. On the other hand, the cases (6) and (7) yield much smaller relative error than that of the other cases. In addition, the permeance-based model results in a negative relative error in Case (7) and apparently under-estimates the force generated. Since the flux path is assumed to connect to the nearest coil by a straight line and/or a circular arc in permeance-based model, this assumption may over-estimate the positive force generated in air-gap between the coils #5 and #8.

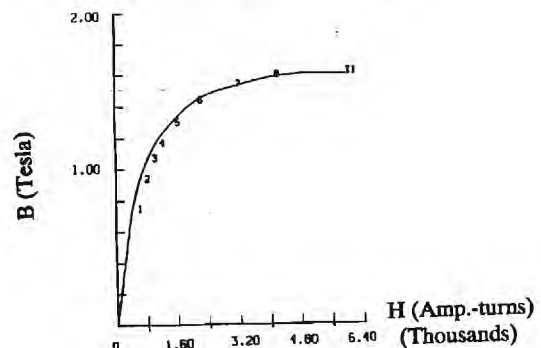
The results have led to the concept of selective magnetic path planning which allows a few coils to be merged physically and still, the individual coils to be function independently. The objective is to restrict the magnetic flux to pass through the selected air-gaps in order to optimize the overall reluctance force in the specified direction for a given set of design parameters. The selective magnetic path planning offers the following potential advantages by distributing the input power among a group of coils, each of which contributes a small fraction of total mmf required: (i) As illustrated in Cases (4) and (7), the force can be significantly increased for a given weight. (ii) Given the same force-to-weight ratio, the multiple coil excitation in selective magnetic path planning allows lower current per coil but large surface areas for heat dissipation. Furthermore, the selective magnetic path planning would tend to result in predictable flux pattern which is a necessity of success for the analytical force prediction using permeance-based model.

**EFFECT OF PERMANENT MAGNETS ON DESIGN** The polarization of the permanent magnet, unlike the d. c. current in the field winding, is flux dependent. The leakage flux distribution has an important effect on the working point of the magnets and so accurate knowledge of the flux distribution is essential for the determination of the performance of motor design having permanent magnets. To determine the effect of the permanent magnets on design, an experimental prediction of the reluctance forces as a function of air-gap separation using a pair of Neodymium-Iron-Boron permanent magnets NDFEB-

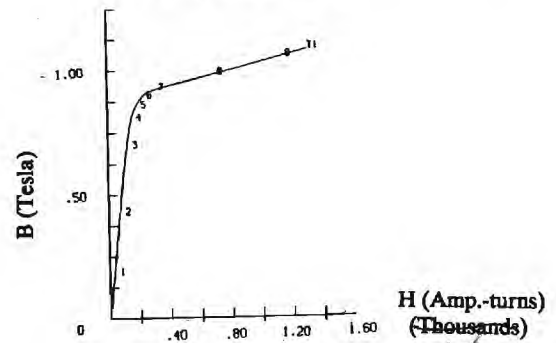
27 was reported in [13] on the system as shown in Fig. 6(a), where the magnetizing characteristics of the iron and magnets are plotted in Figs. 6(b) and 6(c) respectively. The experimental results are displayed as a function of the coil current and spacing in Fig. 7. Each of the coils has a total of 600 turns on an iron bar of 1/4 inch diameter. The dimension of each magnet is 6mm x 6mm x 38mm. The experimental results show that the attraction force has a peak approximately at  $\pm 5.5$ mm. At that particular position, the magnet and the U-bar is about 2/7th overlapped. Further increase of the spacing between stator coils result in rapid decay of restoring force with distance. A maximum force of 3.1 N was obtained even when no coil is excited due to the present of the permanent magnets. The maximum forces of 4.2N, 5.2N, 6.2N and 6.7N were obtained experimentally with a current of 1, 2, 3, and 4 amperes respectively. The forces was not significantly increased as the current was raised higher than 4 amperes showing sign of magnetic saturation.



(a) Experimental System Model [13]



(b) Iron Characteristics



(c) NDFEB-27 Characteristics

Figure 6: Experimental Model and Magnetization Characteristics

A three dimensional finite element model has been computed for the system given in Fig. 6. For simplicity, a U-shaped 6mm x 6mm iron yoke has been used in the computation, which replaced the iron bar of circular cross-section. The model was constructed using 1000 elements and 1386 nodes. The computed results are compared with the tangential component of the experimentally determined static force in TABLE II. Reasonably closed agreements were obtained. Fig. 8 displays the equipotential lines which form an orthogonal system with the magnetic flux for the case with no current excited through the coils. The dashed line indicated the zero potential line. Unlike the d. c. field excitation where the leakage flux occurs primarily between the adjacent excited coils, both self and mutual magnetic leakages can be observed in the permanent magnet. Furthermore, the leakage flux between the adjacent magnets occurs primarily at the free end. The effective magnetic flux flow through the air-gaps depends significantly to the amount of magnetic leakages and the reluctance of magnetic system, both of which tend to decrease the reluctance force obtainable. Fig. 9 shows the equipotential lines of a similar magnetic system with no current excited, in which the width of the permanent magnets is double and the length is reduced by half. For a given volume, the self magnetic leakages increases as the aspect ratio (length-to-width ratio) of the permanent magnets decreases. However, the permeability of the permanent magnets is of the same order of magnitude as that of the air. The decrease of the magnet aspect ratio results in a reduction of overall reluctance of the magnetic system. Thus, the aspect ratio of the permanent magnets for a given volume has a significant influence on the reluctance force obtainable. The reluctance force computed for the configurations in Fig. 8 and 9 are 2.09 N and 5.04 N respectively.

To determine the cause of magnetic saturation, the absolute field strength and the flux density distributions along the permanent magnets and the iron core from the air-gap are plotted in Fig. 10(a) and 10(b) respectively. The computed field strength and the flux density of the iron in the range of 200 - 600 ampere-turns and 0.4 - 1.0 T respectively, which is well within the linear range. On the other hand, the permanent magnets have been operated in the near saturation even with no excitation current through the coils. The magnetic saturation of the permanent magnets, however, can be effectively reduced by reducing the aspect ratio for the same volume.

**CONCLUDING REMARKS AND FUTURE WORK** Finite element computation for two particular models has been performed. It was shown that the selection of coil excitations on magnetic field distribution, magnetic leakages have significant influences on maximum reluctance force obtainable. The results indicated that the aspect ratio of the Nd-Fe based permanent magnets has significant influences on the self magnetic leakages, magnetic saturation, and the overall system reluctance. It has also shown that the finite element simulation could be a useful tool not only for design but also to establish a rational basis for dynamic model using permeance-based model. The saturation effects due to the use of permanent magnets have been examined using finite element simulation. Future work will be directed towards the design optimization and the control algorithm development.

**ACKNOWLEDGEMENT** The authors wish to thank the National Science Foundation for its grant DMC-8810146 under which this research was possible.

## REFERENCES

1. Asada, H. and Cro-Granlto, J. A. "Kinematic and Static Characterization of Wrist Joints and their Optimal Design," Proc. of the 1985 IEEE Int. Conf. on Robotics and Automation. 1985.
2. Paul, R. P. and Stevenson, C. N., "Kinematics of Robots Wrist," Int. Journal of Robotics Research, Vol. 2, No. 1, pp. 31-38, 1983.
3. William, F., Laithwaite, E., and Piggot, L., "Brushless Variable-Speed Induction Motors," Proc. IEEE, No. 2097U, pp.102-118, June 1956.
4. Williams, F., Laithwaite, E., and Eastham, G. F. "Development of Design of Spherical Induction Motors," Proc. IEEE, No. 3036U, pp. 471-484, December 1959.
5. Laithwaite, E., "Design of Spherical Motors," Electrical Times, vol. 9, pp. 921-925, June 1960.
6. Laing I. and Laing, N. Patent U.S. 4352646, Rotodynamic Pump with Spherical Motor, October 5, 1982.
7. Lebedev A. and Shinyev, P. "Moments Acting in a Spherical Rotor in a Magnetic Suspension," Priborostrategie, vol. 16, No.5 pp. 85-88, 1973.
8. Izv Vyssh Uchebn Zaved, "Electromagnetic processes in an Asynchronous Motor with a Spherical Hollow Rotor," Electromekh, N. 11, pp 1231-1239, Nov. 1976.
9. Devay, K. and Vachtsevanos, G. "The analysis of Fields and Torques in a Spherical Induction motor," IEEE Trans. Mag., March 1987.
10. Vachtsevanos, G.J., and Davey K., and Lee, K. "Development of a Novel Intelligent Robotic Manipulator," Presented at the 1986 IEEE Int. Conf. on Systems, Man, and Cybernatic, Atlanta, GA October 10-17, 1986. Also in Control Systems Magazine, June 1987.
11. Hollis, R. L., Allan, A.P. and Salcudan, S., "A Six Degree-of-Freedom Magnetically Levitated Variable Compliance Fine Motion Wrist," The 4th Int'l Symp. on Robotics Research, Santa Cruz, August 1987.
12. Kaneko, K., Yamamda, I. and Itao, K. "A Spherical DC Motor with Three DOF," ASME Trans. J. Dyn. Sys., Meas., and Control. Vol. 111, Number 3, September 1989, pp. 398-402.
13. Lee, K-M., Vachtsevanos, G. and Kwan C-K., "Development of a Spherical Stepper Wrist Motor" Proc. of the IEEE 1988 Int. Conf. of Robotics and Automation, Philadelphia, PA, April 24-29, 1988. Also in Journal of Intelligent and Robotic Systems 1 (1988) 225-242.
14. Sylvester, P. and Ferrari, R. L., "Finite Elements for Electrical Engineers," Cambridge University Press, New York, 1986.
15. Chai, H. D. "Permeance Model and Reluctance Force Between Toothed Structures. Theory and Applications of Step Motor edited by Kuo B.C.; West Publishing Co. 1973.
16. Smith, D. E., "Essentials of Plane and Solid Geometry," Wentworth-Smith Mathematical Series, 1923
17. "Introduction to ANSYS," Vol. 1 & 2, Swanson Analysis System.
18. Rosen, J. B. and Kreuser, J., "A gradient projection algorithm for nonlinear constraints," and numerical methods for nonlinear optimization edited by F. A. Lootsman, 1972.
19. Rosen, J. B., "The gradient projection method for nonlinear programming, Part 1 & 2," SIAM Journal of Applied Mathematics, 9, pp. 514-553, 196.

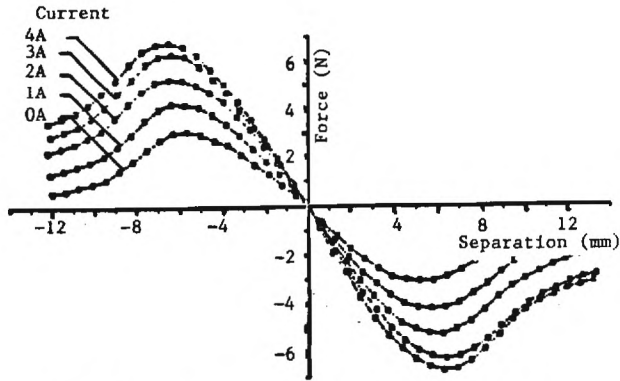


Fig. 7 Experimentally Determined Reluctance Force

TABLE II COMPARISON BETWEEN EXPERIMENTAL AND COMPUTED RELECTUANCE FORCE

Current (Amperes)	Displacement (mm)	Reluctance Force Components (N)		
		F <sub>x</sub>		F <sub>y</sub>
		Computed	Experimental	Computed
0	3	2.09	2.5	11.74
	6	2.81	3.0	5.47
	12	1.15	0.8	0.366
2	6	4.9	5.0	8.47
4	6	5.85	6.0	10.47

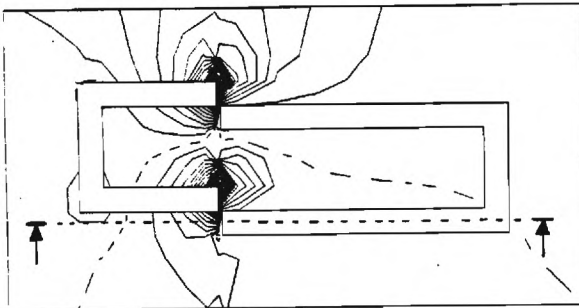


Fig. 8 Equipotential Lines (Aspect ratio = 6.33)

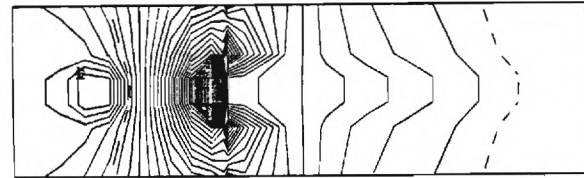


Fig. 9 Equipotential Lines (Aspect ratio = 3.16)

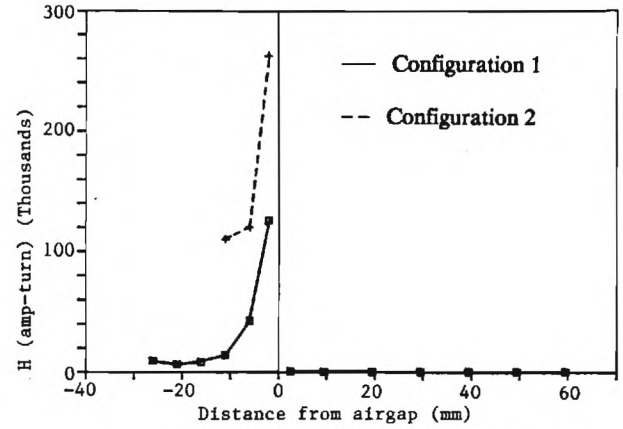
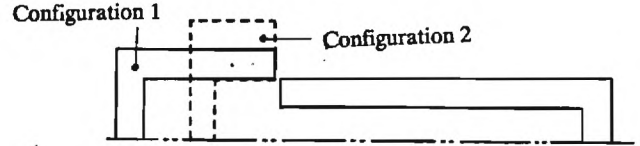


Fig. 10(a) Field Intensity Distribution

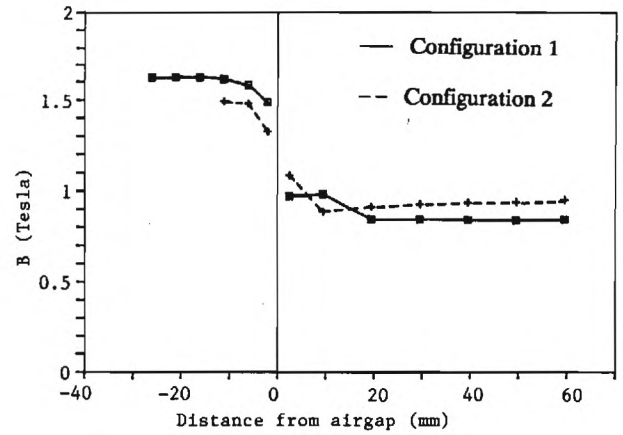


Fig. 10(b) Flux Density Distribution

NATIONAL SCIENCE FOUNDATION  
1800 G STREET, NW  
WASHINGTON, DC 20550

BULK RATE  
POSTAGE & FEES PAID  
National Science Foundation  
Permit No. G-69

## PI/PD Name and Address

Kok-Meng Lee  
Mechanical Engineering  
~~Georgia Tech Research Corp~~  
Atlanta GA 30332

# NATIONAL SCIENCE FOUNDATION FINAL PROJECT REPORT

## PART I - PROJECT IDENTIFICATION INFORMATION

1. Program Official/Org. **Louis A. Martin-Vega** - DDH

2. Program Name **OPERATIONS RESEARCH & PRODUCTION SYSTEMS**

3. Award Dates (MM/YY) From: **09/88** To: **02/91**

4. Institution and Address

**Georgia Tech Research Inst**  
**Atlanta GA 30332**

5. Award Number **8810146**

6. Project Title

**Research Initiation: Development of a Spherical Stepper  
Wrist Motor**

This Packet Contains  
NSF Form 98A  
And 1 Return Envelope

NSF Grant Conditions (Article 17, GC-1, and Article 9, FDP-II) require submission of a Final Project Report (NSF Form 98A) to the NSF program officer no later than 90 days after the expiration of the award. Final Project Reports for expired awards must be received before new awards can be made (NSF Grants Policy Manual Section 677).

Below, or on a separate page, provide a summary of the completed projects and technical information and attach it to this form. Be sure to include your name and award number on each separate page. See below for more instructions.

## PART II - SUMMARY OF COMPLETED PROJECT (for public use)

The summary (about 200 words) must be self-contained and intelligible to a scientifically literate reader. Without restating the project title, it should begin with a topic sentence starting the project's major thesis. The summary should include, if pertinent to the project being described, the following items:

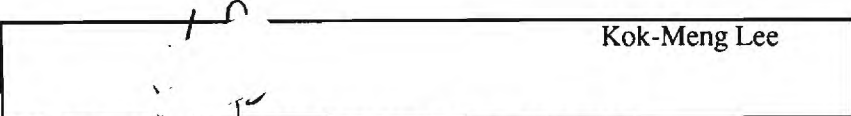
- The primary objectives and scope of the project
- The techniques or approaches used only to the degree necessary for comprehension
- The findings and implications stated as concisely and informatively as possible

This is the final report on the NSF Research Initiation Award DDM-88-10146, "Development of a Spherical Stepper Wrist Motor." During the final reporting period the grant's activities have focused on the theoretical basis for the design, modeling, and control of a three degrees-of-freedom (DOF) spherical variable reluctance (VR) motor, which presents some attractive possibilities by combining pitch, roll, and yaw motion in a single joint. The report covers (1) the determination of kinematically feasible design configurations for a ball-joint-like three DOF spherical VR motor, (2) engineering methods of modeling the reluctance force of the spherical motor using both the finite-element method and a permeance-based model, and (3) analytical forward and inverse dynamic models of the spherical wrist motor.

## PART III - TECHNICAL INFORMATION (for program management use)

List references to publications resulting from this award and briefly describe primary data, samples, physical collections, inventions, software, etc. created or gathered in the course of the research and, if appropriate, how they are being made available to the research community.

See attached information.

 Kok-Meng Lee	May 30 1990
Principal Investigator/Project Director Signature	Date

**IMPORTANT:  
MAILING INSTRUCTIONS**  
Return this *entire* packet plus all attachments in the envelope attached to the back of this form. Please copy the information from Part I, Block I to the *Attention line* on the envelope.

NSF Research Initiation: "Development of a Spherical Stepper Wrist Motor"  
Part III - Technical Information (for program management use)

K-M. Lee, J. Pei, and G. Uri, "On the Development of a Spherical Wrist Actuator," Proceedings of NSF Design and Manufacturing Systems Conference, Tempe, Arizona, January 8-12, 1990.

K-M. Lee and J. Pei, "Kinematic Analysis of a Three Degree-of-freedom Spherical Wrist Actuator," Proceedings of the 5th International Conference on Advanced Robotics, Pisa, Italy, June 20-22, 1991. Also submitted to IEEE Trans. on Robotics and Automation.

K-M. Lee, "An Analytical Development of a Spherical Wrist Actuator," Proceedings of the International Conference on Automation, Robotics, and Computer Vision (Supplement), Singapore, 19-21, September, 1991.

J. Pei, "Methodology of Design and Analysis of Variable-Reluctance Spherical Motors," Ph.D. Thesis (Mechanical Engineering) Georgia Institute of Technology, November, 1990.

K-M. Lee et al., "Development of a Spherical Stepper Wrist Motor," NSF Final Report, (Grant #8810146).

**PART IV — FINAL PROJECT REPORT — SUMMARY DATA ON PROJECT PERSONNEL**

(To be submitted to cognizant Program Officer upon completion of project)

The data requested below are important for the development of a statistical profile on the personnel supported by Federal grants. The information on this part is solicited in response to Public Law 99-383 and 42 USC 1885C. All information provided will be treated as confidential and will be safeguarded in accordance with the provisions of the Privacy Act of 1974. You should submit a single copy of this part with each final project report. However, submission of the requested information is not mandatory and is not a precondition of future award(s). Check the "Decline to Provide Information" box below if you do not wish to provide the information.

Please enter the numbers of individuals supported under this grant.  
Do not enter information for individuals working less than 40 hours in any calendar year.

	Senior Staff		Post-Doctorals		Graduate Students		Under-Graduates		Other Participants <sup>1</sup>	
	Male	Fem.	Male	Fem.	Male	Fem.	Male	Fem.	Male	Fem.
<b>A. Total, U.S. Citizens</b>										
<b>B. Total, Permanent Residents</b>	1									
U.S. Citizens or Permanent Residents <sup>2</sup> :										
American Indian or Alaskan Native . . .										
Asian . . . . .										
Black, Not of Hispanic Origin . . . . .										
Hispanic . . . . .										
Pacific Islander . . . . .										
White, Not of Hispanic Origin . . . . .										
<b>C. Total, Other Non-U.S. Citizens</b>					2					
Specify Country										
1. China					2					
2. Israel									1	
3.										
<b>D. Total, All participants (A + B + C)</b>	1				2				1	
<b>Disabled<sup>3</sup></b>										

Decline to Provide Information: Check box if you do not wish to provide this information (you are still required to return this page along with Parts I-III).

<sup>1</sup>Category includes, for example, college and precollege teachers, conference and workshop participants.

<sup>2</sup>Use the category that best describes the ethnic/racial status for all U.S. Citizens and Non-citizens with Permanent Residency. (If more than one category applies, use the one category that most closely reflects the person's recognition in the community.)

<sup>3</sup>A person having a physical or mental impairment that substantially limits one or more major life activities; who has a record of such impairment; or who is regarded as having such impairment. (Disabled individuals also should be counted under the appropriate ethnic/racial group unless they are classified as "Other Non-U.S. Citizens.")

**AMERICAN INDIAN OR ALASKAN NATIVE:** A person having origins in any of the original peoples of North America, and who maintain cultural identification through tribal affiliation or community recognition.

**ASIAN:** A person having origins in any of the original peoples of East Asia, Southeast Asia and the Indian subcontinent. This area includes, for example, China, India, Indonesia, Japan, Korea and Vietnam.

**BLACK, NOT OF HISPANIC ORIGIN:** A person having origins in any of the black racial groups of Africa.

**HISPANIC:** A person of Mexican, Puerto Rican, Cuban, Central or South American or other Spanish culture or origin, regardless of race.

**PACIFIC ISLANDER:** A person having origins in any of the original peoples of Hawaii; the U.S. Pacific Territories of Guam, American Samoa, or the Northern Marianas; the U.S. Trust Territory of Palau; the islands of Micronesia or Melanesia; or the Philippines.

**WHITE, NOT OF HISPANIC ORIGIN:** A person having origins in any of the original peoples of Europe, North Africa, or the Middle East.

THIS PART WILL BE PHYSICALLY SEPARATED FROM THE FINAL PROJECT REPORT AND USED AS A COMPUTER SOURCE DOCUMENT. DO NOT DUPLICATE IT ON THE REVERSE OF ANY OTHER PART OF THE FINAL REPORT.

FINAL REPORT

Research Initiation:  
**DEVELOPMENT OF A SPHERICAL STEPPER WRIST MOTOR**

by

Kok-Meng Lee, Principal Investigator  
Jianfa Pei  
Xiao-an Wang  
Gilboa Uri

Georgia Institute of Technology  
The George W. Woodruff School of Mechanical Engineering  
Atlanta, Georgia 30332-0405

Prepared for:  
The National Science Foundation  
Washington, D.C. 20550  
Grant DDM-88-10146

## TABLE OF CONTENTS

Abstract .....	2
ACKNOWLEDGEMENT .....	3
1. INTRODUCTION .....	4
1.1 Background .....	4
1.2 Design Concept .....	7
1.3 Reluctance Model .....	9
1.4 Analytical Model .....	10
2. DESIGN CONCEPT .....	12
2.1 Operational Principle .....	12
2.1.1 Torque generation .....	16
2.1.2 Overlapping area of two poles .....	18
2.2 Design Configuration .....	23
2.3 Illustrative Example .....	28
2.3.1 Design configuration .....	28
2.3.2 Motion simulation .....	32
3. RELUCTANCE MODEL .....	38
3.1 Fundamental Equations .....	40
3.2 Comparison between Permeance-based and Finite-element Models .....	44
3.3 Finite-element Analysis .....	52
3.3.1 Finite-element models .....	53
3.3.2 Results and discussions .....	60
3.4 Reluctance Model .....	62
4. ANALYTICAL MODEL OF TORQUE PREDICTION .....	70
4.1 General Formulation .....	70
4.2 Forward Torque Prediction Model .....	75
4.3 Inverse Torque Prediction Model .....	80
4.3.1 Matrix representation .....	80
4.3.2 Formulation for inverse torque model .....	82
4.3.3 Implementation of the inverse torque model .....	84
5. CONCLUSIONS AND FUTURE WORKS.....	92
REFERENCES .....	94
APPENDIX.....	96

## Abstract

This is the final report on the NSF Research Initiation Award DDM-88-10146, "Development of a Spherical Stepper Wrist Motor." During the final reporting period the grant's activities have focused on the theoretical basis for the design, modeling, and control of a three degrees-of freedom (DOF) spherical variable reluctance (VR) motor, which presents some attractive possibilities by combining pitch, roll, and yaw motion in a single joint. The report covers (1) the determination of kinematically feasible design configurations for a ball-joint-like three DOF spherical VR motor, (2) engineering methods of modeling the reluctance force of the spherical motor using both the finite-element method and a permeance-based model, and (3) analytical forward and inverse dynamic models of the spherical wrist motor.

## ACKNOWLEDGEMENT

The authors wish to thank the National Science Foundation for its grant DDM-8810146 under which this research was possible. It represents the opinions of its author only, and is offered for stimulation and exchange of ideas, and does not represent the findings or policies of the National Science Foundation.

## 1. INTRODUCTION

The report summarizes the results of a two year project entitled "Development of a Spherical Stepper Wrist Motor." The goal of this project is to establish the theoretical basis for the design, modeling, and control of the spherical stepper motor. As a result of prior research and extension work, the following issues were identified and addressed:

1. Theoretical basis of kinematically feasible design configurations for a ball-joint-like three DOF spherical VR motor.
2. Engineering analysis methods for modeling the reluctance force of the spherical motor.
3. Analytical modeling method of the spherical wrist motor, which are essential for design optimization and motion control law development of the spherical motor.

The remainder of this section will begin with the overview of prior works and summarizes the progress of the analytical modeling efforts.

### 1.1 Background

The advancements of robotics and automation have motivated the development of a variety of actuators for high performance multi degrees-of-freedom (DOF) wrist motion control. Wrist joints are normally the last few joints of an robotic arm and are used primarily for orienting the end-effector in an arbitrary direction. Significant research efforts have been reported in the design of robotic wrist. Among these, Bennett has developed a six degrees-of-freedom mechanical wrist based on the concept of Stewart platform mechanism [1]. A review of robot wrist designs has been reported in [2].

In some applications, such as high speed plasma and laser cutting, it is required that the end effector is oriented quickly, continuously and isotropically in all directions. Unfortunately, the popular three-consecutive-rotational-joints wrist possesses singularity inside its workspace,

which is a major problem in trajectory planning and control. At a singularity, the wrist cannot orient the end-effector in certain directions. Asada and Cro-Granlto [3] suggested relocation of the singularity outside the required workspace by varying the direction of the end-effector mount. Alternatively, the task may be re-arranged such that the working space of of the end-effector is not in the vicinity of the singularity. However, in the vicinity of a singularity, the ratio of the rotation rate of the wrist joint to that of the end-effector is very large. Paul and Stevensons [4] defined the cone of degeneracy as the the space in which the wrist-joint to end-effector rotation rate ratio is larger than twice the minimum in the entire workspace. In some cases, the cone of degeneracy can have a vertex angle of 60 degrees.

For precision manipulation of robotic wrist, the traditional approach for end-point sensing in a serially actuated consecutive-rotational-joints wrist when the end-point is not in contact with the environment is to measure the joint angles and compute the cartesian position/orientation from the forward kinematics. This process may introduce errors into the final result even if the analytical model is completely accurate, due to the structural deflection of the wrist joint or due to the fact that the actual dimensions of any particular arm may deviate from the nominal values.

Examination of the existing mechanical joints reveals that the ball-joint-like spherical actuator is an attractive alternative to the three consecutive-rotational joint configuration. The interest in spherical motor as a robot wrist is re-triggered because of its ability in providing the roll, yaw and pitch motion in a single joint, isotropic in kinematics and kinetics, and its relatively simple structure. Also, it has no singularity in the middle of workspace except at the boundary. Direct sensing of the end-point orientation is possible due to its simplicity in structure. The elimination of gears and linkages enables both high positioning precision and fast dynamic response to be achieved by a properly designed spherical motor. These attractive features have

potential applications such as high-speed plasma and laser cutting where the orientation must be achieved rapidly and continuously with isotropic resolution in all directions.

A particular form of spherical induction motor was originally designed, built and successfully tested by William et. al. [5], [6], [7], and [8]. Here, the application was in speed control for one-rotational axis - achieved by controlling the direction of the stator wave excitation at an arbitrary angle to the motor axis. Since the work in [5]-[7], little attention has been given to the spherical motor, with the exception to the design of a rotodynamic pump [8] and in gyroscope applications [9], [10].

An increasing need for high performance robotic applications has motivated several researchers to direct their investigation efforts to new actuator concepts to improve the dexterity of robotic wrists. A spherical induction motor was conceptualized in [11] for robotic applications and detailed analysis was given in [12]. However, it is difficult to realize a prototype of its kind because of its complexity in mechanical and winding design and manufacturing, which requires inlaying all three transversing windings on the inner spherical surface of the stator. Laminations are required to prevent movement of unwanted eddy currents. Complicated three phase windings must be mounted in recessed grooves in addition to the rolling supports for the rotor in a static configuration. These and other considerations lead the PI and his co-workerd [13] to investigate an alternative spherical actuators based on the concept of variable reluctance (VR) stepper motor which is easier to manufacture. The trade-off, however, is that sophisticated control scheme is required.

Hollis et al. [14] has developed a six DOF direct-current (DC) "magic wrist" as part of a coarse-fine robotic manipulation. An alternative DC spherical motor design with three DOF in rotation was demonstrated by Kanedo et al. [15], which can spin continuously and can be

inclined to a degree of  $15^\circ$ . Although the DC spherical motor is characterized by its constructional simplicity, the range of inclination and the torque constant are rather limited. Foggia et al. [16] demonstrated an induction type spherical motor of different structure. The range of motion of the spherical motor is a cone of  $60^\circ$  angle. Since the control strategy has not well developed, no results were given on the ability of the motor to realize an arbitrary motions.

## 1.2 Design Concept

Lee and his co-workers [13] have presented the original design concept of the spherical stepper motor as shown in Fig. 1.1. Compared with its DC counterpart, a spherical VR motor has a relatively large range of motion, possesses isotropic properties in motion, and is relatively simple and compact in design. A permeance-base model, which is commonly used in the stepper motor community to model the reluctance force of a step motor, was developed in [17] to predict the the influence of the stator coil spacings on the reluctance force.

It has been demonstrated in the PI's prior research [17] that the operating principle of the three DOF spherical stepper motor differs significantly from the single axis stepper motor. These differences are as follows: (1) Two torques that are not co-linear with the center of the rotor are necessary to provide rotor stability at a static position and 3 DOF motion at any instant. (2) The maximum number of coils which can be evenly inscribed on a spherical surface is limited. (3) The actuation of the spherical VR motor depends on the pole overlapping, the area of which must be determined on the coupled encoder readings. This realization caused us to devote great efforts to determine the kinematic feasibility of the design configuration.

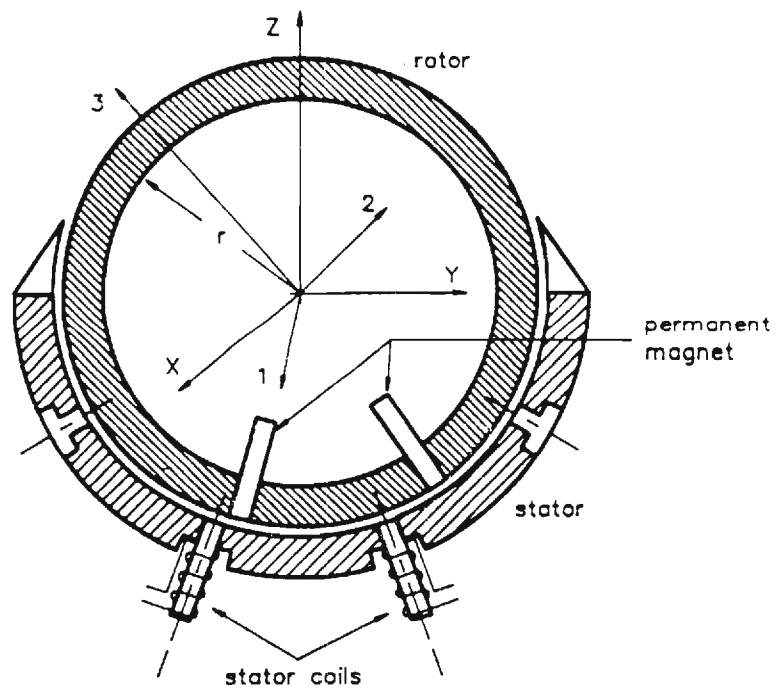


Figure 1.1 Conceptual schematics of a spherical VR motor

Section 2 begins with the operational principle of the spherical motor, which leads to the identification of the optimal design and operational parameters. For the purpose of modeling the kinematics of the spherical motor and hence determining its kinematic feasibility, a general expression to determine the overlapping area between a stator pole and an adjacent rotor pole is presented. The expression of overlapping area allows the constraints imposing the pole design configurations to be described. Along with the results of motion simulation using bang-bang control, a particular design configuration is illustrated.

### 1.3 Reluctance Model

To obtain some knowledge on the initial design of a VR spherical motor, Lee et al. [17] presented the analytical model using a permeance-based model [18] to predict the reluctance force of a spherical stepper motor. However, the permeance-based model which depends significantly on the assumed shape of the magnetic flux tubes yields only qualitative agreement with the experimental study. To provide physical insights of the magnetic flux patterns and to examine the validity of the assumed flux shape of permeance-based model, the finite element analysis [19] [20] was used in this investigation to provide the necessary knowledge on the magnetic flux patterns by numerically solving the Maxwell's equations.

Section 3 presents the modeling technique of the reluctance model using both the finite-element method and a permeance-based model. To obtain some preliminary knowledge of coil excitation on flux distributions, a two-dimensional model of one degree-of-freedom (DOF) linear motion structure where the depth dimension is infinite was analyzed using both the finite-element method and a permeance-based model. The two-dimensional finite element model is formulated using the two-dimensional vector potential method. The results allow a rational

comparison between the finite element method and the permeance-based model, examine the validity of assumptions commonly made in the modeling of permeance, and provide an assessment of the effect of magnetic leakages and fringing on reluctance forces.

A three-dimensional model, which is solved by reduced scalar potential formulation, takes into account of the flux distribution in the third dimension. Thus, it gives a more accurate solution than a two dimensional model. Despite the geometrical modeling difficulty, a three dimensional model is used in order to solve the flux distribution, especially the fringing flux distribution.

#### **1.4 Analytical Model**

For motion control of the spherical motor, both the direct dynamics which determine the torque generated as a result of activating the motor coils and the inverse dynamics which determine the coil excitations required to obtain the desired torques are needed. The solution to the direct dynamics of the spherical motor is unique but the inverse dynamic may have many solutions and therefore an optimization is required. The model permits a variety of magnetic field interactions between the stator and the coil excitation to be investigated. Section 4 presents the analytical modeling of the spherical VR motor. Both the forward and inverse torque predictions are discussed. The objective is to provide an analytical basis for design optimization and control strategy development.

Section 4 begins with the derivation of the torque prediction equations. The reluctance in the iron pole is assumed negligible to obtain a lumped parameter model, and the validity of the assumption has been verified through experiments and finite element analysis. It will be shown in Section 4 that by choosing current sources for coil excitation, the torque prediction are

algebraic and decoupled from the dynamic equations of motion and thus, would reduce the motion control to a great extent.

The inverse problem to torque prediction model is to determine the coil excitations for a specified torque. The inverse problem has infinite solutions and thus a non-linear optimization technique is used to solve the inverse problem. The following aspects are addressed in Section 4; namely, (1) formulation of the inverse problem to torque prediction model for optimization and (2) real-time implementation of the optimization method. The results obtained in this section can be readily used for motion control of the spherical motor.

## 2. DESIGN CONCEPT

The spherical motor referred to in this paper is a ball-joint-like device that consists of two ferromagnetic spheres as shown in Fig. 2.1. These two spheres are concentric and are supported one on the other by bearing rollers in the air gap. The poles on the stator, or the stator poles, are wound by coils and each coil can be energized individually. The ferromagnetic poles are strategically distributed on the stator surface. The rotor poles are distributed on the rotor surface. In order to create a smooth spherical surface for the bearings rollers to roll on, the spherical surface should be made of non-magnetic but hard material except the magnetic poles. In order to maintain geometrical symmetry for simplicity in control, it is desired that the stator poles and the rotor poles are of circular shape.

### 2.1 Operational Principle

The spherical motor is operated on the principle of variable reluctance motor. The driver of the mechanism is the magnetic attraction force between the rotor and the stator coil excitations. The stator coils can be energized individually using a control circuitry. As the stator coils adjacent to the rotor poles are energized, a magnetic field is generated. The corresponding magnetic flux flows through the air gap between the rotor and the stator. The magnetic attraction is created as the system tries to minimize the energy stored and reduces the reluctance of the magnetic path. The tangential components of the magnetic force attract the adjacent rotor poles and hence exert a resultant torque on the rotor. The motor consists of four major components; namely a set of  $M$  interconnecting stator poles, a set of  $N$  interconnecting rotor poles, the air gaps formed between pairs of overlapped stator and rotor poles, and a set of stator coils. A magnetic model of the spherical motor is illustrated by Fig. 2.2(a).

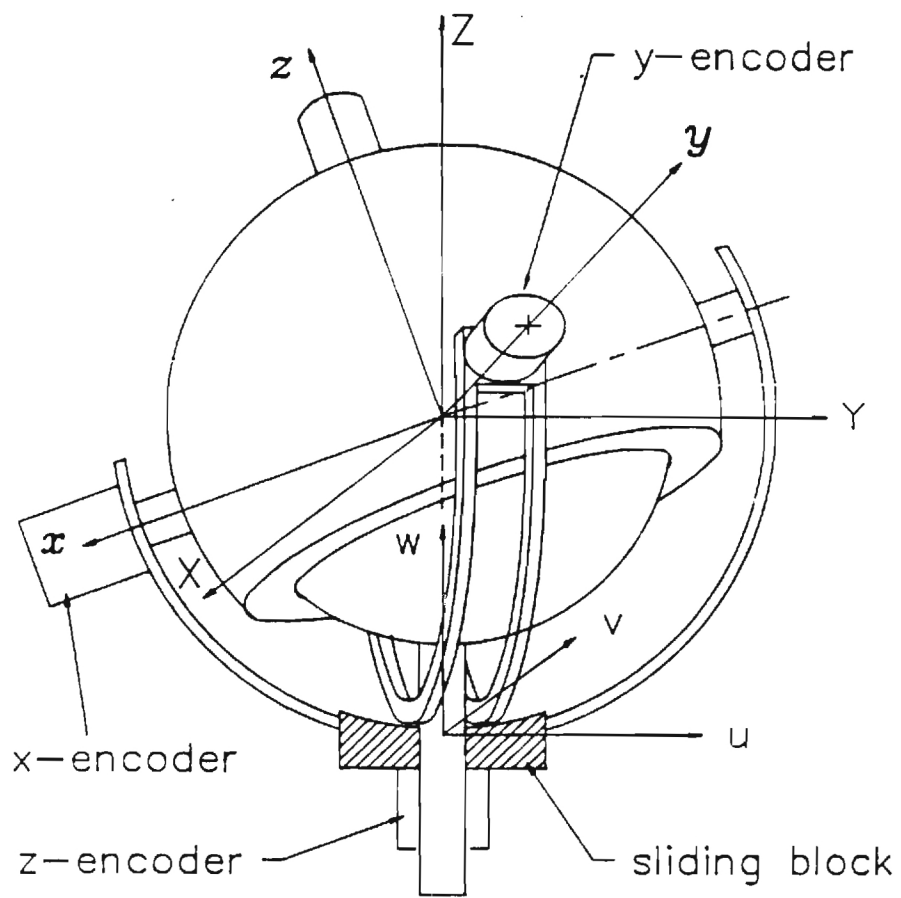


Figure 2.1 (a) Exploded view of spherical VR motor

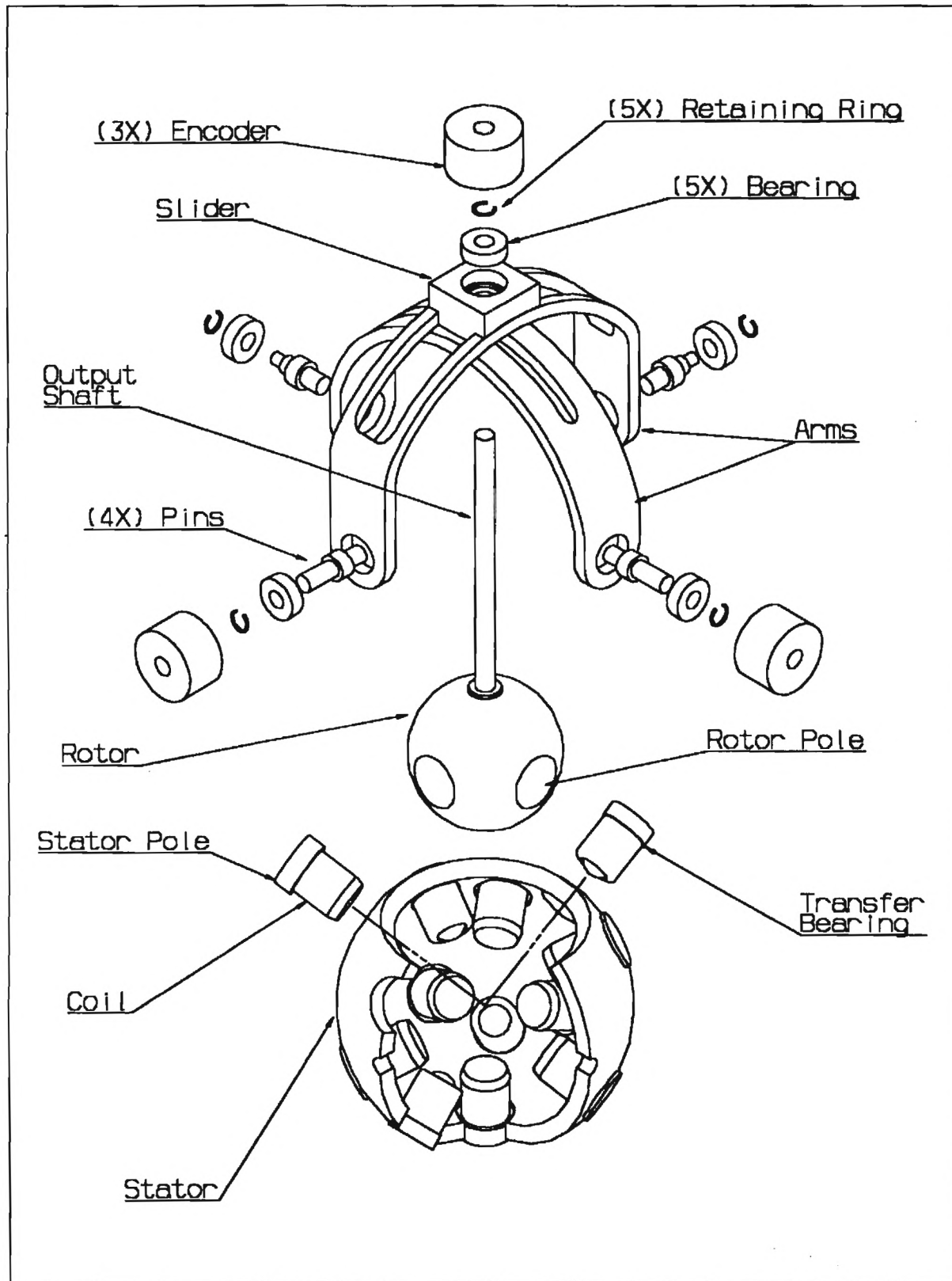
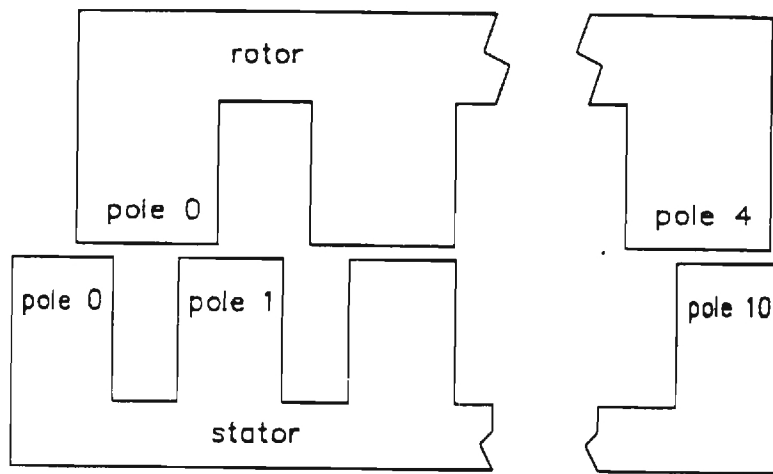
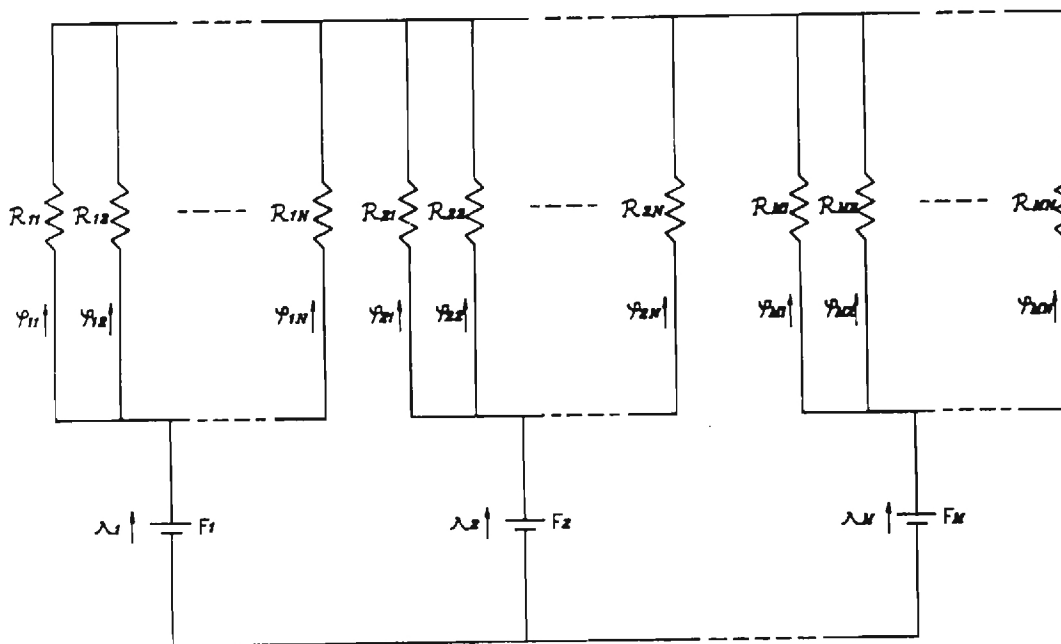


Figure 2.1 (b) Assembly of the spherical VR motor



(a)



(b)

Figure 2.2 Magnetic model and circuit of spherical VR motor

### 2.1.1 Torque Generation

For the purpose of modeling the kinematics of the spherical motor, both the leakage flux and the fringing flux are neglected, and the magnetic system is assumed to be linear. Also, it is assumed that the rotor poles have no coil excitations. The flux between a stator pole and a rotor pole is assumed to flow only through the overlapping area of the two poles. The assumption implies that zero overlapping area corresponds to zero flux. In addition, the flux density distribution in the overlapping area is assumed to be uniform. Thus, the reluctance between the  $k^{\text{th}}$  stator pole and the  $\ell^{\text{th}}$  rotor pole,  $R_{k\ell}$ , is obtained as

$$R_{k\ell} = \frac{g}{\mu_0 S_{k\ell}} \quad (2.1)$$

where  $\mu_0$  is the permeability of air,  $g$  is the air-gap distance, and  $S_{k\ell}$  is the overlapping area between the  $k^{\text{th}}$  stator pole and the  $\ell^{\text{th}}$  rotor pole. If the rotor pole does not overlap with a stator pole, i.e.  $S_{k\ell} = 0$  or  $R_{k\ell} \rightarrow \infty$ , the flux flowing across these two poles is assumed to be zero.

The complete circuit of the spherical motor is presented in Fig. 2.2(b), where  $N$  rotor poles are shown and each rotor pole connects to all  $M$  stator poles. The flux flowing through the air-gap between the  $k^{\text{th}}$  stator pole and the  $\ell^{\text{th}}$  rotor pole is denoted by  $\phi_{k\ell}$  in Fig. 2.2(b).  $\lambda_k$  stands for the flux flowing through the  $k^{\text{th}}$  stator coil. Since the gap reluctances  $R_{k\ell}$ , where  $\ell = 1, 2, \dots, N$ , are in parallel, the total reluctance  $\mathbf{T}_k$  is given by

$$\frac{1}{\mathbf{T}_k} = \sum_{\ell=1}^N \frac{1}{R_{k\ell}} \quad (2.2)$$

where  $\ell = 1, 2, \dots, N$ . The solution of the circuit yields

$$\lambda_k = \begin{pmatrix} 1 \\ \mathbf{T}_k \end{pmatrix} \left[ F_k - \frac{\sum_{\ell=1}^M (F_{\ell} / \mathbf{T}_{\ell})}{\sum_{\ell=1}^M (1 / \mathbf{T}_{\ell})} \right] \quad (2.3)$$

where  $F_k$  is the magneto-motive force (mmf) applied to the  $k^{\text{th}}$  coil,  $k = 1, 2, \dots, M$ .

Since the flux  $\lambda_k$  through a stator coil equals to the sum of the flux of all the air gaps at this coil,  $\phi_{k\ell}$ ,  $\ell = 1, 2, \dots, N$ , the flux in each individual air gap is then solved as,

$$\phi_{k\ell} = \begin{pmatrix} 1 \\ R_{k\ell} \end{pmatrix} \left[ F_k - \frac{\sum_{m=1}^M \sum_{n=1}^N (F_m / R_{mn})}{\sum_{m=1}^M \sum_{n=1}^N (1 / R_{mn})} \right] \quad (2.4)$$

Equation (2.4) represents the flux solution for the spherical motor. The sign of  $F_k$  follows the following convention: if the resulting flux density of the coil points outward, then  $F_k$  is positive. Otherwise  $F_k$  is negative.

From the magnetic circuit solution in Equation (2.4), the magnetic field energy stored in an air gap is

$$E_{k\ell} = \frac{1}{2} \phi_{k\ell}^2 \left( \frac{g}{\mu_0 S_{k\ell}} \right) \quad (2.5)$$

The magnitude of the resulting torque acting on the rotor is derived from the principle of virtual work which yields

$$|t_{k\ell}| = \frac{g}{2\mu_0} \left( \frac{\phi_{k\ell}}{S_{k\ell}} \right)^2 \left| \frac{dS_{k\ell}}{d\theta} \right| \quad (2.6)$$

where  $|dS_{k\ell}/d\theta|$  is the magnitude of the gradient of the overlapping area in spherical coordinates and  $\theta$  is the angle between the position vectors of the stator and rotor poles. The principle of variable-reluctance states that the direction of the torque tends to drive the two poles towards each other in attempt to align the poles. Thus, given the position vectors of the stator and rotor poles as  $\mathbf{q}_k$  and  $\mathbf{p}_\ell$ , the direction of the torque can be determined from Equation (2.7) with respect to a known reference frame

$$\frac{t_{k\ell}}{|t_{k\ell}|} = \frac{\mathbf{p}_\ell \times \mathbf{q}_k}{|\mathbf{p}_\ell \times \mathbf{q}_k|} \quad (2.7)$$

Hence the resulting torque in an air gap is

$$t_{k\ell} = \frac{g}{2\mu_0} \left( \frac{\phi_{k\ell}}{S_{k\ell}} \right)^2 \left[ \frac{dS_{k\ell}}{d\theta} \right] \frac{\mathbf{p}_\ell \times \mathbf{q}_k}{|\mathbf{p}_\ell \times \mathbf{q}_k|} \quad (2.8)$$

where  $k = 1, 2, \dots, M$  and  $\ell = 1, 2, \dots, N$ .

### 2.1.2 Overlapping Area Of Two Poles

The overlapping area between any two adjacent poles determines the resultant tangential force. As indicated by Equation (2.8), the derivation of the overlapping area is necessary.

### Exact solution

Consider any two partially overlapping circular poles on a sphere of radius  $R$ , where the sizes of the poles are denoted by the half-angles as  $\psi_1$  and  $\psi_2$  as shown in Fig. 2.3. Two body coordinate frames,  $X$ - $Y$ - $Z$  and  $x$ - $y$ - $z$ , are attached to the poles  $\psi_1$  and  $\psi_2$  respectively at the origin of the sphere. The orientation of the coordinate frames are assigned such that the  $Z$ -axis and  $z$ -axis are pointing along the normal vectors of the poles respectively and that the  $X$ -axis and  $x$ -axis have a common direction. Thus, the coordinate frame  $x$ - $y$ - $z$  can be described with respect to the  $X$ - $Y$ - $Z$  frame using the following transformation  $[T(\theta)]$

$$[T(\theta)] = \begin{bmatrix} 1 & 0 & 0 \\ 0 & \cos \theta & -\sin \theta \\ 0 & \sin \theta & \cos \theta \end{bmatrix} \quad (2.13)$$

where  $\theta$  is the angle between the  $Z$ -axis and the  $z$ -axis.

In parametric form, the circular edge of the pole denoted by the curve  $e_i$ ,  $i = 1$  and  $2$ , can be written with respect to its own body coordinate frame as

$$\text{curve } e_i: \begin{cases} x^2 + y^2 = (R \sin \psi_i)^2 \\ z = R \cos \psi_i \end{cases} \quad (2.14)$$

In the following derivation, the coordinates are written with respect to the  $X$ - $Y$ - $Z$  frame. Using the transformation matrix given in Equation (2.13) the curve  $e_2$  can be described by

$$\begin{cases} x^2 + (y + R \cos \psi_1 \sin \theta)^2 / \cos^2 \theta = (R \sin \psi_2)^2 \\ x^2 + (z + R \cos \psi_1 \cos \theta)^2 / \sin^2 \theta = (R \sin \psi_2)^2 \end{cases} \quad (2.15)$$

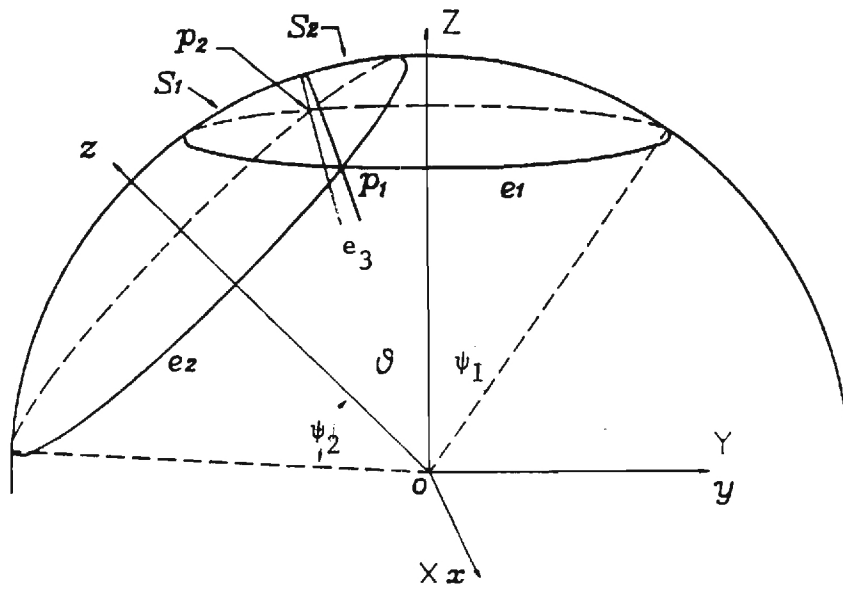


Figure 2.3 Overlapping area of two poles

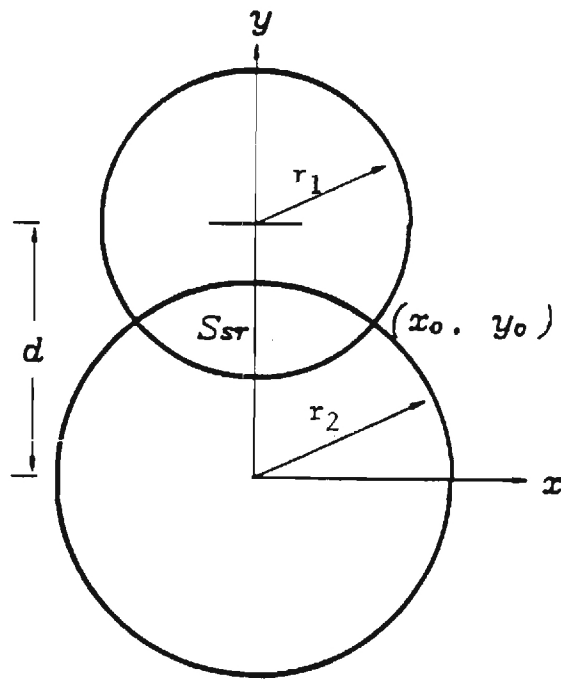


Figure 2.4 approximation of the overlapping area

The position vectors of the two intersecting points are  $\mathbf{P}_1$  and  $\mathbf{P}_2$  which are symmetrical about the YZ plane and can be derived by solving Equations (2.14) and (2.15) simultaneously. Thus, the position vector  $\mathbf{P}_1$  is obtained as

$$\mathbf{P}_1 = \begin{bmatrix} x_{\mathbf{p}_1} \\ y_{\mathbf{p}_1} \\ z_{\mathbf{p}_1} \end{bmatrix} = \begin{bmatrix} \frac{R}{\sin \theta} [(\sin \psi_1 \sin \theta)^2 - (\cos \psi_1 \cos \theta - \cos \psi_2)^2]^{1/2} \\ -\frac{R}{\sin \theta} (\cos \psi_1 \cos \theta - \cos \psi_2) \\ R \cos \psi_1 \end{bmatrix} \quad (2.16)$$

and point  $\mathbf{p}_2$  is a mirror image of point  $\mathbf{p}_1$ . If a plane is defined to pass through  $\mathbf{p}_1$  and  $\mathbf{p}_2$  and the origin of the sphere, the plane would divide the overlapping area  $S$  into two parts,  $S_1$  and  $S_2$ . Let the intersecting contour be denoted by the curve  $e_3$  and the angle between plane  $op_1p_2$  and the XZ plane be  $\rho$ . The intersecting contour  $e_3$  is derived with respect to X-Y-Z frame as

$$\begin{cases} x^2 + y^2 / \sin^2 \rho = R^2 \\ x^2 + z^2 / \cos^2 \rho = R^2 \end{cases} \quad (2.17)$$

where

$$\rho = \tan^{-1} \left( \frac{\cos \psi_2 - \cos \psi_1 \cos \theta}{\cos \psi_1 \sin \theta} \right) \quad (2.18)$$

From the projection of the curves  $e_i$ ,  $i = 1, 2$ , and 3 on the XY plane given in Equations (2.14), (2.15) and (2.17), the overlapping area is computed from the following integral:

$$S_i = \int \int_{D_i} \frac{R}{\sqrt{R^2 - x^2 - y^2}} dx dy \quad i = 1, 2 \quad (2.19)$$

where  $S_i$  and  $D_i$  are the areas bounded by  $e_i$  and  $e_3$  on the spherical surface and the corresponding projections on XY plane respectively. By carrying out the integration, the overlapping area is found to be

$$S = \sum_{i=1}^2 S_i \quad (2.20)$$

where

$$S_i = R^2 \left\{ [1 + \text{Sgn}(\cos \psi_i \cos \theta - \cos \psi_{i+1})] (1 - \cos \psi_i) \pi + 2 \text{Sgn}(\cos \psi_i \cos \theta - \cos \psi_{i+1}) [\Delta_i \cos \psi_i - \sin^{-1}(\cos \Gamma_i \sin \Delta_i)] \right\} \quad (2.21)$$

$$\Gamma_i = \tan^{-1} \left( \frac{\cos \psi_{i+1} - \cos \psi_i \cos \theta}{\cos \psi_i \sin \theta} \right) \quad (2.22)$$

and

$$\Delta_i = \tan^{-1} \left( \frac{\sqrt{(\sin \psi_i \sin \theta)^2 - (\cos \psi_i \cos \theta - \cos \psi_{i+1})^2}}{|\cos \psi_i \cos \theta - \cos \psi_{i+1}|} \right) \quad (2.23)$$

where  $\psi_3 = \psi_1$  and the function  $\text{sgn}(x)$  is 1 if  $x$  is positive or -1 if  $x$  is negative.

### Approximate solution

The expressions of  $S$  in Equations (2.20) and its derivative are rather complicated functions of  $\theta$ ,  $\psi_1$  and  $\psi_2$ , and require time-consuming computation. It is of interest to derive the approximations of the overlapping area and its derivative. The approximated overlapping area has been derived by treating the two poles as planar disks of radii

$$r_i = R \psi_i \quad \text{where} \quad i = 1, 2 \quad (2.24)$$

With the aid of Fig. 2.4, the overlapping area and its spherical gradient are obtained as

$$s = \left[ \frac{\pi}{2} - \text{atan2}(y_o, x_o) \right] r_1^2 + \left[ \frac{\pi}{2} - \text{atan2}(d - y_o, x_o) \right] r_2^2 - x_o d \quad (2.25)$$

and

$$\frac{d}{d\theta} S_{k\ell} = 2 R x_o \quad (2.26)$$

where

$$x_o = \sqrt{r_1^2 - \left[ \frac{r_1^2 - r_2^2 + d^2}{2d} \right]} \quad (2.27)$$

$$y_o = \frac{r_1^2 - r_2^2 + d^2}{2d} \quad (2.28)$$

where  $d$  is the separation between these two disks. The direction of  $dS_{k\ell}/d\theta$  in Equation (2.26) is along the line connecting the centers of the two poles. The comparison between the exact and the approximate solutions is shown in Fig. 2.5 where the overlapping area and its derivative are plotted against the normalized displacement,  $d/(r_1 + r_2)$ . The approximate solution is very close to the exact solution for small  $r_1/r_2$ .

## 2.2 Design Configuration

The geometrical parameters, such as the number of poles and their distribution as well as the size of the poles, directly affect the pole overlappings which in turn affect the motion. The geometrical parameters must be designed based on the following considerations.

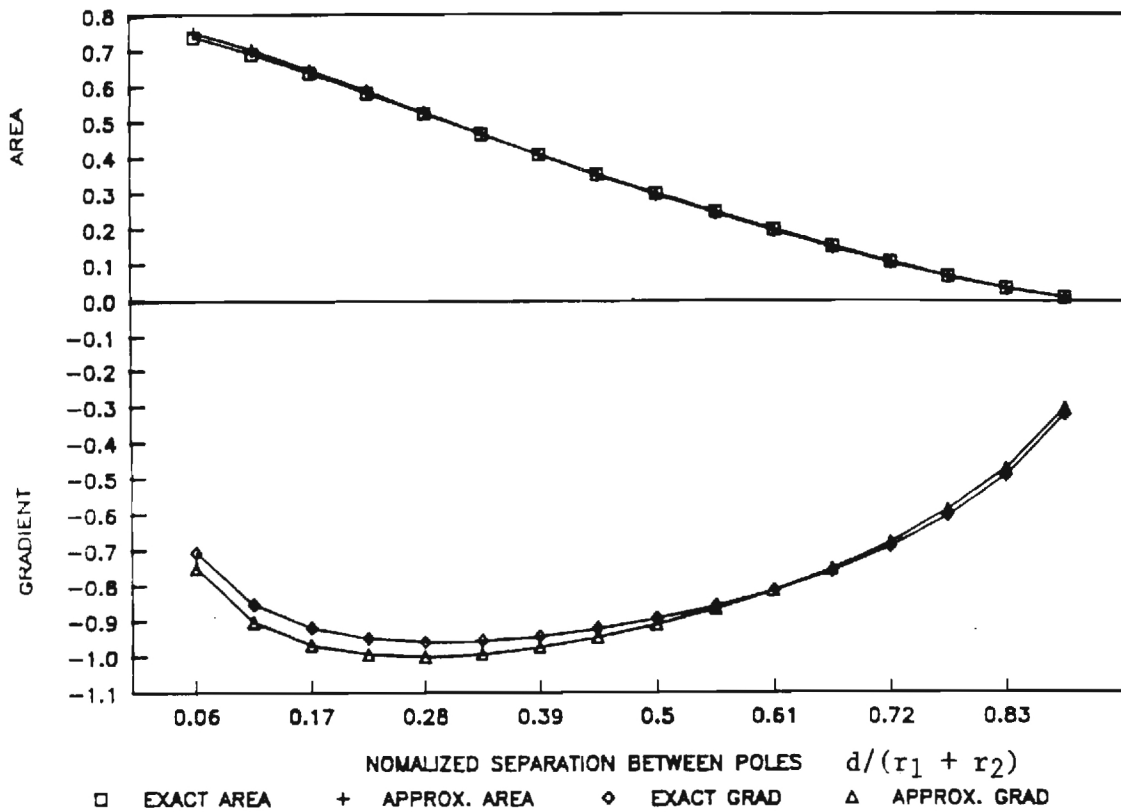


Figure 2.5 Comparison between exact and approximate solutions

For simplicity in motion control, it is desired that the poles are evenly spaced on the stator and on the rotor following the pattern of regular polyhedrons. Each vertex of the polyhedron corresponds to the location of one pole. The regular polyhedrons are tetrahedron, octahedron, cube, icosahedron, and dodecahedron. These polyhedrons have four, six, eight, twelve, and twenty vertices, respectively. The choice on the particular pattern influences the range of inclination which is given by Equation (2.29)

$$\Theta = \pi - \Lambda - \frac{\delta}{2} - \psi_2 \quad (2.29)$$

where  $\Theta$ ,  $\Gamma$ , and  $\delta$  are angles defined in Fig. 2.6.

The spherical actuator has an infinite number of rotational axes and has three degrees of freedom. With only one rotor pole, a point on the rotor surface can be stabilized in any direction along the tangential inner surface of the stator and thus provide two degrees of freedom motion control. To provide the third DOF motion which is the spin motion about an axis through the center of the rotor and that of the rotor pole face, a second force must be actuated at an additional rotor pole. Thus, at least two independent torques which are not colinear acting on the rotor are required to generate three DOF orientations. Furthermore, each of the rotor poles must overlap at least three adjacent stator poles at any instant in order to actuate the rotor pole within the bounded region formed by the adjacent stator poles on the tangential surface of the stator. Thus, it is necessary to have more stator poles than rotor poles, or

$$2 \leq N < M. \quad (2.30)$$

Equation (2.29) must be valid for the entire range of motion.

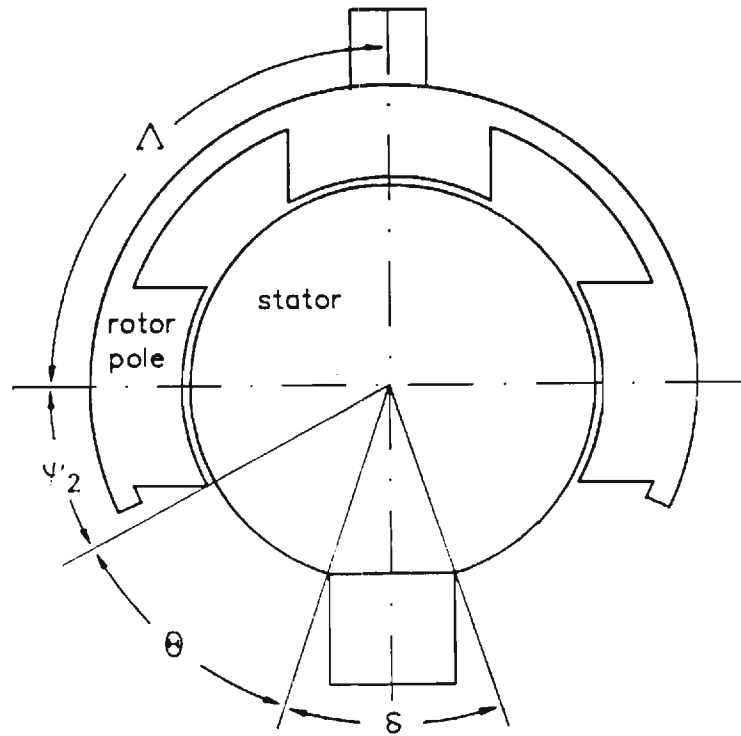


Figure 2.6 Illustration of the range of inclination

It is undesirable that a stator pole simultaneously overlaps more than one rotor poles. The rotor would tend to position itself as the stator pole moves toward the larger overlapping area in an attempt to minimize the reluctance. Thus, in order to avoid the rotor pole to have overlapping area with two or more rotor poles, the following inequality must be satisfied:

$$\psi_1 + \psi_2 < \frac{\Lambda}{2} \quad (2.31)$$

where  $\Lambda$  is the angle between any two adjacent equally spaced rotor poles.

The maximum allowable size of a stator pole is corresponding to the case where two adjacent stator poles are touching each other.

$$\psi_{1\max} = \frac{1}{2} \cos^{-1} (\mathbf{P}_{si} \cdot \mathbf{P}_{sj}) \quad i \neq j \quad (2.32)$$

where  $\mathbf{P}_{si}$  and  $\mathbf{P}_{sj}$  are the position vectors of two adjacent poles.

The rotor orientation at which the spherical motor loses the ability to generate one or more degrees of freedom is referred here as an electro-mechanical singular point. When all the stator and rotor poles are fully overlapping,  $dS_{k\ell}/d\theta = 0$  and no torque would be generated as derived in Equation (2.8). Thus, Equation (2.8) implies that the rotor must not have the same number of evenly spaced poles as that of the stator, i.e.  $N \neq M$ , since a minimum reluctance occurs and no tangential torque can be generated.

### 2.3 Illustrative Example

A particular design configuration, an octahedron/dodecahedron configuration, is given in the following to illustrate the design process. The application of kinematic model for motion

simulation and control of a spherical motor is demonstrated using a kinematic simulation program.

### 2.3.1 Design Configuration

Five rotor poles are located on the inner surface of the outer sphere, corresponding to five vertices of an octahedron. Twenty stator poles are spaced on the outer surface of the sphere in accordance to the pattern of a dodecahedron. The pole locations of the rotor and the stator are illustrated in Figs. 2.7(a) and 2.7(b) respectively. The octahedron/dodecahedron arrangement permits a largest possible number of control inputs evenly spaced on the spherical surface. The locations of the rotor and stator poles in spherical coordinates are tabulated in TABLES 2.1 and 2.2 respectively.

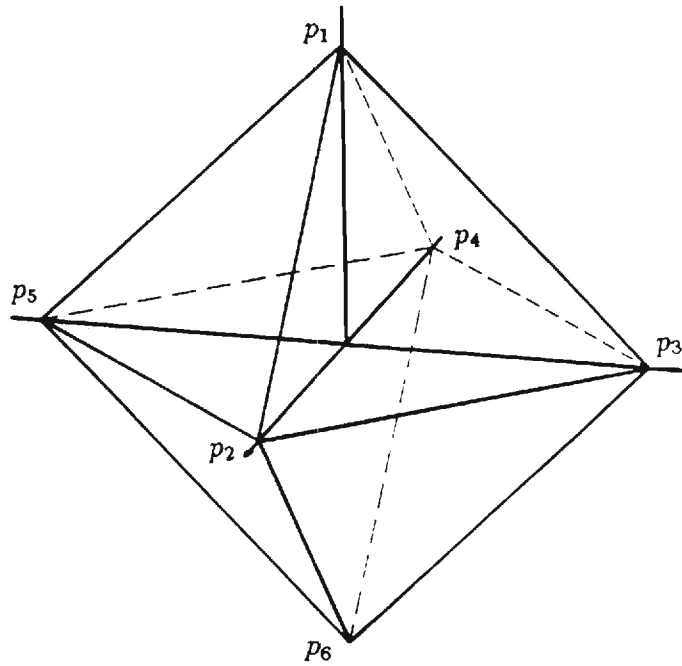
The upper bound on the stator pole size is given by

$$\psi_1 \leq 20.9^\circ \quad (2.33)$$

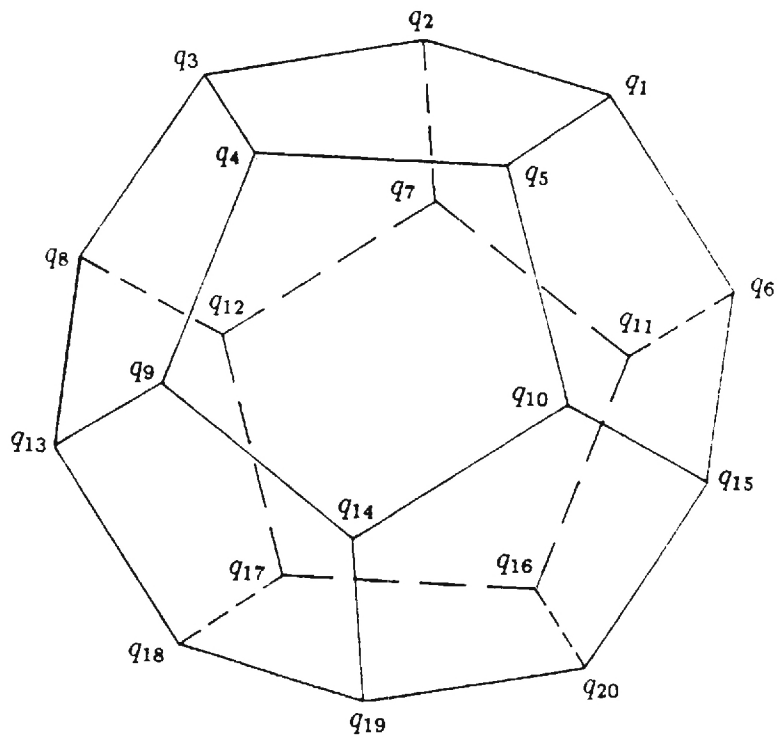
and the inequality which avoids any stator pole to overlap with two or more rotor poles is

$$\psi_1 + \psi_2 < 45^\circ \quad (2.34)$$

The five rotor poles form an orthogonal set of three independent torques that are not colinear with the spherical center. Wherever a pair of stator poles fully overlap with a pair of stator poles on a great circle, the spherical motor may lose the ability to spin about an axis perpendicular to the plane connecting the two fully overlapping rotor poles if the size of the rotor pole is not sufficiently large. Thus, as illustrated in Fig. 2.8, in order to avoid such an electro-mechanical singular point, the size of the rotor pole must satisfy the following inequality given the stator pole.



(a) Octahedron as the model of the rotor



(b) Dodecahedron as the model of the stator

Figure 2.7 Octahedron and dodecahedron configurations

**Table 2.1.** Apex coordinates of an octahedron

pole	$p_1$	$p_2$	$p_3$	$p_4$	$p_5$
x	0	1	0	-1	0
y	0	0	1	0	-1
z	1	0	0	0	0

**Table 2.2.** Apex coordinates of a dodecahedron

coil	$q_1$	$q_2$	$q_3$	$q_4$	$q_5$
x	0.491	-0.188	-0.607	-0.188	0.491
y	0.357	0.577	0	-0.577	-0.357
z	0.795	0.795	0.795	0.795	0.795
coil	$q_6$	$q_7$	$q_8$	$q_9$	$q_{10}$
x	0.795	-0.304	-0.982	-0.304	0.795
y	0.577	0.934	0	-0.934	-0.577
z	0.188	0.188	0.188	0.188	0.188
coil	$q_{11}$	$q_{12}$	$q_{13}$	$q_{14}$	$q_{15}$
x	0.304	-0.795	-0.795	0.304	0.982
y	0.934	0.577	-0.577	-0.934	0
z	-0.188	-0.188	-0.188	-0.188	-0.188
coil	$q_{16}$	$q_{17}$	$q_{18}$	$q_{19}$	$q_{20}$
x	0.188	-0.491	-0.491	0.188	0.607
y	0.577	0.357	-0.357	-0.577	-0.000
z	-0.795	-0.795	-0.795	-0.795	-0.795

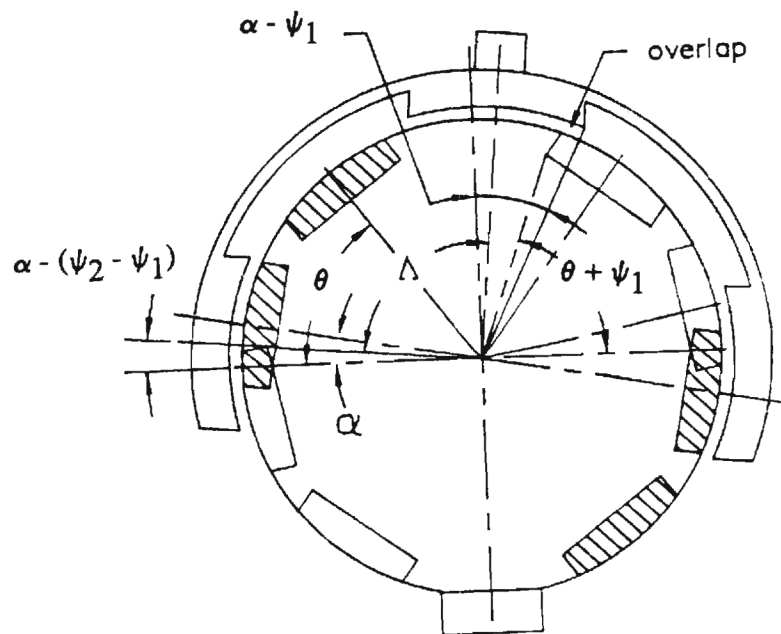


Figure 2.8 Pole size requirements for inclination

$$\cos \theta \cos \phi \sin \gamma + \sin \theta \cos \gamma \geq \cos(\psi_1 + \psi_2) \quad (2.35a)$$

where

$$\gamma = \alpha + \psi_1 - \psi_2$$

For a octahedron/dodecahedron configurations,  $\theta = 52.62^\circ$ ,  $\phi = 36^\circ$ , and  $\alpha = 10.81^\circ$ . In addition,

$$\psi_1 + \psi_2 > \Lambda - \theta \quad (2.35b)$$

The bounded region of the pole sizes computed using Equations (2.33), (2.34) and (2.35) is plotted in Fig. 2.9.

### 2.3.2 Motion Simulation

A computer program was written to simulate the motion of a spherical motor for a pre-specified trajectory. A simple bang-bang control law was used in the simulation which is based on the following steps:

- (1) The direction of the desired torque to generate an incremental step along a pre-specified trajectory from any initial rotor orientation to is determined.
- (2) The direction of the torque at each overlapping area is computed. If the torque contributes motion in the direction of the desired rotation, the corresponding stator coil is selected to be energized. If a stator pole fully overlaps with a rotor pole, the coil is also turned on to provide extra strength to the magnetic field and to provide a return path for the magnetic flux. The magnitude of the mmf is +1 for outward magnetic field or -1 for inward field. Of all the energized coils, about half of them are inward and the other half outward so that closed flux loops could be formed.
- (3) The flux and the torques of all the overlapping areas, which include those with unenergized coils are then computed from the magnetic circuit solution in Equations (4) and (8).
- (4) The resultant torques are obtained by summing vectorly the individual computed torque. The total torque may not be exactly along the desired rotational axis.
- (5) The rotor is rotated a small angle in the direction of the total torque to reach a new orientation.
- (6) Steps (1) - (5) are repeated until the target orientation is reached.

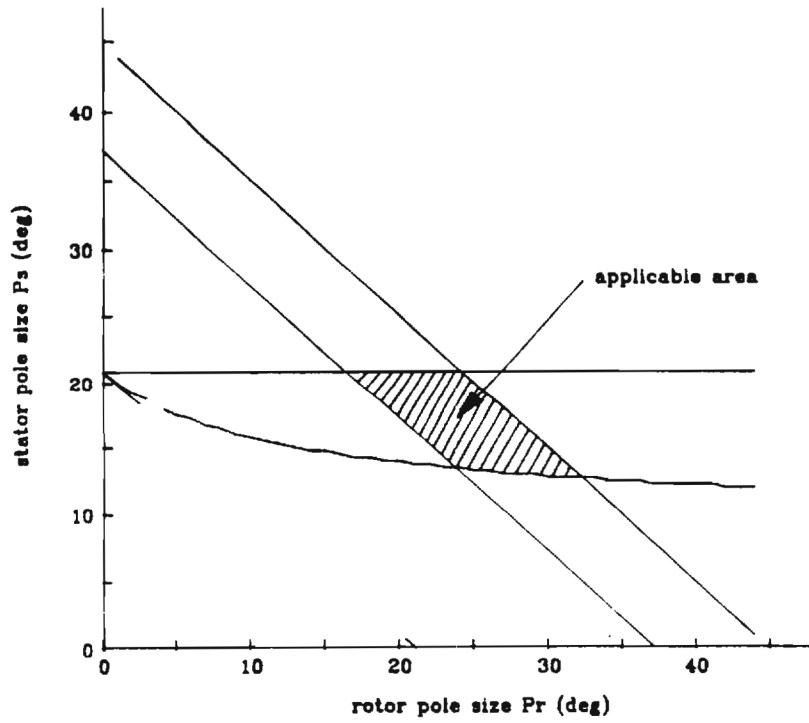


Figure 2.9 Bounds on the rotor and stator pole sizes

For each combination of stator and pole sizes a number of trajectories were tested. TABLE 2.3 gives an example of a typical trajectory in terms of the specified roll, pitch and yaw angles. The three continuous curves represent the actual roll, pitch and yaw angles, whereas the symbols of the curves represent the trajectory specified roll, pitch and yaw angles. The stator and rotor pole sizes for this particular plot are  $15^\circ$  and  $26^\circ$  respectively. This figure shows that the motor is capable of moving from one desired orientation to the other. The corresponding range of inclination is based on the assumption that the stator shaft occupies a cone of  $\pm 20^\circ$ .

As shown in Fig. 2.10, the motor is capable of generating three independent torques at any point within the work space and therefore a desired trajectory of the rotor can be successfully traced. When a more sophisticated control strategy is adopted, the spherical motor is expected to improve its three-dimensional torque capacity and thus to improve its trajectory tracking ability.

In summary, the theoretical design basic for a variable-reluctance motor was established, upon which a specific design scheme that utilizes an octahedron and a dodecahedron as its basic configuration was developed, and its feasibility was verified via a computer simulation.

Table 2.3 Trajectory used in illustrative example

roll	pitch	yaw
0	0	
5	5	0
10	5	0
10	5	10
10	15	10
20	20	10
25	25	20
25	30	25
35	40	30
40	25	30
40	10	25
30	0	25
30	0	10
30	0	-5
20	0	-10
10	0	-20
0	-5	-25
0	-15	-30

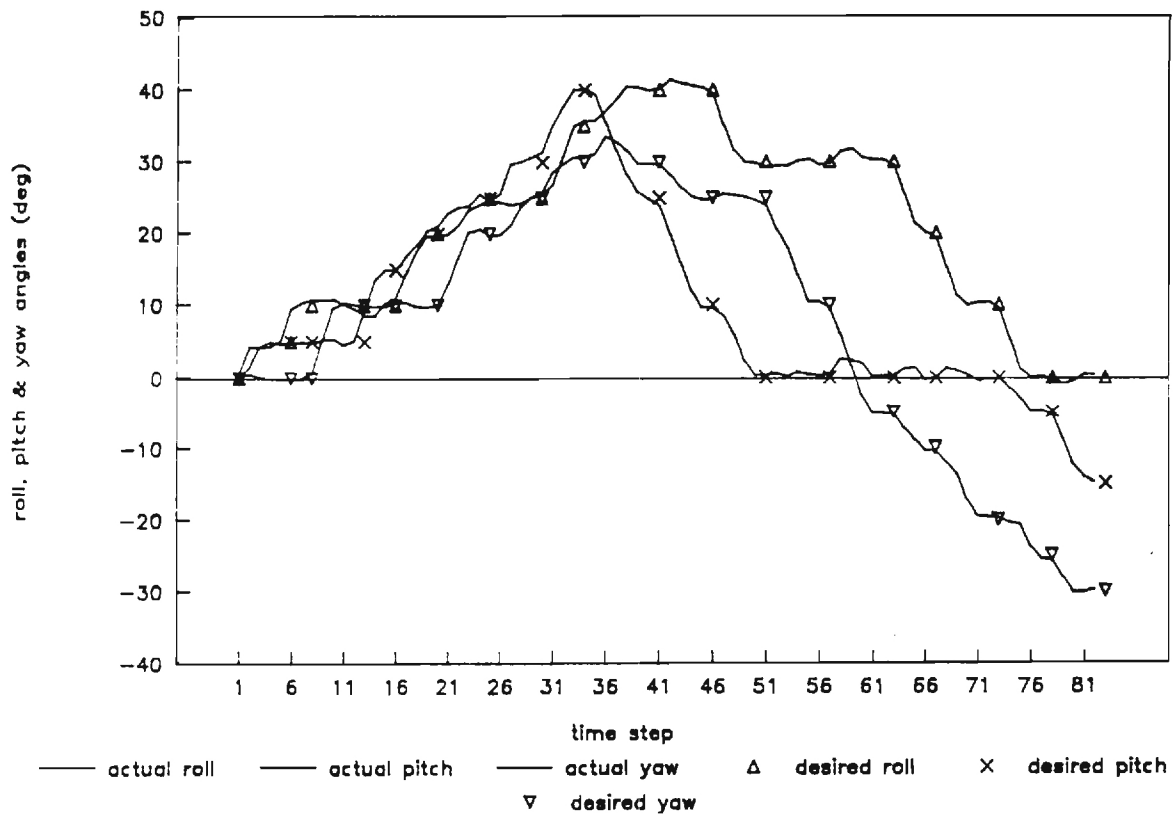


Figure 2.10 Simulation results of trajectory tracking of spherical motor

### 3. RELUCTANCE MODEL

The principle of variable-reluctance can be demonstrated by a simple linear motor scheme shown in Fig. 3.1(a). The coil in the figure represents the stator winding that provides the magnetic field. The iron block represents the rotor. The motion of the rotor is the linear displacement  $x$ . The corresponding magnetic circuit is shown in Fig. 3.1(b), where  $F$  is the magnetomotive force (mmf) of the coil and  $R$  is the reluctance of the system.

When the rotor is subject to a differential displacement  $dx$ , the total electrical energy input  $dW_e$  by the coil is expended to the increase of magnetic field energy  $dW_f$  and to the mechanical work  $dW_m$  done to carry out such a displacement  $dx$ . That is,

$$dW_e = dW_f + dW_m.$$

For a constant  $F$ ,  $dW_f$  is obtained by differentiating  $W_f$  which is represented by the area of the triangle load in Fig. 3.1(c) as  $dW_f = F d\phi/2$ . The total electrical energy increment  $dW_e$  supplied by the coil is  $dW_e = F d\phi$ , represented by the area  $abcd$  in Fig. 3.1(c). Thus, the mechanical work  $dW_m$  is found to be  $dW_m = F d\phi/2$ . From the principle of virtual work, the mechanical force is derived to be

$$f = \frac{dW_m}{dx} = -\frac{1}{2} \left( \frac{F}{R} \right)^2 \frac{dR}{dx}. \quad (3.1)$$

This equation states that the force on the rotor always attempts to move the rotor in the direction of reducing the reluctance of the magnetic circuit, i.e. the direction of increasing the overlapping area of the poles. The prediction of the torque generation of a variable reluctance motor for a given  $F$  requires that reluctance models of the magnetic system to be known.

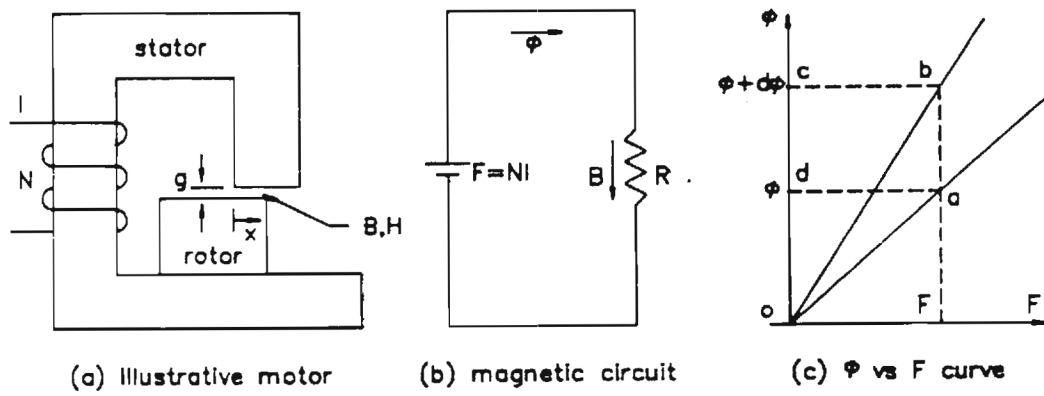


Figure 3.1 A demonstrative linear VR motor

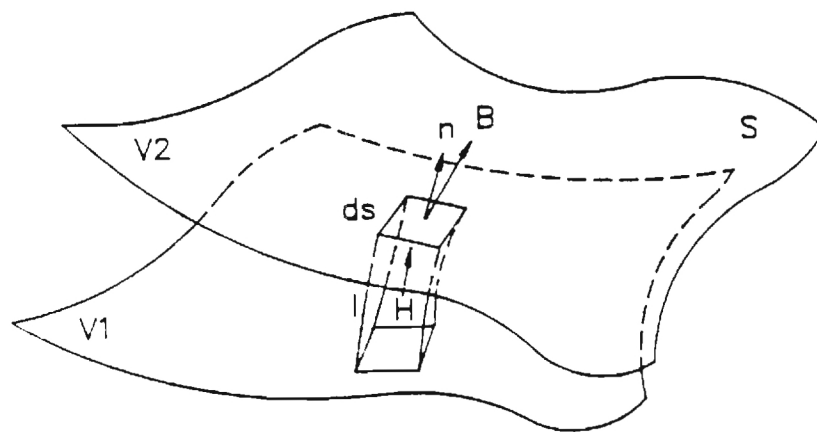


Figure 3.2 A flux tube bounded by two equipotential surfaces

### 3.1 Fundamental Equations

The fundamental equations of magnetostatics, which relate the electromagnetic field and the source quantities of a magnetic field system, are described by the following Maxwell's equations.

$$\nabla \cdot \mathbf{B} = 0 \quad (3.2)$$

$$\nabla \times \mathbf{H} = \mathbf{J} \quad (3.3)$$

where  $\mathbf{B}$  is the flux density,  $\mathbf{H}$  is the magnetic field intensity, and  $\mathbf{J}$  is current density. Equation (3.2) states that the magnetic flux lines are sourceless at any point in the field. Equation (3.3) states that the circulation of the magnetic field at a point is due to the existence of current with density  $\mathbf{J}$  at that point. In addition to these equations, the constitutive law that describe how the physical properties of the materials affect the field is given by  $\mathbf{B} = \mu\mathbf{H}$  where  $\mu$  is the permeability of the material.

Fig. 3.2 illustrates a differential flux tube of cross section  $ds$  and length  $l$  between the two equipotential surfaces, the magnitude of the field intensity  $H$  is

$$H = \frac{V_1 - V_2}{l} \quad (3.4)$$

The differential flux  $d\Phi$  is given as

$$d\Phi = \mu_0 \frac{V_1 - V_2}{l}$$

where  $\mu_0$  is the permeability of air. The total flux  $\Phi$  is the integral of  $d\Phi$  over the entire equipotential surface  $S$ . The reluctance which is the reciprocal of the permeance is defined as

$$R = \frac{V_1 - V_2}{\Phi} \quad (3.5a)$$

or

$$\frac{1}{R} = \mu_o \int_S \frac{ds}{l} \quad (3.5b)$$

where  $(V_1 - V_2)$  has been assumed to be a constant in the derivation of Equation (3.5a). As shown in Equation (3.5b), the permeance is a function of geometry and the computation requires the knowledge of the flux tube (i.e.,  $S$  and  $l$ ).

When the air-gap is much smaller than the dimensions of the adjacent core faces such that fringing at the air gap is negligible, the reluctance of the air-gap can be approximated as

$$R = \frac{l}{\mu_o A_o} \quad (3.6)$$

where  $A_o$  and  $l$  are the overlapping area and the distance between the stator and rotor poles.

#### Permeance-based model

To account for the fringing effects, the shape of the magnetic flux is commonly assumed in modeling the permeance of stepper motors. With an assumed flux shape, the permeance model of an electromagnetic system is determined from Equation (3.5b) with the following assumptions:

1. The iron reluctance is assumed infinite as compared to the air reluctance.
2. No hysteresis or saturation of iron elements in the system. This assumption is reasonable as long as the coil excitations are limited so that the flux density in the iron is within the linear portion of the iron magnetization curve.
3. The assumed flux path is connected to the nearest coil by a straight line and/or a circular arc such that it enters or emerges iron surface perpendicularly and does not cross other flux paths.
4. No magnetic flux leakages between the adjacent stator coils, between the adjacent rotor coils, or in the system.

5. The coil excitations are made such that there are only attraction forces between rotor coils to stator coils. Repulsion between coils generates significant flux leakages. This assumption is also a necessity in order for assumption (4) to be reasonably stated.

A typical flow chart which illustrates the procedure of the static force generation using permeanced-based method is shown in Fig. 3.3.

### Finite-element Methods

Alternatively, the finite-element (FE) method is used to solve numerically for the magnetic field from the Maxwell's equations as outlined in Appendix A. To do so, the Maxwell's equations are first formulated into a Poisson equation either by the vector potential method or by the reduced scalar potential method. The Poisson equation is then implemented by finite element methods to arrive at the magnetic field solution.

A two dimensional model, which is solved by the vector potential formulation, is relatively simple to be solved and therefore is well suitable for cases where the geometrical method is subjected to change. More importantly, two-dimensional model can explicitly give the flux lines by plotting the equipotential lines. However, the two dimensional model ignores the flux distribution in the third dimension. Therefore a two-dimensional model is suitable for qualitative study in the design stage. On the other hand, a three-dimensional model, which is solved by the reduced scalar potential formulation, takes into account of the flux distribution in the third dimension. Thus, it gives a more accurate solution than the two-dimension model.

The finite element solution yields the nodal potential values and the average elemental flux density values. With the knowledge of the fields at hand, the flux through a surface can be calculated using the following summation:

$$\Phi = \sum_S (\underline{B}_i \cdot \underline{n}_i) \Delta S_i \quad (3.7)$$

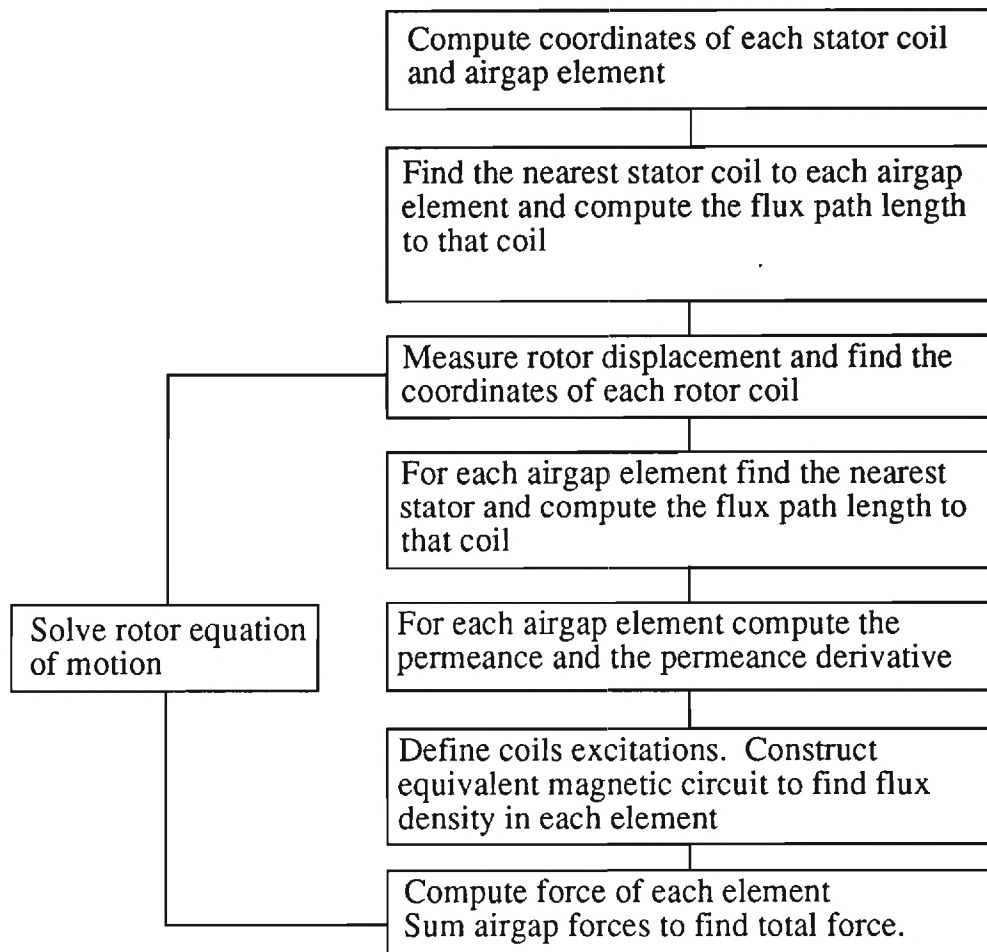


Fig. 3.3 Flow-chart for calculating the model force

where  $\underline{B}_i$ ,  $\underline{n}_i$  and  $\Delta S_i$  are the flux density at the centroid, the unit normal vector, and the surface area of the  $i^{\text{th}}$  element. The useful flux may be divided into three regions. Region 1 is the flux flowing through the overlapping area between the rotor and stator pole which is denoted as  $\Phi_1$ . Region 2 is the rest of the surface of the rotor pole, and region 3 is the cylindrical surface of the rotor pole. The flux flowing through regions 2 and 3 are denoted by  $\Phi_2$  and  $\Phi_3$  respectively. The fringing flux is the sum of the flux flowing through regions 2 and 3, or

$$\Phi_f = \Phi_2 + \Phi_3 \quad (3.8)$$

The reluctance is computed from Equation (3.5a) for a specified potential difference.

### 3.2 Comparison between Permeance-based and Finite-element Models

To obtain some knowledge of coil excitation on flux distributions, magnetic leakages, and reluctance forces, a two-dimensional model of one degree-of-freedom (DOF) linear motion structure as shown in Fig. 3.4 was computed, where the depth dimension is infinite was computed. The magnetic properties of the iron is given in Fig. 3.5. The two-dimensional model is formulated using the vector potential method. The nodal potentials at all other boundary planes which are treated at infinity are set to zero.

The flux distribution computation was performed using the ANSYS finite-element package written by Swanson [20]. The static force generated between the stator and the rotor for a given coil excitation is determined using both the finite-element method and a permeance-based model. To make the two methods comparable, the product of the current density and the coil cross-sectional area is chosen such that it yields the desired magneto-motive-force (mmf).

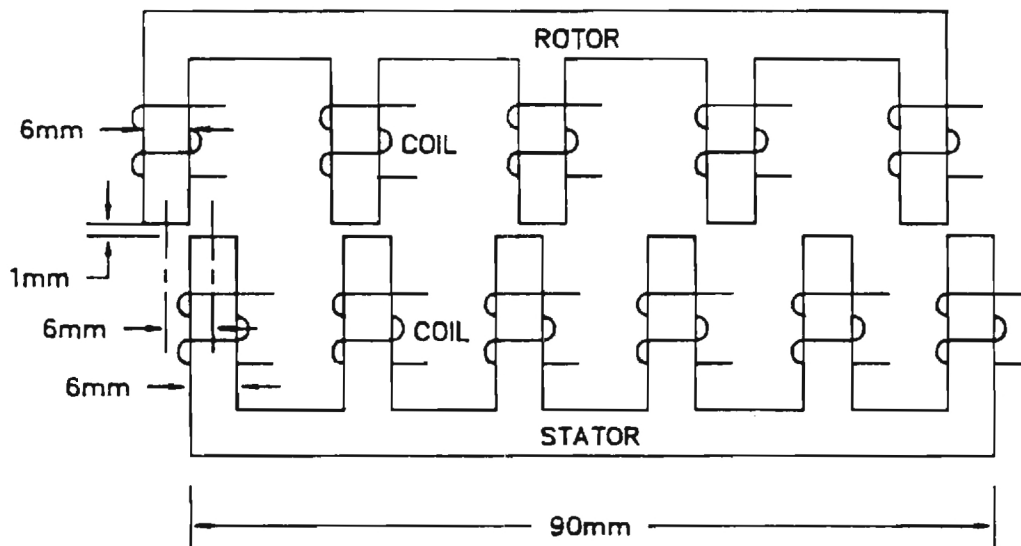


Figure 3.4 2-D multi-pole model of the spherical VR motor

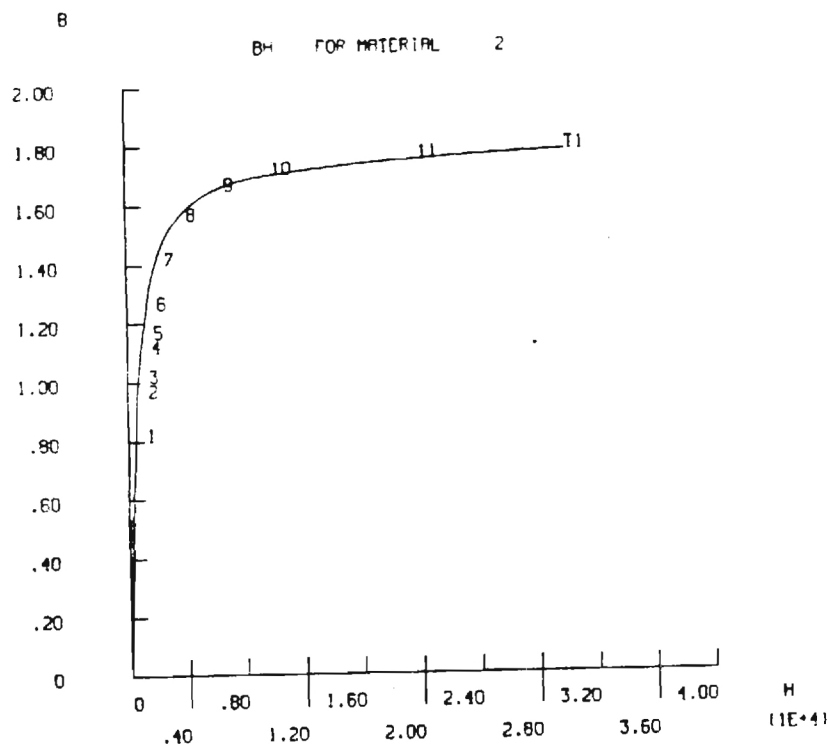


Figure 3.5 B-H curve of soft iron

In the following discussion  $J = (\text{mmf})/A$ , where  $J$  is the current density in Amperes/m<sup>2</sup>; mmf is the magneto-motive-force in Ampere-turns; and  $A$  is the cross-sectional area of the coil in m<sup>2</sup>. In the simulation, the cross-section of the coil on each side is 20mm x 3mm. Thus, 100 Ampere-turns are equivalent to 1.66E+6 Amperes/m<sup>2</sup>. Two different values of iron permeance were used, i.e.  $\mu_i/\mu_o = 1E+3$  and  $1E+7$ . TABLE 3.1 summarizes the result of the computation, where the percentage error listed is relative to the force computed by finite element method. The excitation is indicated as positive if the mmf is directed toward the air gap. The magnitude of each excitation is 100 Ampere-turns. A few selected flux pattern computed using the finite element method is displayed in Fig. 3.6.

Except for Case (5), the permeance-based model yields relatively good approximation when the magnetic materials has a very high permeability. There are three major assumptions which may accumulate significant errors in the permeance-based model:

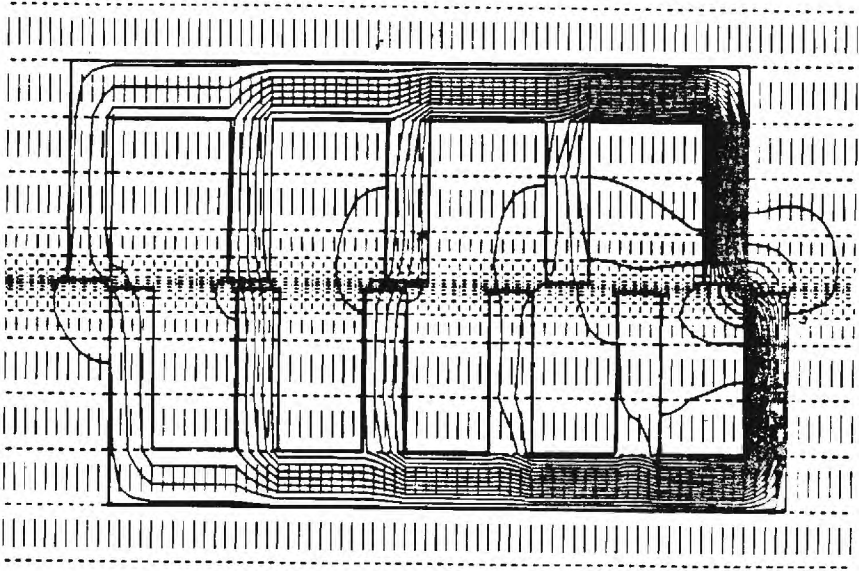
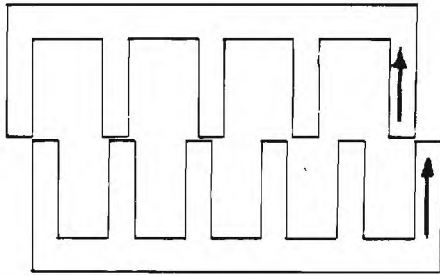
1. The model assumes no reluctance in the iron core.
2. The model neglects leakage paths .
3. The model is inaccurate in describing the flux paths.

The contribution of the first source may be inferred by running modified finite element model using an iron core of very high permeability. As shown in TABLE 3.1, the relative errors in Case (1) are 35.3% and 15.5% with the iron permeance of  $1E+3$  and  $1E+7$  used in ANSYS program respectively. The decrease in relative error can also be observed in all cases, which is consistent with the assumption made in permeance-based model that the reluctance of the iron is negligible or the permeability of the iron is infinite.

Table 3.1  
Comparison between permeance-based model and finite-element model

Case	Model force	Ansys Force Permeance u=1E+3	Error	Ansys Force Permeance u=1E+7	Error
1	16.47	12.17	35.3%	13.52	15.5%
2	10.81	7.81	38.4%	8.79	23.0%
3	10.31	7.90	30.5%	8.82	16.9%
4	63.95	47.68	34.1%	52.33	22.2%
5	-8.02	-4.12	94.7%	4.33	85.2%
6	-5.98	-5.39	10.9%	-5.89	1.5%
7	-26.77	-26.75	0.1%	-28.88	-7.4%

Case 1



Case 2

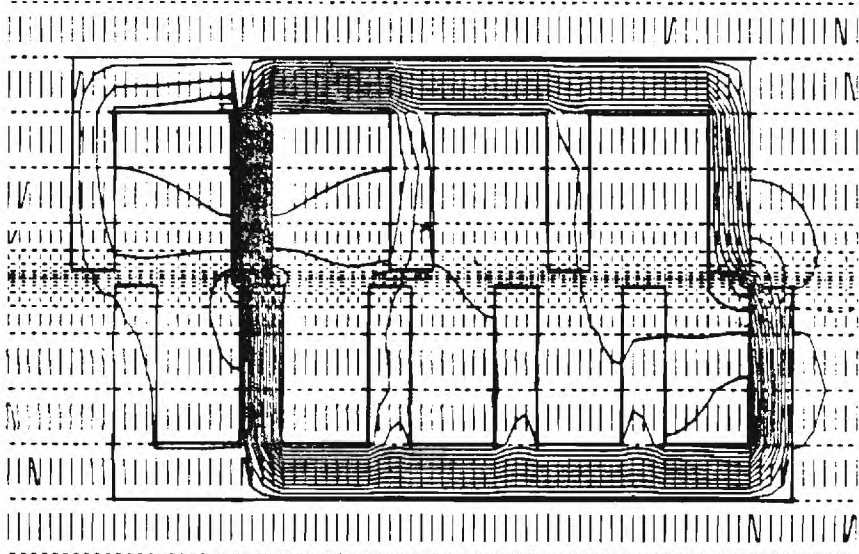
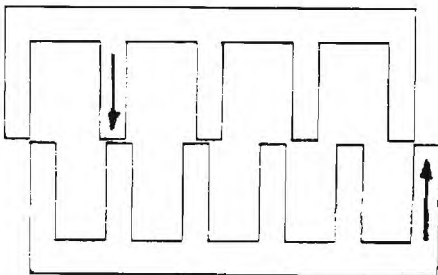
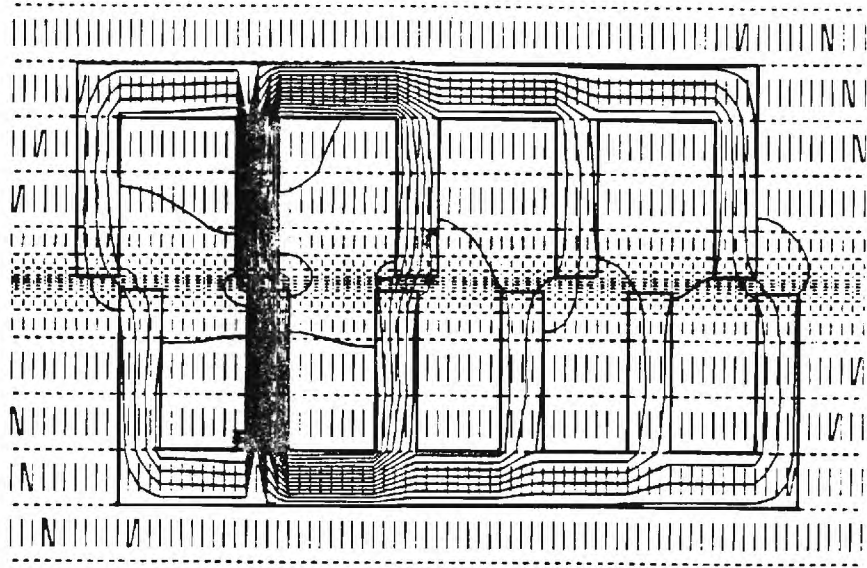
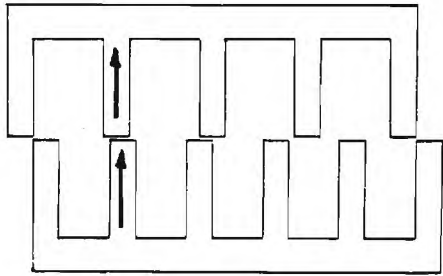


Figure 3.6 Flux of 2-D multi-pole model under leftward excitations

Case 3



Case 4

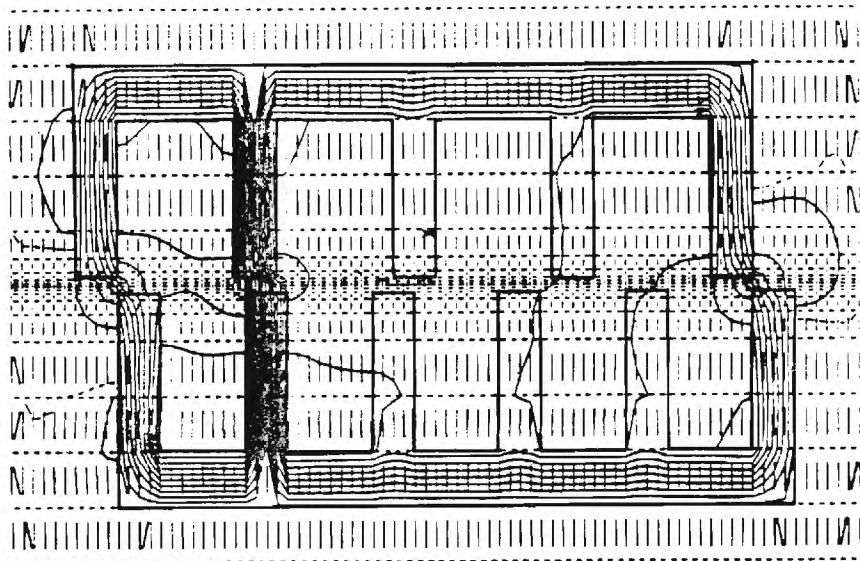
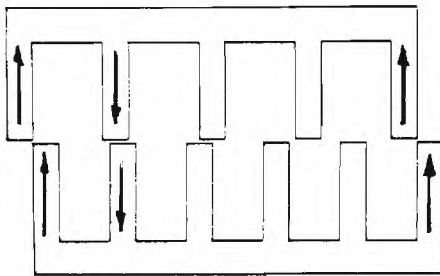
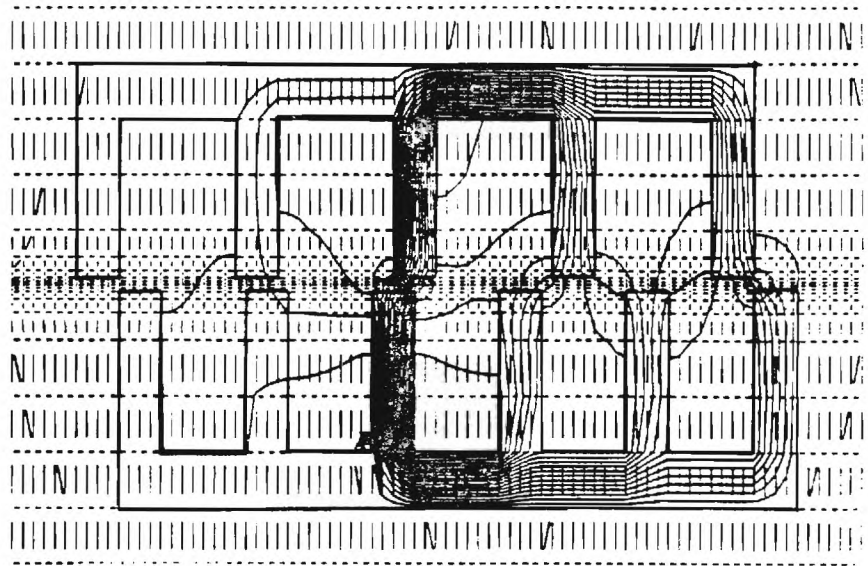
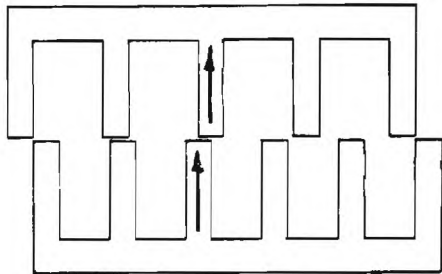


Figure 3.6 Flux of 2-D multi-pole model under leftward excitations

Case 5



Case 6

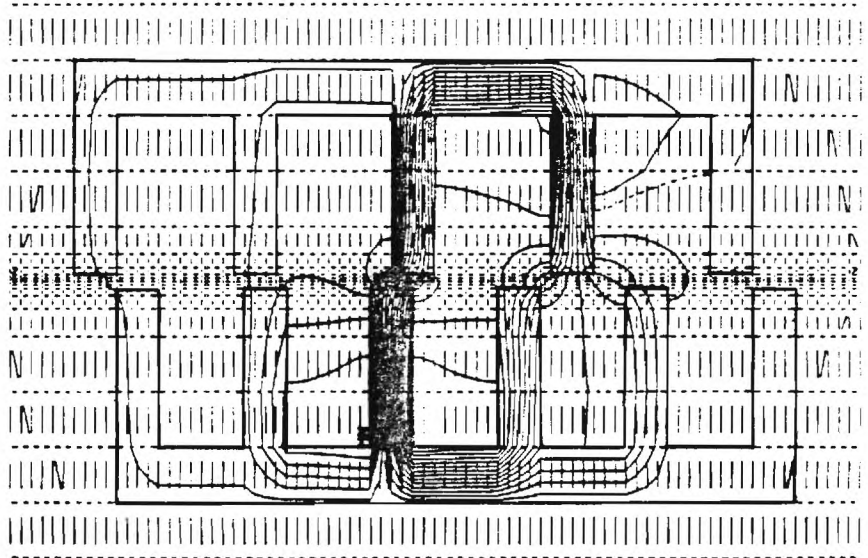
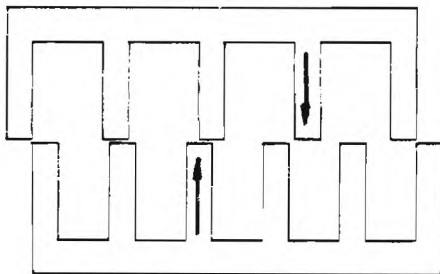


Figure 3.6 Flux of 2-D multi-pole model under leftward excitations

Case 7

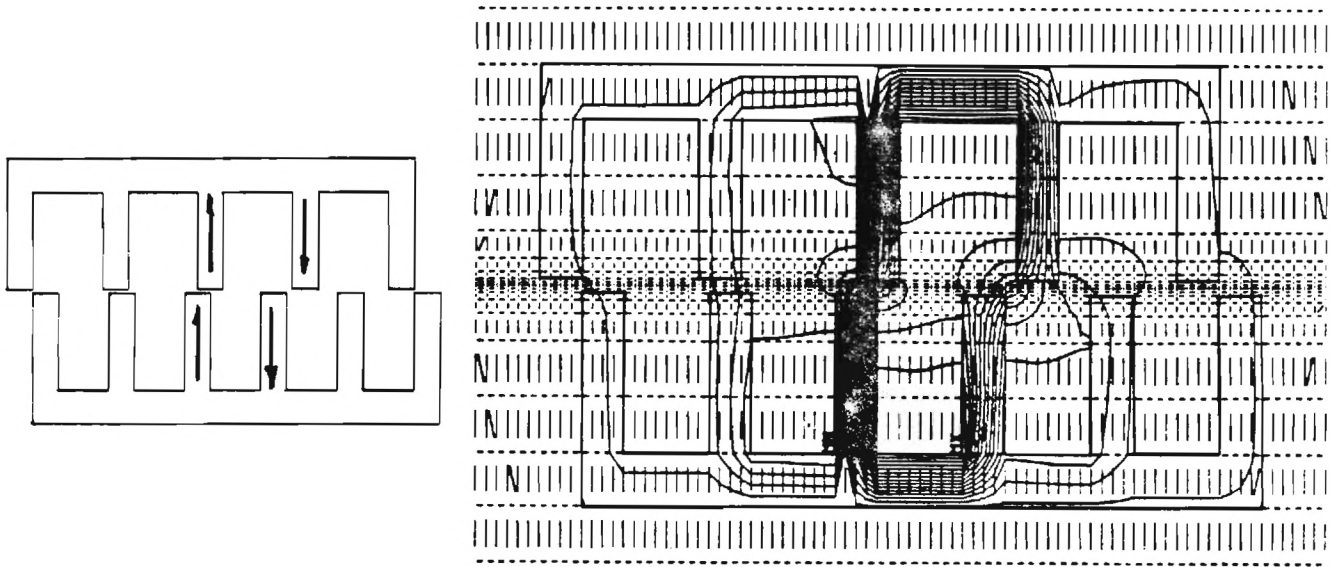


Figure 3.6 Flux of 2-D multi-pole model under leftward excitations

The relative contribution of the second and the third sources to the error is not as obvious. However, the assumption of no magnetic leakages in permeance-based model implies that the flux would generally flow through the excited coils and returns through the remaining poles on both side of electromagnetic structure. As shown in the flux pattern computed for Case (5) demonstrates that the inaccurately assumed flux path may result in a relative error over 90%.

The results have led to the concept of selective magnetic path planning which aims at guiding the magnetic flux to pass through the selected air-gaps in order to optimize the overall reluctance force in the specified direction for a given set of design parameters. The selective magnetic path planning offers the following potential advantages by distributing the input power among a group of coils, each of which contributes a small fraction of total mmf required:

- i. As illustrated in Cases (1) and (7), the force can be significantly increased for a given weight.
- ii. Given the same force-to-weight ratio, the multiple coil excitation in selective magnetic path planning allows lower current per coil but large surface areas for heat dissipation.
- iii. The selective magnetic path planning would tend to result in predictable flux pattern which is a necessity of success for the analytical force prediction using permeance-based model. As illustrated in Case (4) where the input excitation is tripled, the reluctance force increases by a factor of four as compared to Case (1). The significant increase of the reluctance force is the result of a well-shaped magnetic flux path which not only utilizes all the rightward force generating air-gaps but also effectively eliminates the magnetic flux from flowing through the air-gaps which would contribute to the generation of leftward forces.

### **3.3 Finite-element Analysis**

Despite the geometrical modeling difficulty, a three-dimension model is used to solve the flux distribution, especially the fringing flux distribution. Since the reduced scalar potential method does not directly give the flux lines, the solution is represented by the equipotential lines.

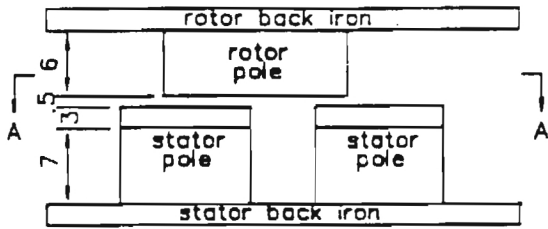
As mentioned before, flux lines can be obtained by drawing line orthogonal to the equipotential lines if no current sources are present.

### 3.3.1 Finite-element models

Two finite element models are discussed in the following analysis; namely, multiple-pole configuration and a single pole-pair configuration. The objectives are to predict the magnetic field distribution and the sensitivity of the fringing flux distribution, the air-gap reluctance to the changes of the geometrical parameters, and the allows the reluctance force comparison to be made between the finite element method and the experimental results. In addition, a reluctance model as a function of displacement is presented, which would provide a rational basis of reluctance force modeling.

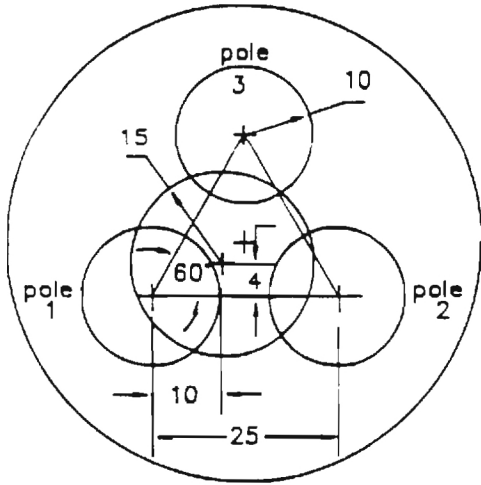
Fig. 3.7 shows a planar magnetic structure consisting of a rotor pole and three stator poles along with basic geometry, where the location of the three stator poles form an equilateral triangle. The distance between any two adjacent pole boundaries is ten times greater than the air-gap spacing and the model is assumed to be magnetically isolated from the rest of the spherical motor. In addition, as the pole sizes are relatively small as compared to the corresponding surface of a spherical motor, it is expected that the finite element result based on the planar structure would not differ significantly from the spherical structure.

In general, the flux lines are not orthogonal to the equipotential lines except when the current sources  $\mathbf{H}_s$  are absent from the system. Thus, the stator poles are excited using permanent magnets instead of electromagnetic coils in order to simplify the air gap reluctance calculation in the finite-element analysis.

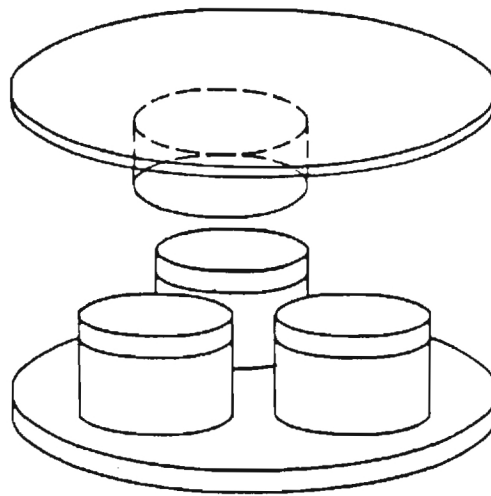


a

View A-A



b



c

Figure 3.7 Model of a section of the spherical VR motor

Permanent magnets, however, have different magnetic properties from the core material, the magnetic field in the air gap would be different from that of an air gap bounded by two iron cores. Thus, a 3-millimeter-thick iron cap is placed on the magnet as illustrated in Fig. 3.8 so that the magnetic field solution around the air-gap is independent of the type of excitation. The demagnetization curve (i.e. the third quadrant of the hysteresis loop of the permanent magnet) and the normalized B-H curve of the iron structure are given in Figs. 3.9. Three different cases of excitations are illustrated along with the boundary conditions in Fig. 3.10, which are denoted as up-none, up-up, and up-down excitations. In all three excitations, the first stator pole was excited such that the flux through the first stator pole would flow towards the rotor and the third stator pole was unexcited. The second stator pole is not excited in the up-none excitation and is excited to have the same polarity as the first pole in the up-up excitation and opposite polarity in the up-down excitation. Since the magnetic model is isolated from the rest of the spherical motor, the cylindrical boundary surface satisfies the Dirichet boundary condition and the nodal potentials on the boundary are set to zero. The top and bottom boundaries of the model, however, vary from one excitation configuration to another. For the cases where the second stator pole is not excited or is excited to have the same polarity as the stator pole 1, the nodal potentials of the bottom and top boundary surfaces are set to zero, in which case the flux flows perpendicularly to the bottom and top surfaces. However, when the polarity of the stator pole 2 is in the opposite direction of stator pole 1 in the up-down excitation, the flux is expected to circulate between stator poles 1 and 2 via the rotor pole. In other words, the fluxes in the back irons of the stator and the rotor are assumed to be parallel to the bottom and upper boundary surfaces. Thus, the top and bottom boundaries satisfy the Normann boundary conditions when the stator poles 1 and 2 are excited in opposite direction.

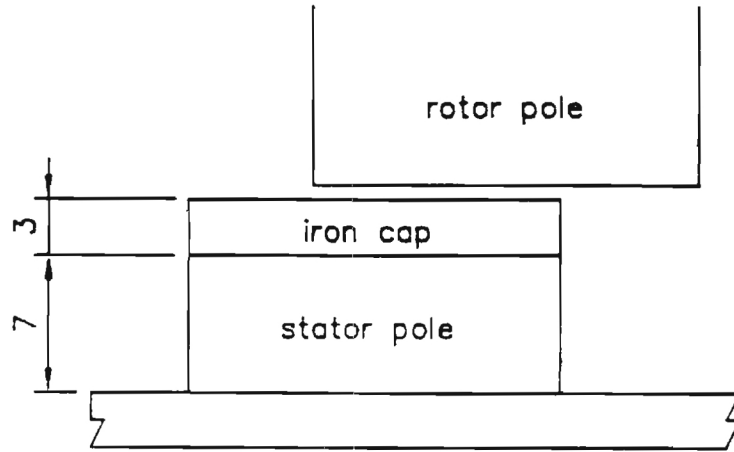


Figure 3.8 An iron cap shielded airgap

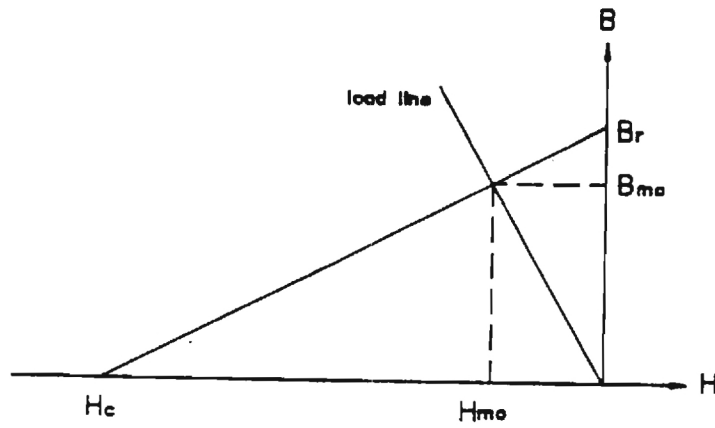
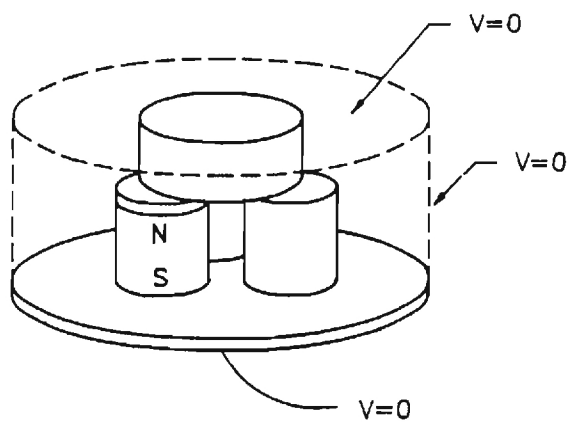
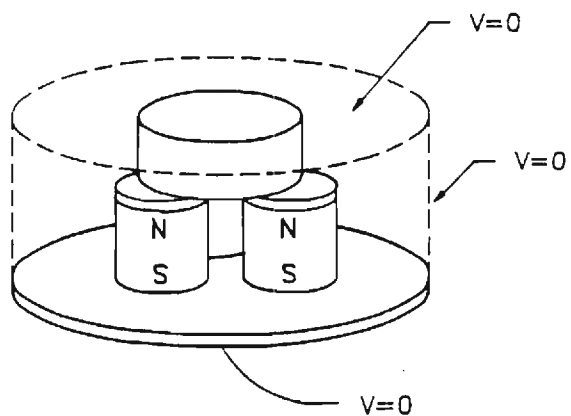


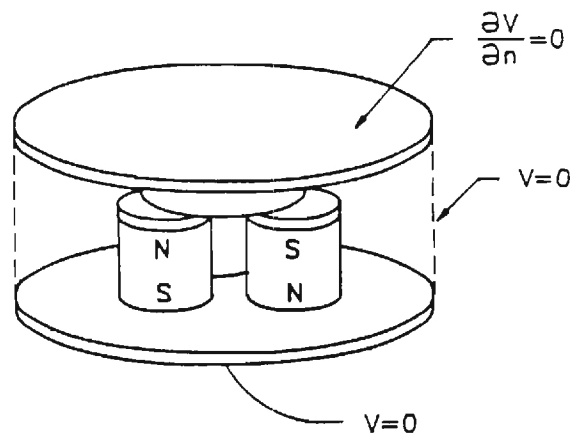
Figure 3.9 Demagnetization of the permanent magnet



(a)



(b)



(c)

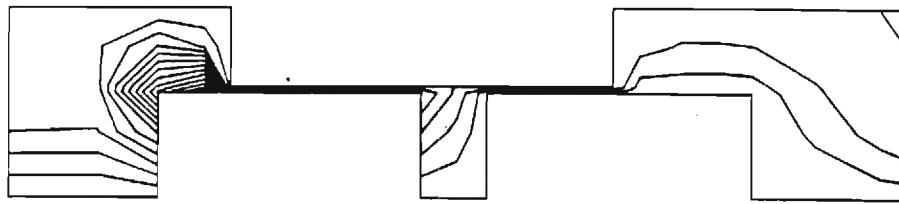
Figure 3.10 Boundary settings for the basic three pole model

The values of the air-gap spacing and the stator pole length are 0.5 mm and 6mm. In order to examine the sensitivity of the flux distribution and the air-gap reluctance to the geometrical parameters, two additional finite element computations have been made, one with the air-gap spacing of 1 mm and the other with the stator pole length of 30mm.

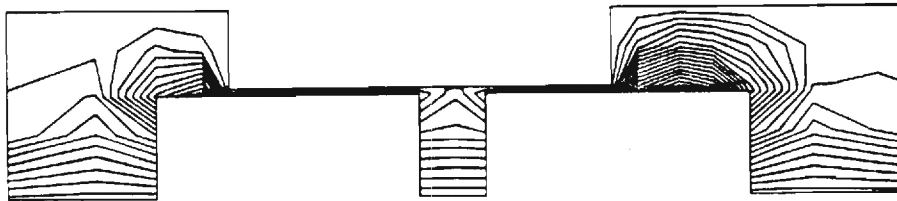
### 3.3.2 Results and discussions

In each of these finite-element computations, all other dimensions were unchanged and only the up-none excitation was applied as shown in Fig. 3.10(a). The results are tabulated in TABLE 3.2. Fig. 3.11 indicates that the magnet surface is not equipotential without the iron cap. The effect of the iron cap on the magnetic flux apparently serves to provide an uniform flux distribution at the air gap and thus the corresponding reluctance of region 1 can be closely estimated using Equation (3.6). Due to the nonuniform potential at the magnetic stator pole face, the reluctance of the overlapping area without the iron cap is about 7% smaller than 1.85. The average potential value has been used in computing the air-gap reluctance. The percentage of the fringing flux, however, is not remarkably sensitive to the presence of the iron cap.

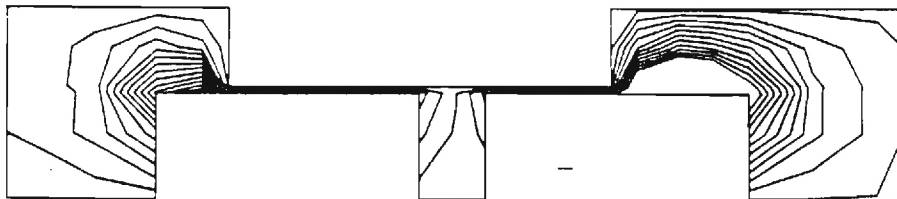
The fringing flux accounts for over 25 percent of the useful flux in the air-gap. The percentage of the fringing flux increases from 26.7% to 31.7% as the air-gap spacing is doubled. Therefore, negligence of the fringing flux would under-estimate the air-gap flux and reluctance estimation. However, the fringing flux is relatively insensitive to the adjacent coil excitation. Thus, when the pole-separation to air-gap ratio is greater than 10, the influence of magnetic field in one air gap on the other may be neglected. The result reasonably justifies the previously stated assumption that the magnetic model as shown in Fig. 3.6 may be treated as an isolated section from the rest of the spherical motor. The assumption significantly reduce the complexity of the spherical motor modeling using finite element method.



(a) up-none excitation



(b) up-up excitation



(c) up-down excitation

Figure 3.11 Side cut-away view of the equipotential lines of the basic three pole model

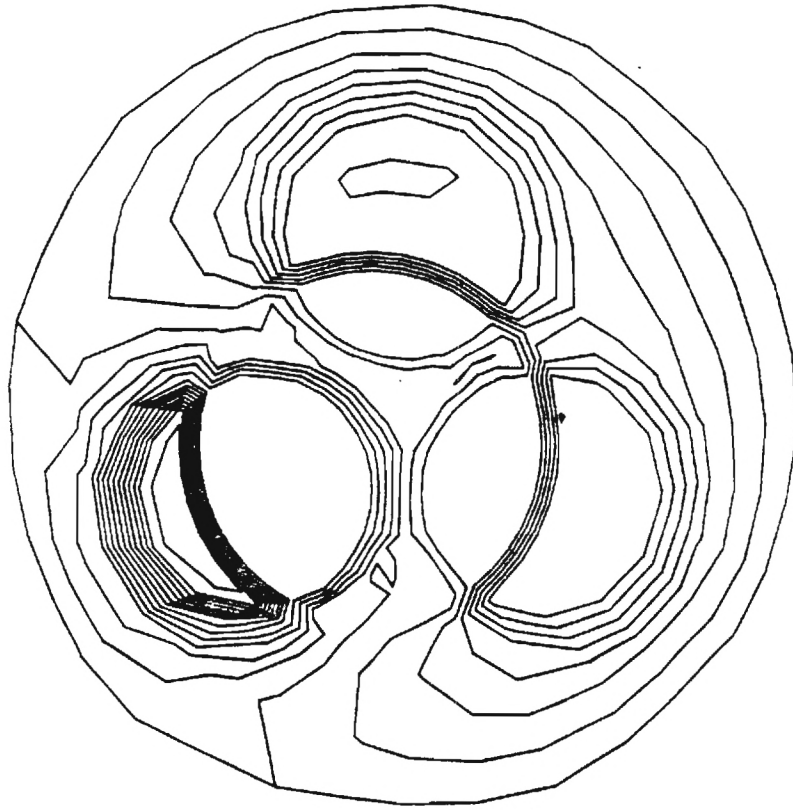


Fig. 3.11(d) Top view of air gap equipotentials of the basic three pole mode

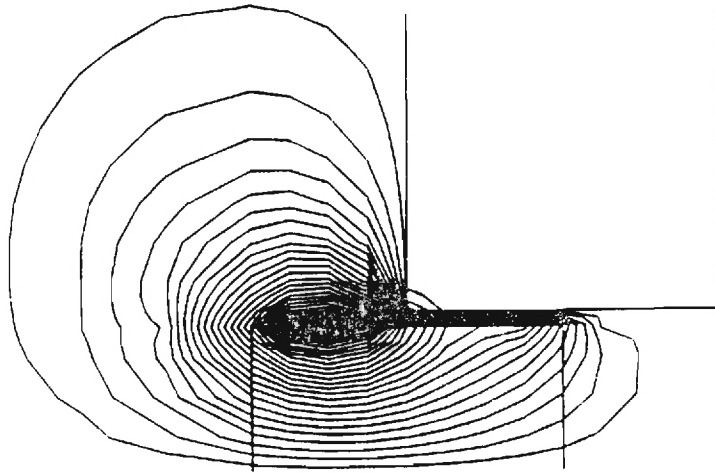


Figure 3.12 (a) Finite element result of potential distribution

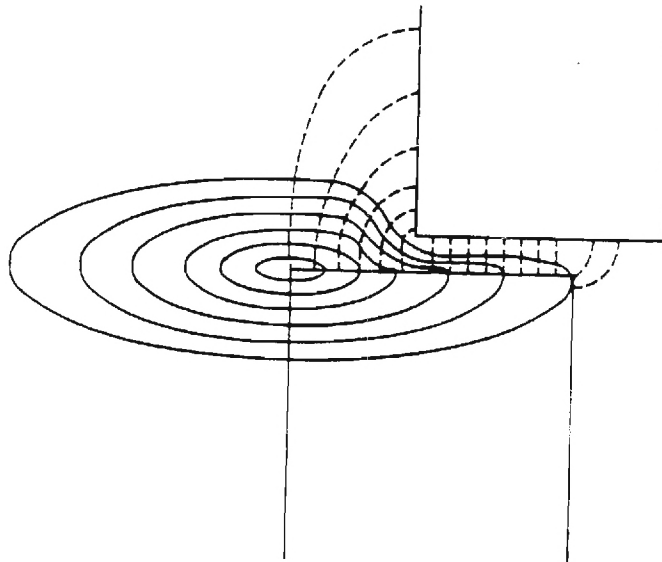


Figure 3.12 (b) Traditional assumption of potential distribution

Table 3.2. FE results of the basic and the non-capped three pole models

Model	Basic three pole model			Non-capped three pole model		
	up-no	up-up	up-dn	up-no	up-up	up-dn
Potential at bottom $V_1$	360	420	380.00	351.19	313.66	387.55
Potential at top $V_2$	10	120	10.00	4.77	3.44	31.28
Gap potential drop $V_1 - V_2$	350	300	370.00	346.42	310.22	356.27
Region 1 flux $\Phi_1$ ( $\times 10^{-6}$ )	189.67	162.22	199.75	197.13	178.43	203.25
Region 2 flux $\Phi_2$ ( $\times 10^{-6}$ )	58.97	48.33	63.95	48.97	39.15	53.72
Region 3 flux $\Phi_3$ ( $\times 10^{-6}$ )	10.09	7.82	11.21	19.02	15.26	22.05
Fringing flux $\Phi_f = \Phi_2 + \Phi_3$	69.06	56.15	75.15	67.99	54.41	75.77
Gap flux $\Phi = \Phi_1 + \Phi_2 + \Phi_3$	258.64	218.37	274.91	265.12	232.84	279.02
Percent fringing flux (%)	26.7	25.7	27.3	25.6	23.4	27.2
Overlap reluct. $\mathcal{R}_{lap}$ ( $\times 10^6$ )	1.845	1.849	1.852	1.766	1.739	1.753
Fringing reluct. $\mathcal{R}_f$ ( $\times 10^6$ )	5.068	5.343	4.923	5.095	5.702	4.702
Total gap reluct. $\mathcal{R}$ ( $\times 10^6$ )	1.353	1.374	1.346	1.307	1.332	1.277

Note: The estimated main reluctance  $\widetilde{\mathcal{R}}_{lap}$  of the overlapping area is  $1.85 \times 10^6$ .

The equipotential plot of the fringing flux in region 2 forms a constant-width band as illustrated in Fig. 3.11. where the potential is represented by the loops in solid line and the flux is represented by the dashed lines. The commonly assumed flux path in stepper motor modeling is shown in Fig. 3.12, which generally neglects the magnetic flux leakages and predicts the point of maximum potential at the edge of the stator pole. In contrast, the influences of the leakage fluxes can be clearly visualized from the equipotential plot of the finite-element analysis.

TABLE 3.3 summarizes the computation results of two other configurations. In the large gap model, the air gap between the stator and the rotor poles is increased from 0.5 mm to 1 mm. All other dimensions are given in Fig. 3.6. Similarly, in the long rotor pole model, the length of the rotor pole is modified from 6 mm to 30 mm. As shown in TABLE 3.3, as the air gap width increased by a factor of 2, the main flux in region 1 has been reduced significantly whereas the fringing flux has been increased from 26.7% to 31.7%.

The increase of rotor pole length from 6 mm to 30 mm does not have significant effect on the fringing flux. This is because the fringing flux mainly distributes around the end of the rotor pole. Therefore, in the design of the spherical motor, small rotor pole aspect ratio may be applied to achieve a compact structure. This model shows that an aspect ratio of 0.2 is satisfactory.

### 3.4 Reluctance Model

The flux distribution and hence the reluctance model of the air gap depend on the geometry of the structure and is a function of the displacement. In order to allow the following quantities, namely, the total flux  $\Phi_t$  flowing through the magnet, the airgap flux  $\Phi_g$ , and the leakage flux  $\Phi_l$  to be modelled, the magnetic structure as shown in Fig. 3.13 has been analyzed.

Table 3.3. FE results of the large air gap model and the long rotor pole model

Model	large gap model	long rotor pole model
Excitation type	up-none	up-none
Potential at bottom $V_1$	555.00	360.00
Potential at top $V_2$	5.00	10.00
Gap potential drop $V_1 - V_2$	550.00	350.00
Region 1 flux $\Phi_1 (\times 10^{-6})$	148.67	189.58
Region 2 flux $\Phi_2 (\times 10^{-6})$	55.00	58.85
Region 3 flux $\Phi_3 (\times 10^{-6})$	14.06	12.88
Fringing flux $\Phi_f = \Phi_2 + \Phi_3$	69.06	71.73
Air gap flux $\Phi = \Phi_1 + \Phi_2 + \Phi_3$	217.75	261.31
Percent fringing flux(%)	31.7	27.5
Main reluctance $\mathcal{R}_{over} (\times 10^6)$	3.699	1.846
Fringing reluctance $\mathcal{R}_f (\times 10^6)$	7.964	4.879
Total gap reluctance $\mathcal{R} (\times 10^6)$	2.526	1.339

**Note:** The estimated main reluctance  $\widetilde{\mathcal{R}}_{lap}$  of the overlapping area for the big gap model is  $3.695 \times 10^6$ .

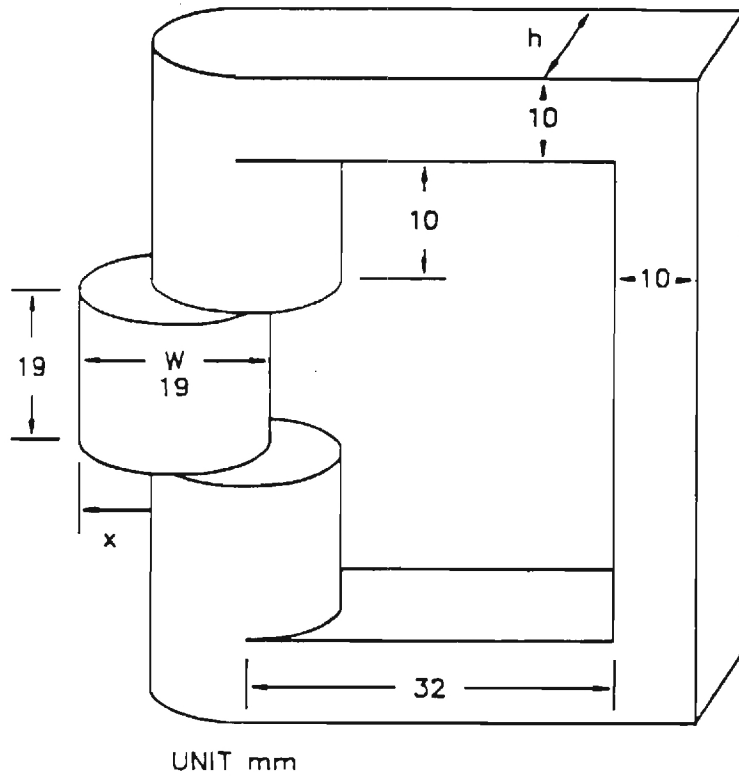


Figure 3.13 3-D model with permanent magnet

The magnetic properties of the permanent magnet and the iron are given in Fig. 3.14. Due to the symmetry of the structure, the total flux  $\Phi_t$  is given by that flowing through the middle cross-section of the permanent magnet. The flux flowing across the air gap consists of two portions; namely the airgap flux passing through the overlapping area between the permanent magnet and the iron structure, and the fringing flux which include the remaining flux from the permanent magnet towards the iron. The leakage flux can be computed from the continuity of flow,

$$\Phi_l = \Phi_t - \Phi_g$$

Since the system is symmetrical about x-y plane and x-z plane, only a quarter of the magnetic system is meshed and computed. The nodal potentials on the x-z plane of symmetry, satisfy the Neumann boundary condition and that on the x-y plane of symmetry satisfy the Dirichet boundary condition. The distances from the far boundaries to the structure are at least 15 times the width of the air gap which is 0.5 mm, therefore they are treated as at infinity and the nodal potentials are set to zero.

The equipotentials in the center plane of the pole are plotted in Fig. 3.17, which show the equipotentials at three normalized displacements 0, 0.5 and 1. The total flux  $\Phi_t$  is calculated by Equation (3.5a) where the integration surface is taken as the elements of the middle cross-section of the magnet. Similarly, the air gap flux  $\Phi_g$  is calculated by taking the integration surface as the layer of elements that encloses the pole. The leakage flux  $\Phi_l$  is the difference between the total flux  $\Phi_t$  and the air gap flux  $\Phi_g$ . The three flux values are given in TABLE 3.4 for three normalized displacements 0, 0.5, and 1.0.

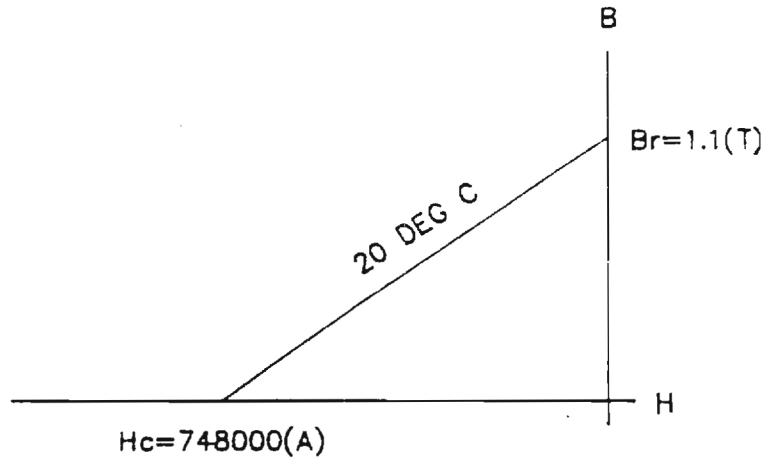


Figure 3.14 (a) Normalized demagnetization curve of permanent magnet

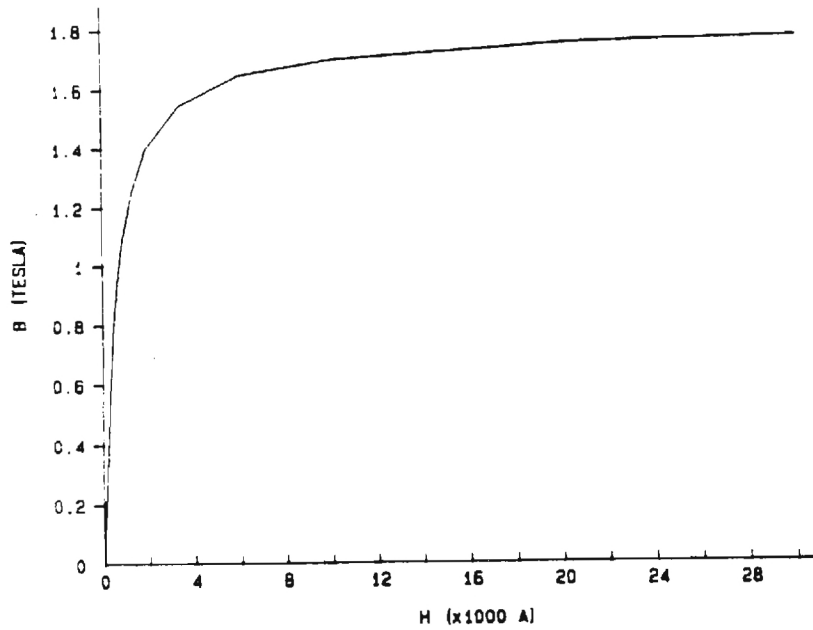
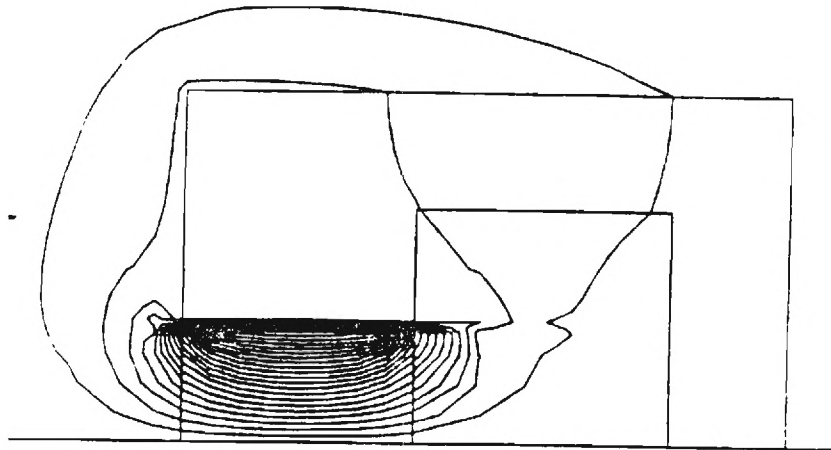
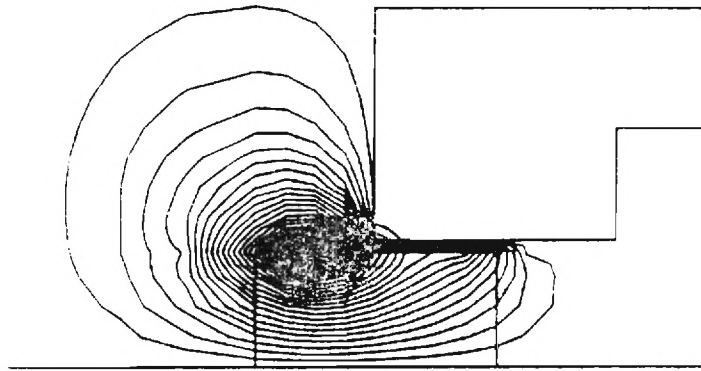


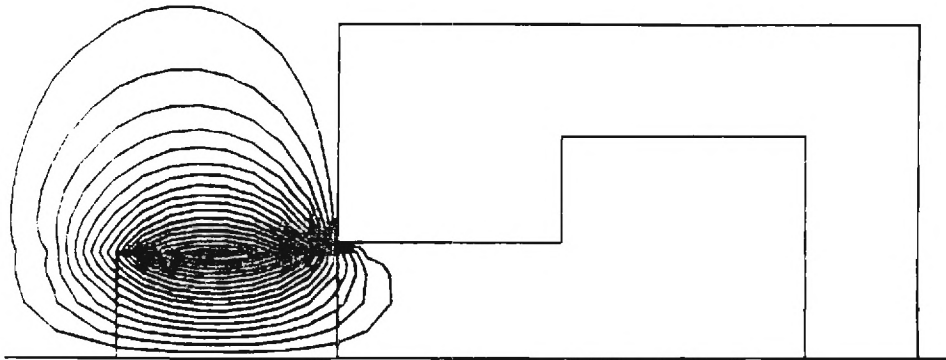
Figure 3.14 (b) Characteristic of soft iron



(a) Equipotentials at center plane at  $\bar{z} = 0$



(b) Equipotentials at center plane at  $\bar{z} = 0.5$



(c) Equipotentials at center plane at  $\bar{z} = 1$

Figure 3.15 Equipotentials of 3-D model with permanent magnet

Table 3.4. Flux in the 3D model with permanent magnet

Displacement $x$ (mm)	0	10	20
Normalized disp $\tilde{x}$	0	0.50	1.00
B value at magnet pole (T)	0.921	0.802	0.596
Air gap potential drop ( $\Delta V$ )	725	1237.5	2800
Total flux $\Phi_t$ ( $\times 10^{-3}$ Wb)	.165	.155	.137
Air gap flux $\Phi_g$ ( $\times 10^{-3}$ Wb)	.145	.112	.048
Leakage flux $\Phi_l$ ( $\times 10^{-3}$ Wb)	.020	.043	.089
Percentage leakage (%)	12	27.7	65
Air gap reluctance $\mathcal{R}_g$ ( $\times 10^6$ )	4.897	11.049	58.300
Air gap permeance $P_g$ ( $\times 10^{-6}$ )	.204	.091	.017

The permeance based on Equation (3.6) and the three-dimensional permeance are found to have the same shape as shown in Fig. 3.16 where the two models are compared. However, the difference between these two curves grows greater as the normalized pole distance increases the pole overlapping area decreases and the proportion of fringing flux increases.

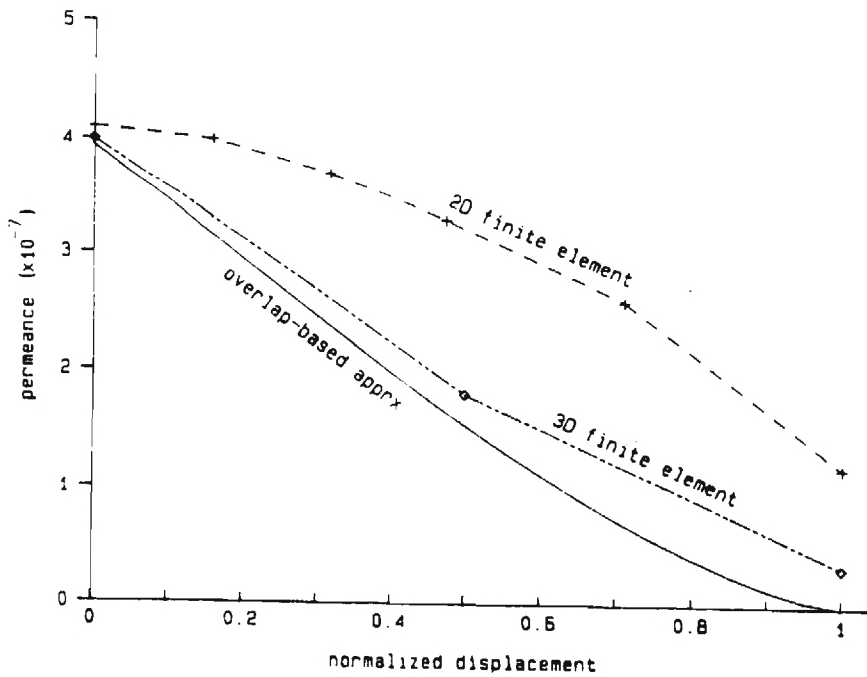


Figure 3.16 Comparison of airgap permeance of 2-D and 3-D models

## 4. ANALYTICAL MODEL OF TORQUE PREDICTION

The electro-magnetic phenomena are governed by Maxwell's equations as discussed in the previous section. For a specific problem where the geometries, the material properties, and the boundary conditions are well defined, the Maxwell's equations represent the model of a distributed parameter system. In deriving an analytical model of the spherical motor for motion control law development, it is desired to reduce the relatively complex magneto-quasi-static field of spherical geometry to a tractable form. In this section, both the forward and inverse torque prediction model of the spherical motor using a lumped-parameter approach are derived.

### 4.1 General Formulation

The following assumption are made in the derivation of the spherical model:

1. The reluctance of the iron core is negligible as compared to that of the airgap. The error introduced by this assumption depends on the geometrical dimensions of the structure and the permeability of the material. This error, in general, can be significantly reduced with magnetic material of high permeability and with small airgap.
2. The spacing between any adjacent rotor poles and that between any adjacent stator poles is assumed to be much larger compared to the airgap. This assumption implies that no leakage flux occurs between adjacent stator (or rotor) poles.
3. The magnetic circuit of the spherical motor is modelled using a lumped-parameter approach analogous to the linear electric circuit. The linearized model allows the flux flowing through the reluctance of airgaps to be considered separately. Thus, the reluctance of the magnetic circuit can be determined from the reciprocal of the permeance derived in the previous section.

The magnetic system as shown in Fig. 4.1 is considered in the derivation of the torque prediction model of the spherical motor consisting of  $m$  active rotor coils and  $n$  active stator coils. The torque generated by the magnetic system is governed by the principle of conservation of energy, which yields:

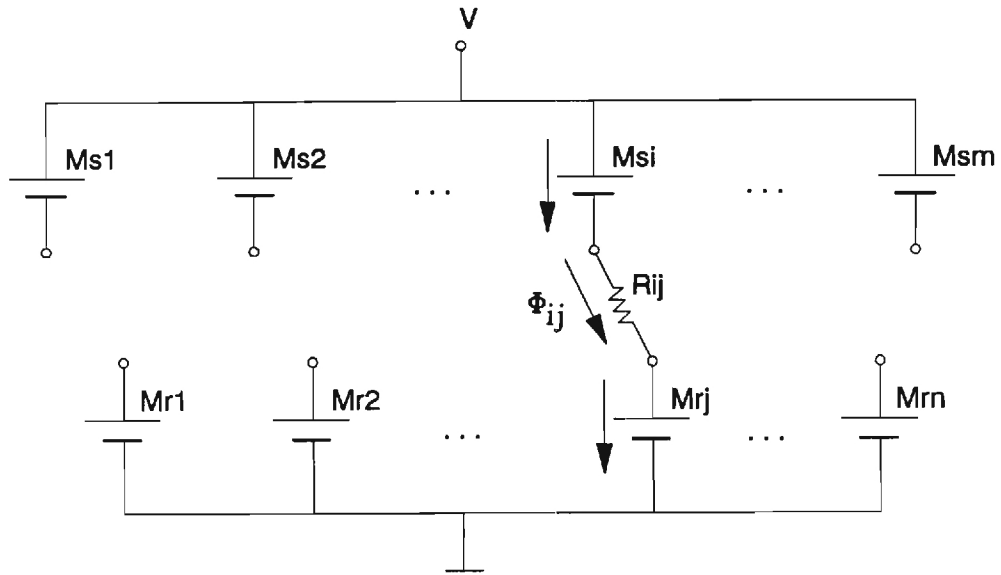


Figure 4.1 Magnetic circuit of the spherical VR motor

$$\dot{E}_m(t) = \dot{E}_e(t) - \mathbf{T}(t) \cdot \omega(t) \quad (4.1)$$

where

$\dot{E}_m$  = time rate of magnetic energy stored,

$\dot{E}_e$  = electrical power input,

$i_n$  = current through the  $n^{\text{th}}$  excited coil,

$\lambda_n$  = flux linkage through the  $n^{\text{th}}$  excited coil,

$\mathbf{T}$  = resultant torque acting on the rotor, and

$\omega$  = angular velocity of the rotor.

### Electrical power input

The rate of change of the total electrical input to the system is given by

$$\dot{E}_e = \sum_{i=1}^m \sum_{j=1}^n (M_{si} + M_{rj}) \dot{\Phi}_{ij} \quad (4.2)$$

where  $\Phi_{ij}$  is the flux flowing through the airgap between  $i^{\text{th}}$  stator coil and  $j^{\text{th}}$  rotor coil; and  $M_{si}$  and  $M_{rj}$  are the mmf generated by the  $i^{\text{th}}$  stator coil and the  $j^{\text{th}}$  rotor coil respectively. From Fig. 4.1, the magnetic flux  $\Phi_{ij}$  flowing through the air-gap separating the  $i^{\text{th}}$  rotor coil and the  $j^{\text{th}}$  stator coil is given by

$$\Phi_{ij} = P_{ij} [M_{si} + M_{rj} - V] \quad (4.3)$$

where  $P_{ij}$  is the permeance of the air-gap between the  $i^{\text{th}}$  stator coil and the  $j^{\text{th}}$  rotor coil, and  $V$  is the magnetic potential at the rotor core. Since

$$\sum_{i=1}^m \sum_{j=1}^n \Phi_{ij} = 0, \quad (4.4)$$

the magnetic potential at the rotor core  $V$  can be derived by substituting  $\Phi_{ij}$  from Equation (4.3) into Equation (4.4), which leads to

$$V = \frac{\sum_{i=1}^m \sum_{j=1}^n P_{ij} (M_{si} + M_{rj})}{\sum_{i=1}^m \sum_{j=1}^n P_{ij}} \quad (4.5)$$

Noting that the time derivative of the flux  $\Phi_{ij}$  can be determined from Equation (4.3), the electrical power input to the system is given by Equation (4.6):

$$\dot{E}_e = \sum_{i=1}^m \sum_{j=1}^n \{ (V - M_{si} - M_{rj})^2 \dot{P}_{ij} + P_{ij} (M_{si} + M_{rj}) (\dot{M}_{si} + \dot{M}_{rj}) \} \quad (4.6)$$

#### Rate of change of magnetic energy

The total magnetic energy stored in the system is

$$E_m = \frac{1}{2} \sum_{i=1}^m \sum_{j=1}^n \Phi_{ij}^2 R_{ij} \quad (4.7)$$

where the flux is given by Equation (). By substituting the time rate of change of magnetic flux  $\Phi_{ij}$ , the corresponding time-rate of change in the magnetic energy stored in the airgap is derived as

$$\dot{E}_m = \sum_{i=1}^m \sum_{j=1}^n \left\{ \frac{1}{2} (M_{si} + M_{rj} - V)^2 \dot{P}_{ij} + P_{ij} (M_{si} + M_{rj} - V) (\dot{M}_{si} + \dot{M}_{rj}) \right\} \quad (4.8)$$

From Equations (4.6) and (4.8), it follows that

$$\dot{E}_e - \dot{E}_m = \frac{1}{2} \sum_{i=1}^m \sum_{j=1}^n (M_{si} - M_{rj} - V)^2 \dot{P}_{ij} \quad (4.9)$$

### Mechanical Power

Since the mechanical power can be re-written as:

$$\mathbf{T} \cdot \boldsymbol{\omega} = \sum_{k=1}^3 T_k \dot{\phi}_k \quad (4.10)$$

where  $\phi_1$ ,  $\phi_2$ , and  $\phi_3$  are the angles that the rotor rotated about the the axes of rotor body frame. Using the result from Equations (4.1), (4.9), and (4.10), and noting that the differentials of  $\phi_1$ ,  $\phi_2$ , and  $\phi_3$  are independent of each other, the torque generated by the magnetic system is given by

$$\mathbf{T} = \nabla (E_e - E_m) \quad (4.11)$$

where

$$\nabla = \left( \frac{\partial}{\partial \phi_1} \right) \mathbf{u}_1 + \left( \frac{\partial}{\partial \phi_2} \right) \mathbf{u}_2 + \left( \frac{\partial}{\partial \phi_3} \right) \mathbf{u}_3$$

## 4.2 Forward Torque Prediction Model

The forward torque prediction model is to determine the torque generated by the spherical motor for a given set input currents applied to the electromagnetic coils. As discussed in previous section, the torque generated depends on the permeance of the electromagnetic system. For a specified spherical motor structure, the permeance between any pair of the stator pole and rotor pole is a function of the distance between the two poles. As shown in Figure 4.4 for the case of rotation, the separation angle between the  $i^{\text{th}}$  stator pole and the  $j^{\text{th}}$  rotor pole is denoted as  $\phi_{ij}$ . Hence,

$$P_{ij} = P(\phi_{ij}) \quad (4.12)$$

If  $\mathbf{C}_{si}(x_{si}, y_{si}, z_{si})$  and  $\mathbf{C}_{rj}(x_{rj}, y_{rj}, z_{rj})$  are the position vectors of  $i^{\text{th}}$  stator coil and the  $j^{\text{th}}$  rotor coil originating from the center of spherical motor respectively, the angle between the  $i^{\text{th}}$  rotor coil and  $j^{\text{th}}$  coil can be determined from the dot product of the position vectors,  $\mathbf{C}_{si}$  and  $\mathbf{C}_{rj}$ , or

$$\cos(\phi_{ij}) = \frac{\mathbf{C}_{si} \cdot \mathbf{C}_{rj}}{R^2} \quad (4.13)$$

where the position vector of the  $j^{\text{th}}$  rotor coil is defined by

$$\begin{bmatrix} \mathbf{C}_{rj} \\ 1 \end{bmatrix}_{XYZ} = [T] \begin{bmatrix} \mathbf{c}_{rj} \\ 1 \end{bmatrix}_{123}, \quad (4.14)$$

[T] is a homogeneous transformation describing the rotor frame with respect to stator frame, and  $\mathbf{c}_{rj}$  describe the position vectors of  $j^{\text{th}}$  rotor pole with respect to the rotor frame. It can be shown that the torque generation can be computed from Equation (4.11), which leads to

$$\mathbf{T} = \frac{1}{2} \left[ \sum_{i=1}^m \sum_{j=1}^n (M_{si} - M_{ri} - V)^2 \cdot \left. \frac{dP(\phi)}{d\phi} \right|_{\phi=\phi_{ij}} \right] \mathbf{e}_{ij} \quad (4.15)$$

where  $\mathbf{e}_{ij}$  is an unit vector perpendicular to the position vectors  $\mathbf{C}_{si}$  and  $\mathbf{C}_{rj}$  and can be derived from differential geometry to be

$$\mathbf{e}_{ij} = \frac{\mathbf{C}_{si} \times \mathbf{C}_{rj}}{R^2 \sin \phi_{ij}}. \quad (4.16)$$

Thus, Equation (4.15), along with Equations (4.5) and (4.16) and the permeance model, defines the torque generated by the spherical motor for a given set of inputs in terms of the magnetomotive-forces (MMF's) of the coils.

### Remark 1

The torque generation equation given by Equation (4.15) is quadratic with respect to  $(M_{si}, i=1, \dots, m)$  and  $(M_{rj}, j=1, \dots, n)$ . In controlling the electromechanical devices, either current or voltage sources may be used. If the current source is used, the MMF of each coil is simply the ampere-turns, i.e. the product of the current and the number of turns in each coil, and the torque prediction model of a current-controlled spherical VR motor remains to be an algebraic quadratic function of the currents through the coils.

However, if a voltage source is used for each stator coil of  $N$  turns and with a coil resistance of  $r_e$ , then

$$u_{si} = M_{si} \frac{r_e}{N} + N \frac{d}{dt} \sum_{j=1}^n \Phi_{ij} \quad (4.17a)$$

where  $u_{si}$  is the voltage supplied to the  $i^{\text{th}}$  stator coil. Similar expression can be derived for the voltage input to the  $j^{\text{th}}$  rotor coil

$$u_{rj} = M_{rj} \frac{r_e}{N} + N \frac{d}{dt} \sum_{i=1}^m \Phi_{ij} \quad (4.17b)$$

Substituting Equations (4.3) - (4.5) into Equation (4.17) and noting that

$$\frac{d}{dt} P_{ij}(\phi_{ij}) = \frac{dP(\phi)}{d\phi} \cdot \frac{d}{dt} \phi_{ij} \quad (4.18)$$

which is velocity related. Equation (4.17) is essentially a set of differential equations in terms of  $(M_{si}, i=1, \dots, m)$  with time-varying coefficients due to the coupled velocities. Equations (4.15) and (4.17) constitute the torque prediction model of a voltage-controlled spherical VR motor. Unlike the current-controlled spherical VR motor for which the torque generation is described by a set of algebraic equations, the torque generation of a voltage-controlled spherical VR motor is

represented by a set of dynamic equations which coupled the electromagnetics with the motion dynamics through the velocity.

Thus, it is desired to use current sources for a spherical VR motor in order to ease the task of designing the motion controller for the spherical motor.

Remark 2

The physical meaning of Equation (4.15) can be interpreted as follows: Equation (4.14) represents the magnetic energy  $E_m$  in the electromagnetic field, which is a form of potential energy. From Equation (4.15), the torque may be viewed as the spatial gradient of a scalar field.

Moreover, consider each pair of stator-rotor poles is treated separately. If the magnetic energy stored in an airgap between the  $i^{th}$  stator pole and the  $j^{th}$  rotor pole is  $E_{ij}$ , the vector

$$\mathbf{T}_{ij} = \frac{1}{2} (M_{si} - M_{rj} - v)^2 \cdot \left. \frac{dP(\phi)}{d\phi} \right|_{\phi=\phi_{ij}} \mathbf{e}_{ij} \quad (4.19)$$

can be thought as the torque generated by this particular pole pair. The direction of this torque is such that the two poles are attracted to each other in order to reduce the magnetic energy stored.

The summation of Equation (4.19) over all  $i = 1, \dots, m$  and  $j = 1, \dots, n$  gives Equation (4.15).

Remark 3

Consider that the rotor poles of the spherical motor are driven by permanent magnets instead of electromagnetic coils. In general, the reluctances of the permanent magnets and hence the leakage flux cannot be ignored. If the  $j^{th}$  permanent magnet of the rotor is characterized by a mmf  $M_{pj}$  and a reluctance  $r_{pj}$ , the  $j^{th}$  magnetic driver may be represented by an equivalent reluctance in series with an equivalent mmf  $M_{rj}$  as

$$M_{rj} = \frac{r_{lj} M_{pj}}{r_{pj} + r_{lj}} \quad \text{and} \quad R_{rj} = \frac{r_{lj} r_{pj}}{r_{pj} + r_{lj}} \quad (4.20)$$

where  $r_{rj}$  is the reluctance to the leakage flux of the  $j^{\text{th}}$  permanent magnet. However, the magnetic flux  $\Phi_{ij}$  flowing through the air-gap separating the  $j^{\text{th}}$  rotor coil and the  $i^{\text{th}}$  stator coil is flux dependent, which is given by

$$\Phi_{ij} = P_{ij} [M_{si} - R_{rj} \sum_{k=1}^m \Phi_{kj} - M_{rj} - V]. \quad (4.21)$$

The magnetic potential at the rotor core  $V$  can be derived by substituting  $\Phi_{ij}$  from Equation (4.21) into Equation (4.4), which yields

$$V = \frac{\sum_{i=1}^m \sum_{j=1}^n P_{ij} \left[ (M_{si} + M_{rj}) + R_{rj} \sum_{k=1}^m \Phi_{kj} \right]}{\sum_{i=1}^m \sum_{j=1}^n P_{ij}} \quad (4.22)$$

Thus, the corresponding flux  $\Phi_{ij}$  can be determined from the following system of linear equation

$$[A] \underline{\Phi} = \underline{b} \quad (4.23)$$

where

$$\underline{\Phi} = [\Phi_{11}', \Phi_{12}', \dots, \Phi_{1n}; \Phi_{21}', \Phi_{22}', \dots, \Phi_{2n}; \dots; \Phi_{m1}', \Phi_{m2}', \dots, \Phi_{mn}]^T$$

In order to determine the flux flowing through an airgap, a system of  $m \times n$  equations in the form of Equation (4.23) must be solved simultaneously. Similar argument can be made for the case where the reluctance of the magnetic core of stator coils cannot be ignored.

### 4.3 Inverse Torque Prediction Model

The inverse torque prediction model is to compute a set of coil excitations, which is denoted here as a control input vector  $\mathbf{U}$ , that is required to generate the desired torque. Unlike the forward torque prediction model which yields an unique torque vector for a specified set of coil excitations, there are generally infinite number of solutions to the inverse torque prediction model of a spherical VR motor which would produce a specified torque. To simplify the derivation, the following additional assumptions are made:

1. In practice, it is desired to have no wiring in the moving parts and thus, only iron cores or permanent magnets are used as magnetic poles in the rotor. The presence of permanent magnets, however, generally introduces reluctances and magnetic leakages which result in complicated electromagnetic model. Thus, it is assumed that  $M_{Tj} = 0$  for  $j = 1, \dots, n$ . The assumption implies that there are not control variables in rotor.
2. To simplify the derivation, it is assumed that only current sources are used and that the MMF's of the coil are treated as system input variables.

#### 4.3.1 Matrix Representation

In order to obtain an optimal solution to the inverse torque prediction model, the torque equation is presented in quadratic form using the following notations:

$$\mathbf{U} = [M_{S1} \quad \dots \quad M_{Sm}] \in \mathbb{R}^m, \quad (4.24)$$

$$\mathbf{a} = [a_1 \quad \dots \quad a_i \quad \dots \quad a_m]^T, \quad (4.25)$$

$$a_i = \frac{\sum_{j=1}^n P_{ij}}{\sum_{i=1}^m \sum_{j=1}^n P_{ij}}, \quad \sum_{i=1}^m a_i = 1 \quad (4.26)$$

and

$$\mathbf{c}_i = [0 \quad 0 \quad \dots \quad 1 \quad 0 \quad 0]^T \quad (4.27)$$

i.e. except the  $i^{\text{th}}$  element which is equal to 1, all other elements of  $\mathbf{c}_i$  are equal to 0. Clearly, the sum of  $\mathbf{a}_i$  over  $i = 1, \dots, m$  is unity. Hence, using the notations defined by Equations (4.24) to (4.27), the torque can be written in matrix form as follows:

$$\tau_k = \frac{1}{2} \mathbf{U}^T [\mathbf{A}_I] \mathbf{U} \quad I = 1, 2, 3 \quad (4.28)$$

where

$$[\mathbf{A}_I] = \sum_{i=1}^m \left[ \sum_{j=1}^n \left. \frac{dP(\phi)}{d\phi} \right|_{\phi=\phi_{ij}} (\mathbf{e}_{ij} \cdot \underline{\mathbf{u}}_I) \right] (\mathbf{a} - \mathbf{c}_i) (\mathbf{a} - \mathbf{c}_i)^T \quad (4.29)$$

where  $(\mathbf{u}_I, I=1,2,3)$  is an unit vector along the axes of the rotor baby frame.

#### Property

The matrix obtained above have the following property: Define  $\mathbf{U}_e = [1, 1, \dots, 1]^T \in \mathbb{R}^m$ , then

$$[\mathbf{A}_I] \mathbf{U}_e = 0 \quad (4.30)$$

which means summing the column vectors over each matrix resulting a zero vector. This can be verified as follows: Define  $\delta_{ik} = 1$  if  $i=k$  or 0 otherwise. Then the elements of  $[\mathbf{A}_I]$  can be written as

$$A_{Ik\ell} = \sum_{i=1}^m \left[ \sum_{j=1}^n \left. \frac{dP(\phi)}{d\phi} \right|_{\phi=\phi_{ij}} (\mathbf{e}_{ij} \cdot \underline{\mathbf{u}}_I) \right] (a_k - \delta_{ik}) (a_\ell - \delta_{i\ell}) \quad (4.31)$$

By summing Equation (4.31) over  $(\ell = 1, \dots, m)$ ,

$$\sum_{\ell=1}^m A_{Ik\ell} = \sum_{i=1}^m \left[ \sum_{j=1}^n \left. \frac{dP(\phi)}{d\phi} \right|_{\phi=\phi_{ij}} (\mathbf{e}_{ij} \cdot \underline{\mathbf{u}}_I) \right] (a_k - \delta_{ik}) \sum_{\ell=1}^m (a_\ell - \delta_{i\ell}) \quad (4.32)$$

Using Equation (4.26) and the definition of  $\delta_{ik}$ , the right-hand-side of Equation (4.32) can be readily shown to be zero. Since for any  $\alpha \in \mathbb{R}$ , which implies

$$[\mathbf{A}_k] (\alpha \mathbf{U}_e) = 0, \quad (4.33)$$

the property means that if all the control variables have a same value, no torque will be generated. The property can also be seen from Fig. 4.1 where if all MMF's are the same no flux will be generated. In other words, adding a constant to all components in  $\mathbf{U}$  does not change the torque  $T$ .

#### 4.3.2 Formulation for Inverse Torque Model

The derivations in the previous subsection have established the model for predicting the torques for given control inputs. Given the desired torque,  $\mathbf{U}$  may be determined from Equation (4.28) by solving the algebraic equations. However, since  $\mathbf{U} \in \mathbb{R}^m$  where  $m$  is the number of stator coils sufficiently large integer as compared to three, the degrees-of-freedom of the spherical motor, there are generally infinite numbers of solutions to the inverse problem. It is of interest to determine an optimal solution by some guidelines or a criterion, such as one minimizing of the current amplitude or the consumed power. In other words, the inverse torque prediction is essentially an optimization problem, which may be formulated as follows:

$$\text{Minimize } \sum_{i=1}^m |u_i|^p \quad \text{where } p > 0 \quad (4.34)$$

subjected to constraints imposed by Equation (4.28).

Typical values of  $p$  are 1, 2 and  $\infty$ . When  $p$  is chosen as 1, the sum of the current amplitude is minimized. If the consumed power of the electrical circuit is to be minimized,  $p$  equal to 2 may

be assigned. For the case where the maximum amplitude of the current is to be minimized,  $p$  is set to infinity.

The generalized reduced gradient (GRG) method [21] [22], is used to solve for the optimal solution, which is well known to be an effective way in solving the nonlinear programming problem [23] [24]. However, it is difficult to find a feasible point and to proceed within the feasible region, the GRG method is not suitable for the problem with equality constraints. Therefore, the inverse problem (4.34) is reformulated as an unconstrained problem. The equality constraint problem can be converted to the unconstrained problem in two ways; namely the use of Lagrange multipliers and the addition of penalty terms.

#### Formulation I

$$\text{Minimize } f(\mathbf{U}, \lambda) = \sum_{i=1}^m |u_i|^p + \sum_{I=1}^3 \lambda_I \left( \frac{1}{2} \mathbf{U}^T [\mathbf{A}_I] \mathbf{U} - T_I \right) \quad (4.35)$$

where  $\lambda_1, \lambda_2,$  and  $\lambda_3$  are the Lagrange multipliers.

#### Formulation II

$$\text{Minimize } f(\mathbf{U}) = \sum_{i=1}^m |u_i|^p + M \sum_{I=1}^3 \left( \frac{1}{2} \mathbf{U}^T [\mathbf{A}_I] \mathbf{U} - T_I \right)^2 \quad (4.36)$$

where  $M > 0$  and  $M$  is a very large real number. It has been shown that under some very general conditions, the solution to the problem formulation II approaches the solution to the original inverse problem (4.34) as  $M \rightarrow \infty$ . The problem formulation I is unbounded since  $\lambda$ 's can be chosen such that the objective function has arbitrarily large amplitude with minus sign. Therefore, the gradient-based method would fail to find the stationary points. On the other hand, the problem represented by the formulation II is bounded and a global optimal solution exists

since  $f(\mathbf{U}) \geq 0$  for all  $\mathbf{U} \in \mathbb{R}^m$ . It has been numerically found that the GRG method works well in solving Formulation II.

### 4.3.3 Implementation of the inverse torque model

The average running time to solve an optimal solution represented by Problem (4.36) using an off-the-shelf optimization software [25] is about 1 minute on a Intel 80386 25 MHz computer. The typical sampling rate in the control of an electromechanical systems is in the order of 1KHz. In other words, if the inverse torque model is to be implemented in real-time, it is necessary that all computations should be completed within 1 msec. For real time applications, a look-up table may be pre-compiled using off-line computation. The following discussion addresses practical issues related to the design of the look-up table for real time implementation, which fits the practical memory size.

The table size is determined by the number and the range of variables. Since the matrices  $([\mathbf{A}_I], I=1,2,3)$  vary with the orientation of the spherical motor, the table should typically consists of three torque components and three independent position coordinates. Therefore, the dimensions of the table will be six. If all of the variables are simply put together into the table, the table size will be enormously large as illustrated in the following example.

Consider eleven stator coils to be individually controlled. Each of the control inputs require two bytes for representation. If each of six system variables (three torque and three position coordinates) is characterized by 20 points over the entire range (which is still rough), the total number of points would be  $20^6$  or  $64 \times 10^6$ . Each point would require  $11 \times 2 = 22$  bytes to store an input vector  $\mathbf{U}$ . The memory needed would exceed 1300 Mbytes.

### Table Size Reduction by Parameter elimination

To reduce the table size, first notice that (4.49) is a quadratic function, the torque is proportional to  $\|U\|^2$ , where  $\|U\|^2 = U^T U$ . Therefore, it is possible that the table only contains the results for  $|T|=1$ , since for other values of  $T$ , the control inputs can be obtained by scaling. Now there are only two independent components for  $T$  of unity amplitude, the dimensions of the table is reduced by 1.

This is still far from satisfactory. A more efficient way is to eliminate all the torque variables in the table. Several approaches along with their advantages and shortcomings are discussed as follows: Let  $U_1$ ,  $U_2$ , and  $U_3$  be the control inputs computed off-line from the inverse torque model which would produce the unit torque components  $T_1$ ,  $T_2$  and  $T_3$  about the three axes of the rotor body frame respectively. For each rotor position which is characterized by three independent position coordinates, the three input vectors  $U_1$ ,  $U_2$ , and  $U_3$  are stored in the precompiled table.

(A) For a specified torque of any arbitrary direction, the input vector  $U$  is given by

$$U = \alpha U_1 + \beta U_2 + \gamma U_3 . \quad (4.37)$$

Given the three coordinates of the spherical motor, the three input vectors  $U_1$ ,  $U_2$ , and  $U_3$  corresponding to the input vectors required to generate a specified torque with respect to the rotor body frame respectively, are determined from the table. The coefficients  $(\alpha, \beta, \gamma)$  are computed from a set of three nonlinear simultaneous equations, which are obtained by substituting Equation (4.37) into Equation (4.28). Thus, the required control input can be solved from Equation (4.37). In this approach, only the three input vectors ( $U_1$ ,  $U_2$ , and  $U_3$ ) are required to be stored for each rotor position and thus the torque variables are eliminated.

(B) This approach is similar to the approach (A), but in solving  $U_1$ ,  $U_2$ , and  $U_3$ , six more constraints are added:

$$[A_J] U_I = 0 \quad (4.38)$$

for  $J \neq I$  where  $I, J = 1, 2, 3$

which makes all cross terms zero when Equation (4.37) is substituted into Equation (4.28). Therefore without solving for  $(\alpha, \beta, \gamma)$ ,  $U$  can be directly written as

$$U = \sum_{I=1}^3 \sqrt{T_I} U_I \quad (4.39)$$

As in approach (A), only  $U_1$ ,  $U_2$ , and  $U_3$  are required to be stored for each rotor position.

- (C) In this approach, the sampling period is divided into three segments  $t_1$ ,  $t_2$  and  $t_3$  such that the sum of  $t_1$ ,  $t_2$ , and  $t_3$  is equal to a specified sample time. The control inputs  $U_1$ ,  $U_2$ , and  $U_3$  are applied to the system during the time intervals  $t_1$ ,  $t_2$ , and  $t_3$  respectively. Since  $(t_1, t_2, \text{ and } t_3)$  can be chosen to be proportional to the desired  $(T_1, T_2, T_3)$ , the result effect of the control inputs to the system will yield an output torque approximately equal to the specified  $T(T_1, T_2, T_3)$ .

Consider the same example where the spherical motor consists of eleven stator coils and 20 points are used to characterize each of the three position coordinates. The total number of points required to be stored in the look-up table would be  $(20^3 \times 11 \times 3 \times 2 \text{ bytes})$  or 528 Kbytes in all three approaches (A), (B) and (C). The memory space required for the table is reduced by a factor of 8000 as a result of eliminating the three torque components as parameters.

Among the approaches, (C) requires a minimum amount of computation and is easiest to realize. However, the actual trajectory resulted from approach (C) may not be very smooth, and the abrupt change in  $U$  in a fraction of a specified sampling time may cause a very high voltage in coils. The approach (A), on the other hand, requires an on-line computation of  $(\alpha, \beta, \gamma)$  from a set of three non-linear simultaneous equations. By imposing six additional constraints to the inverse torque model,  $U$ , the approach (B) aims at reaching a near optimal solution to eliminate the on-line computation of  $(\alpha, \beta, \gamma)$ , which implies more currents (or more power consumed) than (A) are required to generate a specified torque.

### Table Size Reduction by Use of Symmetry

Since the torque variables are eliminated from the table, the variables in the table are only the position coordinates, namely, Eulerian angles. Further reduction of the look-up table can be achieved by using the pole location symmetry of the spherical motor to reduce the range of position variables. The following example illustrates the method.

Consider a spherical motor where eleven poles on the stator are arranged according to the apices of an icosahedron. The rotor has four evenly spaced poles. The stator and rotor poles are listed in TABLEs 4.1 and 4.2 respectively. The corresponding ranges of the Eulerian angles are as follows:

precession:	$0 \leq \psi \leq 2\pi$
nutation:	$0 \leq \theta \leq \pi/4$
spin:	$0 \leq \phi \leq 2\pi$

Fig. 4.2 shows the rotor pole configurations with respect to the rotor body frame. Similarly, the stator pole configuration with respect to the stator coordinate frame is shown in Fig. 4.3 where  $S_i$  defined the  $i^{\text{th}}$  space bounded between two adjacent projections of the radial lines connecting the origin and the stator poles on the xy plane. Let b be the end point of the 4<sup>th</sup> rotor pole. Consider  $b \in S_1$ , the range of the spin angle about the pole b required in the formation of the look-up table is  $0 \leq \phi \leq 2\pi/3$ . Suppose b remains the same position and spin angle  $\phi \geq 2\pi/3$ . Since the rotor poles are evenly spaced at  $2\pi/3$  apart about the pole b, the same torque generated will remain unchanged if the control inputs are the same as the case when  $\phi' = \phi \pm 2\pi/3$ . Therefore, to produce the same torque,  $u(\phi) = u(\phi \pm 2\pi/3)$ .

Outside the region  $S_1$ , the same torque can be obtained by transformations of the control input U for b as follows: In general,

$$\mathbf{U}^{(K)} = [\mathbf{R}_K] \mathbf{U}^{(1)}$$

Table 4.1. Coordinate of the stator poles

pole	x	y	z
0	0.0000	0.0000	0.0000
1	0.8944	0.0000	0.4472
2	0.2764	0.8507	0.4472
3	-0.7236	0.5257	0.4472
4	-0.7236	-0.5257	0.4472
5	-0.2764	-0.8507	0.4472
6	0.7236	-0.5257	-0.4472
7	0.7236	0.5257	-0.4472
8	-0.2764	0.8507	-0.4472
9	-0.8944	0.0000	-0.4472
10	-0.2764	-0.8507	-0.4472
11	0.0000	0.0000	-1.0000

Table 4.2. Coordinates of the rotor poles

pole	x	y	z
1	0.9428	0.0000	0.3333
2	-0.4714	0.8165	0.3333
3	-0.4714	-0.8165	0.3333
4	0.0000	0.0000	1.0000

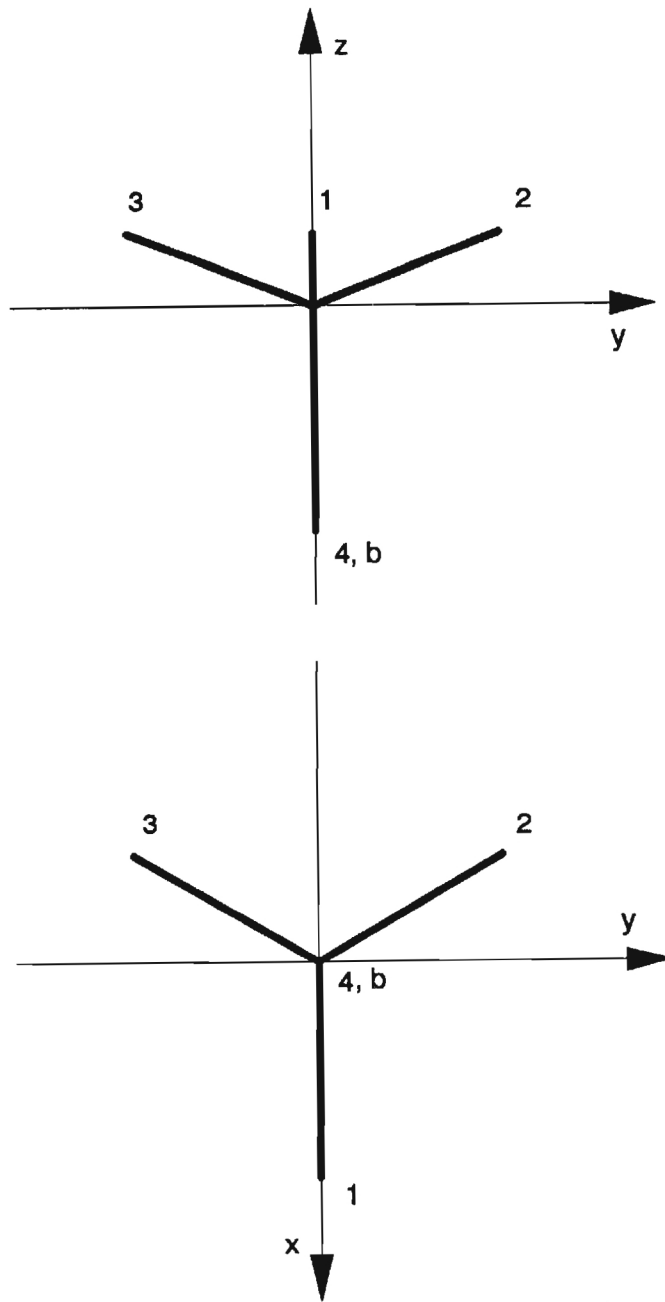


Figure 4.2 Rotor pole configuration

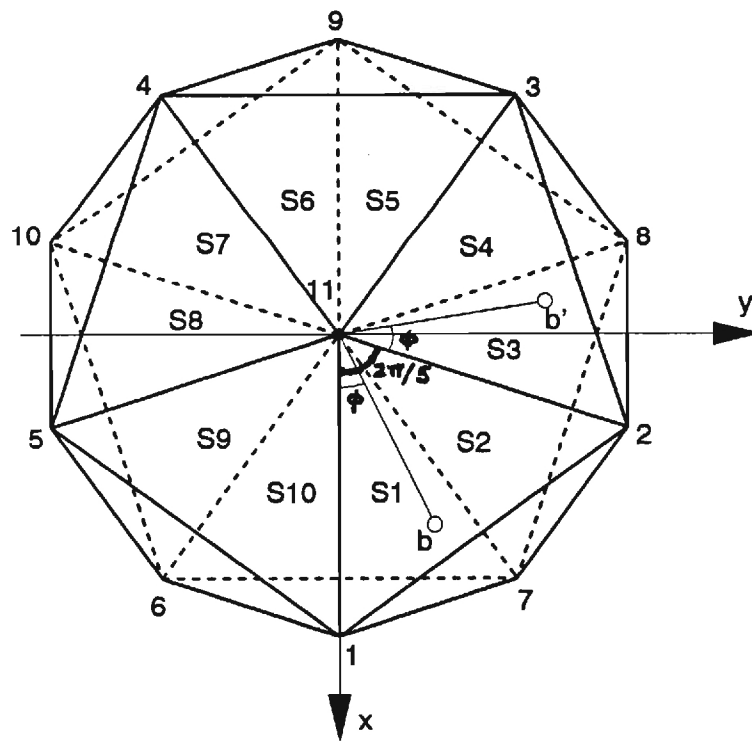


Figure 4.3 Stator pole configuration

First consider the case where  $K$  is an odd index number defining the region  $S_K$  indicated in Fig. 4.3. Suppose  $b \in S_3$ . If  $(\psi, \theta, \phi)$  denotes the position of  $b$  when  $b \in S_1$ , the corresponding position of  $b$  in the region  $S_3$  can be written as  $(\psi + 2\pi/5, \theta, \phi)$ . If  $U^{(1)}$  where the superscript (1) denotes the input vector  $U$  required to generate  $T$  when  $b \in S_1$ , to produce the same torque  $T$  with respect to the rotor body frame, the input vector  $U^{(3)}$  is deduced from  $U^{(1)}$  by shifting the components of  $U^{(1)}$   $2\pi/5$  in the counterclockwise direction. Hence, the transformation  $[R_3]$  is made up by the following equations:

$$[R_3] = \begin{bmatrix} 0 & 0 & 0 & 0 & 1 & 0 & 0 & 0 & 0 & 0 & 0 \\ 1 & 0 & 0 & 0 & 0 & 0 & 0 & 0 & 0 & 0 & 0 \\ 0 & 1 & 0 & 0 & 0 & 0 & 0 & 0 & 0 & 0 & 0 \\ 0 & 0 & 1 & 0 & 0 & 0 & 0 & 0 & 0 & 0 & 0 \\ 0 & 0 & 0 & 1 & 0 & 0 & 0 & 0 & 0 & 0 & 0 \\ 0 & 0 & 0 & 0 & 0 & 0 & 0 & 0 & 0 & 1 & 0 \\ 0 & 0 & 0 & 0 & 0 & 1 & 0 & 0 & 0 & 0 & 0 \\ 0 & 0 & 0 & 0 & 0 & 0 & 1 & 0 & 0 & 0 & 0 \\ 0 & 0 & 0 & 0 & 0 & 0 & 0 & 1 & 0 & 0 & 0 \\ 0 & 0 & 0 & 0 & 0 & 0 & 0 & 0 & 1 & 0 & 0 \\ 0 & 0 & 0 & 0 & 0 & 0 & 0 & 0 & 0 & 0 & 1 \end{bmatrix}$$

The remaining transformations for an odd number of  $K$  is given as follows:

$$[R_1] = [I]$$

$$[R_5] = [R_3]^2$$

$$[R_7] = [R_3]^3$$

$$[R_9] = [R_3]^4$$

Finally, consider an even number of  $K$ . To begin with, suppose  $b \in S_{10}$ . From symmetric, the mirror image of any point  $b$  with its position denoted by  $(\psi, \theta, \phi) \in S_1$  is  $(-\psi, \theta, -\phi) = (2\pi-\psi, \theta, 2\pi-\phi) \in S_{10}$ . Since this symmetry is mirror-like and cannot produce the same torque by

simple transforms, but we can produce a torque that is the mirror image of the torque produced when  $b \in S_1$ .

$$\mathbf{T}_e = \begin{bmatrix} -1 & 0 & 0 \\ 0 & 1 & 0 \\ 0 & 0 & -1 \end{bmatrix} \mathbf{T}_o$$

This can be done by using the transformation  $[\mathbf{R}_{10}]$ :

$$[\mathbf{R}_{10}] = \begin{bmatrix} 1 & 0 & 0 & 0 & 0 & 0 & 0 & 0 & 0 & 0 & 0 \\ 0 & 0 & 0 & 0 & 1 & 0 & 0 & 0 & 0 & 0 & 0 \\ 0 & 0 & 0 & 1 & 0 & 0 & 0 & 0 & 0 & 0 & 0 \\ 0 & 0 & 1 & 0 & 0 & 0 & 0 & 0 & 0 & 0 & 0 \\ 0 & 1 & 0 & 0 & 0 & 0 & 0 & 0 & 0 & 0 & 0 \\ 0 & 0 & 0 & 0 & 0 & 0 & 1 & 0 & 0 & 0 & 0 \\ 0 & 0 & 0 & 0 & 0 & 1 & 0 & 0 & 0 & 0 & 0 \\ 0 & 0 & 0 & 0 & 0 & 0 & 0 & 0 & 0 & 1 & 0 \\ 0 & 0 & 0 & 0 & 0 & 0 & 0 & 0 & 1 & 0 & 0 \\ 0 & 0 & 0 & 0 & 0 & 0 & 0 & 1 & 0 & 0 & 0 \\ 0 & 0 & 0 & 0 & 0 & 0 & 0 & 0 & 0 & 0 & 1 \end{bmatrix}$$

For an even number of K, the transformation is given as follows:

$$[\mathbf{R}_2] = [\mathbf{R}_3] [\mathbf{R}_{10}]$$

$$[\mathbf{R}_4] = [\mathbf{R}_3]^2 [\mathbf{R}_{10}]$$

$$[\mathbf{R}_6] = [\mathbf{R}_3]^3 [\mathbf{R}_{10}]$$

$$[\mathbf{R}_8] = [\mathbf{R}_3]^4 [\mathbf{R}_{10}]$$

Thus, the ranges of the rotor coordinates are reduced to

$$\begin{array}{ll} \text{precession:} & 0 \leq \psi \leq 2\pi/5, \\ \text{nutaton:} & 0 \leq \theta \leq \pi/4, \text{ and} \\ \text{spin:} & 0 \leq \phi \leq 2\pi/3, \end{array}$$

which represents 1/30 as the original range. It is expected that the memory size required by the table can be reduced to the order of 100 Kbytes.

## 5. CONCLUSIONS AND FUTURE WORK

This section is a summary of major findings already discussed in each of the previous sections:

1. Along with an illustrative example, the design feasibility of a ball-joint-like spherical VR motor has been described in terms of the overlapping area between the circular stator and rotor poles. Two general expressions to determine the overlapping area between any circular stator/rotor pole pair in three dimensional space, an exact solution and an approximation, have been derived.
2. Magnetic flux patterns of a typical pole interaction have been predicted using finite element methods. It has been shown that inaccurate assumed flux shapes and the assumption of no magnetic leakages in deriving the reluctance force could lead to a significant error as high as 90%.
3. By choosing current sources for coil excitation, the torque prediction model is algebraic and decoupled from the dynamic equations of motion and thus, would reduce the motion control to a great extent.
4. The inverse problem to torque prediction model of the three DOF spherical VR motor, which determines the coil excitations for a specified torque, is characterized by its infinite solutions.
5. Along with the formulation for input vector optimization, the memory size of the lookup table for practical implementation of the optimal solution can be effectively reduced by parameter elimination technique and the symmetry property of pole configuration.

The analysis presented in this report would serve as a basis for spherical VR motor design. Research efforts have been led to the prototype development of a three DOF spherical VR motor. The prototype spherical VR motor will serve as a testbed for experimental verification of the reluctance and the torque prediction models. Research efforts have currently been directed towards the motion control law development and implementation.

## REFERENCES

1. Bennett, "A mechanical Wrist for a Robot Arm," B.S. Thesis, MIT 1968.
2. Rosheim, M.E., "Robot Wrist Actuators," *Robotics Age*, Nov/Dec 1982
3. Asada, H. and Cro-Granlto, J. A. "Kinematic and Static Characterization of Wrist Joints and their Optimal Design," *Proc. of the 1985 IEEE Int. Conf. on Robotics and Automation*. 1985.
4. Paul, R. P. and Stevenson, C. N., "Kinematics of Robots Wrist," *Int. Journal of Robotics Research*, Vol. 2, No. 1, pp. 31-38, 1983.
5. William, F., Laithwaite, E., and Piggot, L., "Brushless Variable-Speed Induction Motors," *Proc. IEEE*, No. 2097U, pp.102-118, June 1956.
6. Williams, F., Laithwaite, E., and Eastham, G. F. "Development of Design of Spherical Induction Motors," *Proc. IEEE*, No. 3036U, pp. 471-484, December 1959.
7. Laithwaite, E., "Design of Spherical Motors," *Electrical Times*, vol. 9, pp. 921-925, June 1960.
8. Laing I. and Laing, N. Patent U.S. 4352646, Rotodynamic Pump with Spherical Motor, October 5, 1982.
9. Lebedev A. and Shinyev, P. "Moments Acting in a Spherical Rotor in a Magnetic Suspension," *Priborostroegie*, vol. 16, No.5 pp. 85-88, 1973.
10. Izv Vyssh Uchebn Zaved, "Electromagnetic processes in an Asynchronous Motor with a Spherical Hollow Rotor," *Electromekh*, N. 11, pp 1231-1239, Nov. 1976.
11. Vachtsevanos, G.J., and Davey K., and Lee, K. "Development of a Novel Intelligent Robotic Manipulator," *Control Systems Magazine*, June 1987.
12. Davey, K., Vachtsevanos, G., and Powers, R., "The Analysis of Fields and Torques in Spherical Induction Motors", *IEEE Trans. on Magn.*, Vol. MAG-23, No. 1, January 1987.
13. Vachtsevanos, G.J., and Davey K., and Lee, K. "Development of a Novel Intelligent Robotic Manipulator," Presented at the 1986 IEEE Int. Conf. on Systems, Man, and Cybernetic, Atlanta, GA October 10-17, 1986. Also in *Control Systems Magazine*, June 1987.
14. Hollis, R. L., Allan, A.P. and Salcudan, S., "A Six Degree-of-Freedom Magnetically Levitated Variable Compliance Fine Motion Wrist," *The 4th Int'l Symp. on Robotics Research*, Santa Cruz, August 1987.

15. Kaneko, K., Yamada, I. and Itao, K. "A Spherical DC Servo Motor with Three Degrees of Freedom", ASME, Dyn. Systems & Control Div., Vol. 11, 1988, p. 433.
16. Foggia, A.; Oliver, E.; Chappuis, F. and Sabonnadiere, J., "New Three Degrees of Freedom Electromagnetic Actuator," Conference Record - IAS Annual Meeting, Vol. 35, No. 6, Published by IEEE, New York, NY, USA; 1988, pp. 137-141.
17. Lee, K.M. and Kwan, C., "Design Concept Development of a Spherical Stepper for Robotic Applications," IEEE Trans. Journal of Robotics and Automation, February 1991.
18. Chai, H. D. "Permeance Model and Reluctance Force Between Toothed Structures. Theory and Applications of Step Motor edited by Kuo B.C.; West Publishing Co. 1973.
19. Sylvester, P. and Ferrari, R. L., "Finite Elements for Electrical Engineers," Cambridge University Press, New York, 1986.
20. "Introduction to ANSYS," Vol. 1 & 2, Swanson Analysis System.
21. Wolfe, P., "Methods for Linear Constraints," Nonlinear Programming, North Holland, 1967.
22. Wolfe, P., "Methods of Nonlinear Programming," Recent Advances in Mathematical Programming, McGraw-Hill, New York, 1968.
23. Abadie, J. and Carpentier, J. , "Generalization of the Wolfe Reduced Gradient Method to Case of Nonlinear Constraints," Optimization, Academic Press, 1969.
24. Lasdon, L. S., and Warren, A.D., "GRG2 User's Guide," University of Texas at Austin, 1989.

## APPENDIX

### FINITE ELEMENT FORMULATION

The fundamental equations of magnetostatics, which relate the electromagnetic field and source quantities in a magnetic field system, are described the following Maxwell's equation as:

$$\nabla \cdot \mathbf{B} = 0 \quad (1)$$

$$\nabla \times \mathbf{H} = \mathbf{J} \quad (2)$$

where  $\mathbf{B}$  is the flux density,  $\mathbf{H}$  is the magnetic field intensity, and  $\mathbf{J}$  is current density. Equation (1) states that the magnetic flux lines are sourceless at any point in the field. Equation (2) states that the circulation of the magnetic field at a point is due to the existence of current with density  $\mathbf{J}$  at that point. In addition to these equations, the constitutive law that describe how the physical properties of the materials affect the field and source quantities is given by

$$\mathbf{B} = \mu \mathbf{H} \quad (3)$$

where  $\mu$  is the permeability of the material.

The Maxwell's equations are numerically solved using finite element method to predict the magnetic field. In order to do so, the Maxwell's equations are formulated into a Poisson equation which was then solved by the finite element method. Two particular methods are used in the finite element formulation; namely, the vector potential formulation and the reduced scalar potential formulation.

#### A.1 Vector Potential Formulation

In the vector potential formulation, a vector potential  $\mathbf{A}$  is defined as

$$\nabla \times \mathbf{A} = \mathbf{B} \quad (\text{A.1})$$

$$\nabla \cdot \mathbf{A} = 0. \quad (\text{A.2})$$

Using the constitutive law defined in Equation (3) and the definition given in Equation (A.1), Equation (2) becomes

$$\nabla \times \left( \frac{1}{\mu} \nabla \times \mathbf{A} \right) = \mathbf{J}. \quad (\text{A.3})$$

In the two-dimensional analysis, where both the current density  $\mathbf{J}$  and the magnetic vector potential  $\mathbf{A}$  possess only longitudinally directed components, i.e.  $A_x = A_y = 0$ ,  $J_x = J_y = 0$ , and  $A_z = A_z(x,y)$ , Equation (A.3) can be simplified to

$$\nabla \cdot \left( \frac{1}{\mu} \nabla \mathbf{A}_z \right) = - J_z \quad (\text{A.4})$$

which is in the form of a Poisson equation.

$A_z$  is assumed to have an expansion form

$$A_z = \sum_j^N a_j N_j. \quad (\text{A.5})$$

where the  $a_j$  terms are unknowns and the  $N_j$  are chosen shape functions. The  $N$  shape functions are chosen such that each shape function has a value of 1 at the node  $i$ , and linearly reduces to 0 at the adjacent nodes and the rest of the domain.

Equation (A.4) is multiplied by  $N_i$  ( $i = 1, \dots, N$ ) on both sides and integrated by parts over the domain  $D$ . By applying the divergence theorem to the first term on the left-hand side of Equation (A.6) and substituting  $A_z$  from Equation (A.5) into Equation (A.6), the unknown vector  $\mathbf{a} = [a_1 \dots a_N]^T$  can be determined from Equation (A.7)

$$[\mathbf{K}] \mathbf{a} = \mathbf{c} \quad (\text{A.7})$$

where the elements of the  $N \times N$  constant matrix  $[\mathbf{K}]$ ,  $k_{ij}$ , is

$$k_{ij} = \int_D \frac{1}{\mu} \nabla N_j \cdot \nabla N_i \, dx \quad (\text{A.8})$$

and the element  $c_i$  of the constant vector  $\mathbf{c} = [c_1 \dots c_N]^T$  is

$$c_i = \int_D J_z N_i \, dx - \int_{\partial D} \frac{N_i}{\mu} \frac{\delta A_z}{\delta n} \, dx \quad (\text{A.9})$$

where  $\partial D$  denotes the boundary of domain  $D$  and  $\partial A_z / \partial n$  is the boundary condition to be specified.

Since  $\mu$  is a nonlinear function of  $H$ , this solution process must be iterative. The first iteration uses a guessed value of  $\mu$  to evaluate  $k_{ij}$  and  $c_i$  numerically from the integrals in Equations (A.8) and (A.9) respectively. The solution of  $A_z$  can be determined from the summation in Equation (A.5) by solving for the nodal potential vector  $\mathbf{a}$  from Equation (A.7). The flux density  $B$  can then be computed from Equation (A.1). Using the computed flux density  $B$ , the  $\mu$  value is updated according to the  $B$ - $H$  curve of the magnetic material. The solution is repeated until further update of  $\mu$  does not cause significant change in  $B$ .

## A.II Reduced Scalar Potential Formulation

In the reduced scalar potential formulation, the magnetic field intensity  $\mathbf{H}$  is first distinguished as the fraction due to current sources and the fraction due to the induced magnetization of the material. That is,

$$\mathbf{H} = \mathbf{H}_s + \mathbf{H}_m$$

where  $\mathbf{H}_s$  is due to the current sources and  $\mathbf{H}_m$  is due to magnetization of the material. Thus, Equation (3.2) gives

$$\nabla \times (\mathbf{H}_s + \mathbf{H}_m) = \mathbf{J} \quad (\text{A.10})$$

or

$$\nabla \times \mathbf{H}_s = \mathbf{J}$$

$$\nabla \times \mathbf{H}_m = 0$$

Equation (A.10) suggests that  $\mathbf{H}_m$  is curl free and therefore can be expressed as the gradient of a "reduced" scalar function  $V$  as []

$$\nabla V = -\mathbf{H}_m \quad (\text{A.11})$$

The term "reduced" comes from the fact that  $V$  is defined only by  $\mathbf{H}_m$ , not the full field intensity  $\mathbf{H}$  which can be expressed correspondingly as

$$\mathbf{H} = -\nabla V + \mathbf{H}_m \quad (\text{A.12})$$

Equation (1) become  
s

$$\nabla \cdot (\mu \nabla V) = \nabla \cdot (\mu \mathbf{H}_s) \quad (\text{A.13})$$

which is in the form of a Poisson equation. The left hand side term  $\mathbf{H}_s$  can be directly calculated from the current sources by applying the Biot-Savart law as follows

$$\mathbf{H}_s = \frac{1}{4\pi} \int_D \frac{\mathbf{J} \times \mathbf{r}}{|\mathbf{r}|^3} dv \quad (\text{A.14})$$

where the domain of integration  $D$  is the entire current carrying body,  $\mathbf{r}$  is the vector pointing from the differential current carrying body to the point where the  $\mathbf{H}_s$  is to be calculated, and  $\mathbf{J}$  is the current density at this differential body.

Using Gerlakin approach, the reduced scalar function  $V$  is approximated by

$$V = \sum_j^N v_j N_j \quad (\text{A.15})$$

where the  $v_j$  terms are unknowns and the  $N_j$  are chosen shape functions as defined in Equation (A.5). The finite element formulation of Equation (A.13) is similar to that for the vector potential method. The unknown vector  $\mathbf{v} = [v_1 \dots v_N]^T$  is determined from Equation (A.16)

$$[\mathbf{K}]\mathbf{v} = \mathbf{c} \quad (\text{A.16})$$

where

$$k_{ij} = \int_D \mu \nabla N_j \cdot \nabla N_i \, dx \quad (\text{A.17})$$

$$c_i = \int_D \mu \mathbf{H}_s \cdot \nabla N_i \, dx - \int_{\partial D} \mu N_i \frac{\partial V}{\partial n} \, dx. \quad (\text{A.18})$$

and where  $\partial V/\partial n$  is the boundary condition to be specified. The solution of  $\mathbf{H}$  is an iterative process, which starts with a guessed value of  $\mu$ . The nodal potential vector  $\mathbf{v}$  is solved from Equation (A.16), in which  $k_{ij}$  and  $c_i$  are evaluated numerically from the integrals in Equations (A.17) and (A.18). The field intensity  $\mathbf{H}$  can then be solved from Equation (A.12) and the new value of  $\mu$  is obtained using Equation (3). This process is repeated until the change of  $\mu$  does not cause significant change in  $\mathbf{H}$ .

In the reduced scalar potential formulation the flux lines are not equipotential lines. In general, the flux lines are not orthogonal to the equipotential lines except when the current sources  $\mathbf{H}_s$  are absent from the system.